

Shape-based image reconstruction methods for hyperspectral diffuse optical tomography

A dissertation

submitted by

Friðrik Lárusson

In partial fulfillment of the requirements

for the degree of

Doctor of Philosophy

in

Electrical Engineering

Tufts University

February 2013

©2013 Friðrik Lárusson

© Copyright 2013 by Friðrik Lárusson

Abstract of “Shape-based image reconstruction methods for hyperspectral diffuse optical tomography”, by Fridrik Larusson, Ph.D., Tufts University, October 2012.

Diffuse optical tomography (DOT) is an optical imaging modality that uses near infrared light to recover functional information of tissue. In this thesis we focus on breast imaging where estimation of the optical properties of the breast can assist in detecting cancerous tumors and in judging overall breast health.

To this end we explore the application of a parametric level set method (PaLS) for image reconstruction for hyperspectral DOT. Chromophore concentrations and diffusion amplitude are recovered using a linearized Born approximation model and employing data from over 100 wavelengths. The images to be recovered are taken to be piecewise constant and a newly introduced, shape-based model is used as the foundation for reconstruction. The PaLS method significantly reduces the number of unknowns relative to more traditional level-set reconstruction methods and has been shown to be particularly well suited for ill-posed inverse problems such as the one of interest here. We extend the PaLS method to imaging problems by considering a redundant dictionary matrix for basis functions allowing for recovery of a wide array of shapes.

Additionally we explore the ability of diffuse optical tomography (DOT) to recover 3D tubular shapes representing vascular structures in breast tissue. Using the

PaLS method, we incorporate the connectedness of vascular structures in breast tissue to reconstruct shape and absorption values from severely limited data sets. The approach is based on a decomposition of the unknown structure into a series of two dimensional slices. Using a simplified physical model that ignores 3D effects of the complete structure, we develop a novel inter-slice regularization strategy to obtain global regularity. We report on simulated and experimental reconstructions using realistic optical contrasts where our method provides a more accurate estimation compared to an unregularized approach and a pixel based reconstruction.

Dedication

Tvær konur eiga þessa ritgerð

Jóhanna Lárentsínusdóttir

&

Helga Marín Gestsdóttir

Acknowledgements

This work is supported by financial support provided by the National Institutes of Health grant R01 CA154774.

Many thanks to my advisor, Prof. Eric Miller. He showed me how to be a good researcher and taught me how to communicate with people outside of my area. Always encouraging and pushing me forward when I needed it. I really appreciate the time spent in his lab, and will carry what I learned throughout my life. I am also tremendously grateful to Prof. Sergio Fantini, his advice and guidance has meant a lot to me. He taught me how to ask questions in an intelligent way and that a good engineer should always have questions to ask. It was a lot of fun to get the chance to work so closely with the Biomedical group, and being able to get a taste of things on the other side on the fence.

Many thanks to the members of my dissertation committee, Dr. Qianqian Fang for his helpful suggestions in the final writing of this thesis and Dr. Brian Tracy for his insight and discussions in between work at 196 Boston Ave.

Prof. Angelo Sassaroli for all his assistance and putting up with all my questions.

He always took the time out to meet with me and talk about geography as well as the never ending topic of photon migration.

Thanks to Dr. Alireza Aghasi, one of the smartest people I have ever met. He was always willing to help out and give me advice, even when he was swamped with work himself.

My office mate and friend, Oguz Semerci. A lot of arguments over the legitimacy of blockbuster movies, the quality of cooked supermarket ham, the optimal number of basis functions and regularization parameters. How boring the office would have been if he hadn't been there.

Everybody in the Biomedical Department that helped me out. Bertan and Michele for all the help and putting up with all the de-stressing discussions. Jana for all the help and advice and Gee for all the data you collected. Pami for being an enormous help in the home stretch, taking measurements, talking about measurements, and finally taking more measurements. It was a huge help.

I would like to thank my parents. Always backing me up and making sure that I have support and love. Giving me advice, having fun with me and going off to the mountains when I needed it. They pointed me in the right direction. My in-laws for putting up with me when I had to work when they came to visit. Cooking dinners, being great company and bringing all the kókómjólk, draumur and love. Skúli and Auður for the good times in Boston and Fífumýri, good food and awesome discussions. Iðunn Mattea, thanks for all your crazy stuff.

My brother for all the assistance and pointers he gave me. Basically showing me how every graduate student goes through the same process and I should power through. He also introduced me to Niko Bellic and his cousin.

My “kjallara”-crew in Iceland. Long skype sessions, talking about music, movies and video games, camping trips in the summers and board games in winters. This group is a large part of who I am.

My wife, Helga Marín Gestsdóttir. I have no idea how many times she had to talk to me about the details of my thesis, or sit with me and Oguz while we endlessly talked about our work. She owns this thesis, and all my work is for her.

Contents

List of Tables	x
List of Figures	xii
1 Introduction	1
1.1 Non-tomographic optical modalities	3
1.2 Diffuse optical tomography	7
1.3 The purpose of this work	15
1.4 Thesis Outline	16
2 Background	17
2.1 Image reconstruction for DOT	17
2.2 Linear approximations	20
2.2.1 Born Approximation	21
2.2.2 Rytov Approximation	22
2.3 Regularization techniques	23

2.3.1	Reconstruction using the singular value decomposition	24
2.3.2	Tikhonov Regularization	26
2.4	Non-linear reconstruction	28
2.5	Shape Based Methods	31
2.5.1	Primitives for 3D shape estimation	35
2.6	Hyperspectral information	38
3	Forward Models	42
3.1	Diffusion approximation	42
3.2	Discrete model and integral equation	45
3.3	Green's Functions	46
3.4	Born Approximation	49
4	Experimental methods	54
4.1	Measurements	54
4.2	Milk and Water phantom	55
4.2.1	Liquid phantom	55
4.2.2	Measurement setup	58
4.3	Silicon phantom	62
4.3.1	Construction of Cylinder	62
4.3.2	Scanning measurments	63
5	Hyperspectral PaLS Based Reconstruction	66

5.1	Parametric level-set method	66
5.2	Inversion using PaLS	72
5.3	Comparing to a Pixel-based reconstruction	76
5.3.1	Selecting optimal regularization for multiple chromophores . .	78
5.4	Implementing Hyperspectral information	80
5.5	Simulation analysis	81
5.6	Results	84
5.6.1	Simulations	84
5.6.2	Experimental validation	90
5.7	Discussion	93
6	Dictionary Approach	98
6.1	Introduction	98
6.2	Projected Levenberg-Marquardt	101
6.3	Results and Discussion	105
7	Parametric estimation of 3D tubular structures using primitives	109
7.1	Forward Model for 2D slices	111
7.2	Image reconstruction	112
7.3	Simulation Analysis	115
7.4	Results	118
7.4.1	Simulations	118

7.4.2	Experimental Validation	121
7.5	Discussion	125
8	Conclusion	128
A	Jacobian for Levenberg Marquardt optimization	135
	Bibliography	139

List of Tables

5.1	<i>The MSE is compared for each chromophore for multiple wavelength choices. For the 8 wavelength case optimal wavelengths are used, where 176 wavelengths are equally spaced.</i>	84
5.2	<i>$D(S, G)$ is compared for each chromophore for multiple wavelength choices. In each case the reconstructions are done with equally spaced wavelengths over the spectrum except for the 8 wavelength case. $D(S, G)$ is calculated comparing 80% of the target peak to the reconstruction. . .</i>	86
5.3	<i>$D(S, G)$ is compared for each chromophore for multiple wavelength choices. In each case the reconstructions are done with equally spaced wavelengths over the spectrum except for the 6 wavelength case where we use optimally chosen wavelengths. $D(S, G)$ is calculated comparing the half maximum of the target peak to the reconstruction.</i>	93
5.4	<i>Comparison of $\hat{\mathbf{c}}_i$ and $\hat{\mathbf{c}}_i^r$ to target concentration values for experimental results, for the pixel-based method. Best performance is highlighted in bold.</i>	94

5.5	<i>Comparison of $\hat{\mathbf{c}}_i$ and $\hat{\mathbf{c}}_i^r$ to target concentration values for experimental results, for the PaLS method. Best performance is highlighted in bold.</i>	95
7.1	<i>Error metrics used to judge image reconstructions for simulated reconstructions.</i>	124
7.2	<i>Error metrics used to judge image reconstructions for experimental reconstructions.</i>	125

List of Figures

1.1	<i>The process of photons passing through tissue [13]. Black line represents light injected into the medium, where part of it is reflected right at the surface, represented by the brown arrow. Purple line represents diffuse reflectance, where light is scattered out the same side as the injected light. Blue line represent scattered and absorbed photons, where the green arrow is scattered photons that travel to the detector. Finally, red line represent ballistic photons that undergo no scattering events. .</i>	9
2.1	<i>Basic setup of the imaging problem in this thesis. It demonstrates where optical properties \mathbf{c} are separated into foreground and background. The model \mathbf{K} acts on the entire domain, \mathcal{F}, to generate Φ</i>	18
2.2	<i>Definition of anomalous region Ω within the imaging domain \mathcal{F} used for shape-based methods.</i>	32
2.3	<i>Example of hyperspectral cube considered for multi wavelength imaging. Each pixel in each image on the spectral axis corresponds to an absorption value in the near-infrared spectrum.</i>	39

2.4	<i>Molar extinction coefficients for oxy-hemoglobin (HbO_2) deoxy-hemoglobin (HbR) shown as a function of wavelength.</i>	40
3.1	<i>Setup of the slab geometry with example mirror sources used for calculating the slab geometry Green's function. Figure is not to scale. . . .</i>	48
4.1	<i>Absorption spectra of the ink and dye solutions chromophores used in experimental measurements. Specifically chosen wavelengths are marked with an asterisk.</i>	56
4.2	<i>(a) Absorption spectra for the background, μ_a, and the inclusion, $\mu_a + \Delta\mu_a$, in experimental set 1, containing 10% ink and 90% dye. (b) Contrast between the background and the inclusion for experimental set 1.</i>	58
4.3	<i>(a) Absorption spectra for the background, μ_a, and the inclusion, $\mu_a + \Delta\mu_a$, in experimental set 2, containing 70% ink and 30% dye. (b) Contrast between the background and the inclusion for experimental set 2.</i>	59
4.4	<i>The setup of sources and detectors for infinite geometry using liquid milk and water phantom.</i>	60
4.5	<i>Silicon phantom used for experimental measurements. Homogeneous cylindrical slab, with two absorbing inclusions.</i>	61

4.6	<i>The setup of sources and detectors for simulation reconstructions. Same orientation of axes is used for experimental data. The angle φ represents the angle between the axis of the inclusion, along y in the figure, and the scanning direction, along x in the figure.</i>	64
4.7	<i>Calculated ground truth images for phantom angled at $\varphi = 90^\circ$ and $\varphi = 30^\circ$ relative to scanning direction along the x-axis.</i>	65
5.1	<i>(a) Definition of domains used for the parametric level-set methods as shown in Chapter 2. (b) Circles represent example basis functions placed on a fixed grid in the imaging medium. The iteration process evolves κ_i to the estimated anomaly structure. (c) Example of movable basis functions placed in the imaging medium. The iteration process evolves κ_i and ψ_i towards the estimated anomaly structure</i>	67
5.2	<i>Reconstruction using a pixel based method. Leftmost column are ground truth images, middle column of images are generated with 8 wavelengths and rightmost images are generated with 176 wavelengths. From top to bottom the rows show HbO_2, HbR, lipid, water and diffusion amplitude, respectively. Concentration units are in mM.</i>	85

5.3	<i>Reconstruction using the PaLS method. Leftmost column are ground truth images, middle column of images are generated with 8 wavelengths and rightmost images are generated with 176 wavelengths. From top to bottom the rows show HbO_2, HbR, lipid, water and diffusion amplitude, respectively. Concentration units are in mM.</i>	87
5.4	<i>(a) L-hypersurface, defined by (5.25) plotted against regularization parameters. (b) H curvature, defined by (5.26), computed for the L-hypersurface. (c) Error estimation surface, defined by (5.31), plotted against regularization parameters. The optimal regularization parameters are marked in each case with a red arrow.</i>	89
5.5	<i>Reconstruction for HbO_2 and HbR using a pixel based method. Upper row is for the HbO_2 chromophore and the lower for HbR. Concentration units are in mM. Reconstruction performed for 176 equally spaced wavelengths.</i>	90
5.6	<i>Pixel reconstruction from both experimental sets, set 1 containing 10% ink and 90% dye and set 2 70% ink and 30% dye. Black circle denotes the true location of the inclusion.</i>	96
5.7	<i>PaLS Reconstruction from both experimental sets, set 1 containing 10% ink and 90% dye and set 2 70% ink and 30% dye. Black circle denotes the true location of the inclusion.</i>	97

6.1	<i>Example basis functions placed on a fixed grid in the imaging medium, where each grid point, f, has a set of different shaped basis functions, denoted by $\{l\}$.</i>	98
6.2	<i>Example of the object function \mathbf{O} as defined by (6.2). The aim is to estimate a $\boldsymbol{\kappa}$ weighting vector with induced sparsity to pick out optimal basis functions from a dense dictionary matrix \mathbf{B} where $\boldsymbol{\psi}_l^f$ represent the l^{th} function at gridpoint f.</i>	101
6.3	<i>Projection, $\pi(\boldsymbol{\kappa})$ of the weight vector $\boldsymbol{\kappa}$ to the ℓ_1 norm ball to induce sparseness. This results in selecting the optimal collection of basis functions representing the shape.</i>	102
6.4	<i>Reconstructions for Case I of low complexity. Top row shows HbO_2, middle is HbR and bottom row displays weights used in the reconstruction. Signal to noise ratio is set to 50 dB.</i>	105
6.5	<i>Reconstructions for Case II of medium complexity. Top row shows HbO_2, middle is HbR and bottom row displays weights used in the reconstruction. Signal to noise ratio is set to 50 dB.</i>	106
6.6	<i>Reconstructions for Case III of high complexity. Top row shows HbO_2, middle is HbR and bottom row displays weights used in the reconstruction. Signal to noise ratio is set to 50 dB.</i>	107

7.1	<i>Example of how 2D slices are used to estimate 3D structure with data from measurements collected as in Fig. 4.6. Each 2D primitive is estimated with vector θ_k. Regularization term in the objective function, (7.2), correlates each slice primitive together, to generate a connected structure</i>	110
7.2	<i>Ground truth image used to generate simulated data.</i>	120
7.3	<i>(a) Example L-curve used to select optimal α for the reconstruction using 2 detectors at 30 dB SNR for simulated data. (b) Example L-curve used to select optimal α for the reconstruction using 10 detectors at 30 dB SNR for simulated data.</i>	120
7.4	<i>Reconstruction results for a simulated geometry structure with realistic optical contrast.</i>	121
7.5	<i>Reconstruction results from simulated data with realistic optical contrast, using 2 detectors for each source location</i>	122
7.6	<i>Reconstruction results from simulated data with realistic optical contrast, using 10 detectors for each source location</i>	123
7.7	<i>Slice reconstruction from $y = 5$ cm, demonstrating absorption contrast. 3D reconstructed using 10 detectors shown in Fig. 7.6.</i>	124
7.8	<i>Reconstruction results using experimental data and 3 detectors. Inclusions are angled 90° relative to scanning direction, $\alpha = 12$.</i>	125

7.9	<i>Reconstruction results using experimental data and 3 detectors. Inclusions are angled 30° relative to scanning direction, $\alpha = 80$.</i>	126
7.10	<i>Slice reconstruction located at $y = 3$ cm in Fig. 7.8, compared to ground truth demonstrating absorption contrast.</i>	127
8.1	<i>Hemoglobin saturation maps measured, where false-color representation of oxygenation values are superimposed on a gray level image. Image and data was reported in Yu et al. [111].</i>	132

Chapter 1

Introduction

Non-invasive imaging modalities are becoming increasingly important to monitor female breast health in the 21st century. The Cancer Prevention and Control division of the Centers for Disease Control and Prevention (CDC) states that breast cancer is the most common cancer among women of all races in the United States [53], and the World Health Organization (WHO) lists it as the top cancer in women in both the developed and developing world [25]. Among the leading causes of cancer death among women, breast cancer ranks second outnumbered only by deaths due to lung cancer. In the prevention and control protocol published by WHO great significance is placed on early detection. Although some risk reduction is achieved by prevention, i.e. promoting healthy diet and physical activity, these strategies cannot eliminate the majority of breast cancers that develop in low- and middle income countries. Because of this, early detection is the cornerstone of achieving successful breast cancer

control [2].

To this end screening methods need to incorporate detection systems and imaging modalities that are low-cost, portable and as we discuss in greater detail shortly sensitive to functional information of the breast tissue. Keeping detection systems low-cost is a significant factor, especially considering breast cancer mortality rates in the developing world. The ratio of mortality to incidence is below 0.2 in North America, where it is 0.35 in Latin America and the Caribbean and 0.7 in Africa [87]. There is a clear positive gradient between level of economic development and probability of survivorship across and within regions, which is closely related to inequities in access to knowledge, early detection and treatment.

Breast imaging researchers have for a long time been dependent on information from 3D imaging modalities, such as X-ray computed tomography (CT) and magnetic resonance imaging (MRI). Still, there are some drawbacks that hamper these imaging methods. MRI remains a large and fairly expensive system and can entail a considerable maintenance cost. CT on the other hand exposes the patient to ionizing radiation which can be non-ideal, specifically for patients in treatment. Recently the idea of detecting breast cancer has shifted from anatomical information, obtained from CT and MRI, and towards modalities that obtain functional information such as the consumption of oxygen in tissue, which is relevant to processes such as tumor growth [83].

Considering the constraints at hand; a system which needs to be low cost, portable,

sensitive to functional information, useful for early detection and monitoring overall breast health, it has become clear that promising candidates are optical imaging modalities, microwave tomography, electric impedance tomography and ultrasound, which are expected to fulfill all of the conditions stated [104, 23, 13, 63]. The focus of this thesis will be optical imaging tomography for this purpose.

1.1 Non-tomographic optical modalities

Research on optical imaging started in the 1920's with a pioneering article from Max Cutler on optical transillumination images of the breast [32]. Specifically, light has been used to detect certain information such as the blood oxygenation level using pulse oximeters since the 1930's. While these methods did not generate images directly, it illustrates one way where light carries information about the material through which it travels. Cutler proposed using continuous light to detect breast lesions but this idea was quickly dropped since the intensity of light required caused the patient's skin to overheat. In the 1970's and the early 1980's significant developments were made that led to commercially available equipment for optical tomography of the breast. Gros et al. [52] introduced a concept named diaphanography, in which the breast was positioned between a visible or near-infrared light source and the physician. From this setup the doctor perceived images using his eyes alone. These advances led to the development of pulse oxymetry, laser Doppler blood-flowmetry and near infrared spectroscopy (NIRS) which then led to development of various

optical breast imaging instruments utilizing continuous-wave, frequency domain or time-domain light sources.

Pulse oxymetry originated in the 1930's and is widely used to monitor blood oxygenation, an important physiological parameter that is related to the well being of the patient. Pulse oxymeters provide accurate information on arterial blood oxygen saturation. The advantage of optical oxymeters over oxygen tension monitors, which need to be a part of the circulation or have a blood sample, is that they provide a rapid response to changes in blood oxygenation and yet are non-invasive [13].

The invention of the laser quickly gave rise to its use in medical applications. As early as the 1970's the laser was being used for laser Doppler studies of blood flow [13]. When a beam of coherent light with uniform intensity is incident on a rough surface, the reflection of the beam will not be completely uniform but will include some dark and light spots [101]. These dark spots, called speckles, are caused by light reflected many different times which causes interference at the detector. This is exactly what occurs when coherent light travels through a highly scattering sample. Additionally, if the scattering particles are moving the speckle pattern will fluctuate with a time scale which depends on the motion. This was the basis for Laser Doppler Blood Flowmetry in the 1960's [101].

Attempts at applying pulse oxymetry and laser Doppler blood flowmetry to measure hemodynamics in the brain were hindered by photodetector bandwidth limits and photon limits. In the 1970's NIRS was developed to monitor baseline changes

in total oxygenation in the brain, as revealed by the average intensity of diffusely reflected light [28, 64, 27]. Briefly, NIRS quantifies changes in chromophore concentration within highly scattering tissue by measuring the change in the photon density of light which is diffusely transported through it. The concentration change of each chromophore is then computed by relating them to the measured change in photon density. The measured change in photon density is directly related to the concentration change by the extinction coefficient of the chromophores and the effective pathlength of the tissue. The extinction coefficient is an intrinsic property of each chromophore, but the effective pathlength must be estimated for each measurement as it is heavily dependent upon the measurement setup and the optical properties of the tissue [13].

In the late 1980's and early 1990's it was soon realized that photon migration spectroscopy measurements could be extended to imaging by solving the inverse problem as is done with X-Ray computed tomography. Research investigating this possibility began in the late 1980's and is reviewed in [8, 9].

In optical imaging three measurement schemes are typically used for measuring the light transmitted through tissue. They are:

1. Time domain systems that produce illumination by short pulses of light. This pulse allows detection of the temporal distribution of photons as they exit the tissue. The shape obtained from this distribution provides information about the optical properties of tissue, especially the pathlengths and scattering of

photons.

2. Frequency-domain systems that utilize radio-frequency light intensity modulation signals. For these systems the light is on constantly but is amplitude-modulated at frequencies on the order of tens to hundreds of megahertz. This allows the absorption and scattering properties of tissue to be obtained by recording amplitude decay and phase delay of the detected signal [13].
3. Continuous wave (CW) systems emit light at a constant amplitude or are modulated at a certain frequency. These systems measure the amplitude decay of the incident light.

Out of these schemes the CW method is the simplest, least expensive, and provides the fastest data collection, however the inverse problem associated with CW does not have unique solutions, where multiple sets of optical parameters can yield identical data [29].

Due to the overall low absorption of breast tissue, it is possible to measure transmitted light through a breast, either compressed or uncompressed. In other cases where optical absorption is too strong, reflectance can be measured, such as the case for brain imaging [30], where in some situations measuring both transmission and reflection could be useful. Using the measurements schemes described above, one can estimate the absorption or different chromophore concentrations based on the measured photons transmitted through tissue. Depending on the wavelength observed by the detectors different scattering and absorption can be calculated from the measured

data.

These developments discussed in previous paragraphs led to optical imaging modalities becoming more relevant for clinical applications. This thesis will focus on CW and its usefulness for breast imaging using tomographic methods which use multiple source detector pairs that can render accurate images of the underlying structure in tissue. Accurate spatial maps of optical properties prove useful compared to the non-tomographic spectroscopy methods discussed above.

1.2 Diffuse optical tomography

In the past 15 years there has been increasing research into the use of near-infrared light to image inside the human body with tomographic approaches. Recent efforts have demonstrated that these methods can provide useful information for tumor location and optical parameters. In this setting tissue is illuminated with spatially distributed sources and measurement taken with an array of sources where tomographic algorithms can be used to reconstruct slice images of the medium. These methods can provide better localization of abnormalities in tissue and optical properties by rendering accurate maps of the imaging domain and in some cases, spatial-temporal profiles of chromophore concentrations (oxy- and deoxy-hemoglobin, water and lipids etc.) which convey functional information about the body [72]. One of the techniques of interest is diffuse optical tomography (DOT) [48]. DOT uses infrared light which is, as was discussed above, sensitive to the functional state of tissue such as the

consumption of oxygen which is possibly relevant to processes such as the growth of tumors, vascular structures as well as the state of brain activity. Specifically, existing clinical studies have related concentrations of total hemoglobin with tumor locations, which is promising for using light to locate tumors. Although many applications have been shown for the DOT method the most promising ones are for brain imaging and breast imaging. For the case of brain the dominant method is still topography, which monitors haemodynamic and oxygenation changes, while breast imaging serves as our focus in this thesis [42, 92].

Throughout this work we consider a standalone DOT device [44]. Although a standalone device is considered, it is interesting to compare DOT to X-ray especially since DOT offers functional information which can be hard to obtain with X-ray mammography, whereas the later gives highly detailed anatomical information. Tumor detection in X-ray is for example done by the identification of microcalcification characteristic of malignant lesions, while optical mammography measures changes in blood perfusion of the tissue surrounding the tumor. These changes occur early in a tumor's growth and can affect a relatively large area [95]. Some reasearches have proposed that DOT be combined with other modalities, for example Li et al. [71] proposed that the contrast seen in X-ray images should be assumed to be proportional to the DOT contrast. A linear least-squares type of DOT image formation problem was then posed to use the information from the X-ray measurements. The image reconstruction was regularized using the Tikhonov method which is similar to

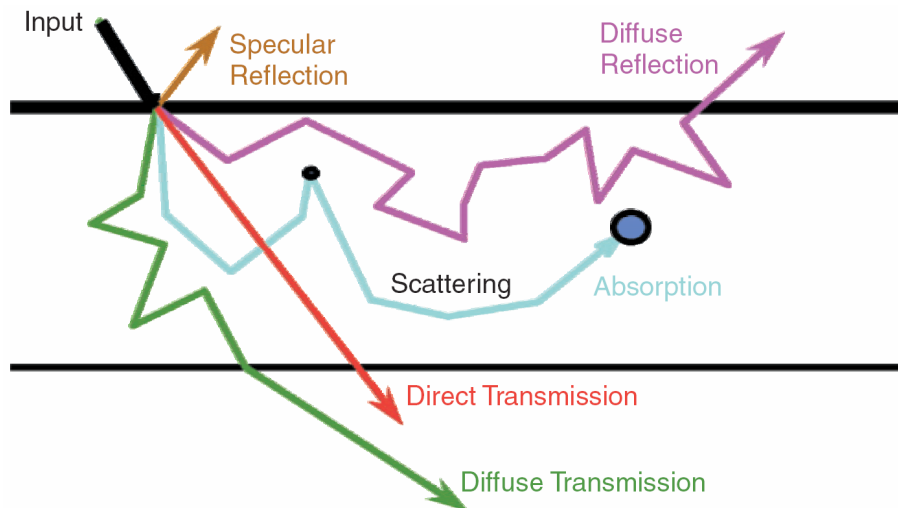


Figure 1.1: *The process of photons passing through tissue [13]. Black line represents light injected into the medium, where part of it is reflected right at the surface, represented by the brown arrow. Purple line represents diffuse reflectance, where light is scattered out the same side as the injected light. Blue line represent scattered and absorbed photons, where the green arrow is scattered photons that travel to the detector. Finally, red line represent ballistic photons that undergo no scattering events.*

what is tested in Chapter 5. The regularization in general was based on regions of interest, mainly the tumor regions and background regions. Additionally, through simulation they were able to show that their method improved the contrast-to-noise ratio and resolution in the reconstructed image. Although, pairing DOT with other imaging modalities is promising, the work in this thesis focuses on DOT as a standalone modality, serving as an independent tool to estimate female breast health, without information gathered from X-ray imaging or other modalities. Additionally, as has been discussed, mobility, cost and patient comfort are issues that are easier to solve when considering a standalone DOT device.

As discussed above, the functional information accessible by DOT shows significant promise to apply it to breast cancer imaging. The use of near-infrared light is essentially electromagnetic radiation but is at a significantly lower energy than CT, making this method less harmful. Operating in the infrared spectrum, 650-950nm, gives us a range which is sometime called the window of transparency [95]. In this window light propagates relatively far into the tissue (on the order of centimeters) before being absorbed, thereby allowing us to probe quite deeply. Additionally, light is also scattered within the tissue as it interacts with subsurface inhomogeneities. This process is illustrated in Fig. 1.1. Within the window, light is absorbed and scattered differently at different wavelengths depending on the space-varying oxygenation state of the tissue. This relation gives us a way to use multiple wavelengths when estimating chromophore concentrations, the recovery of which is the main interest of this thesis. Using different wavelengths, performing multispectral measurements or using a higher number of wavelength (i.e., collecting a “hyperspectral” dataset) , more information is added to the imaging problem thereby improving our ability to determine the concentrations of chromophores and ultimately detect cancers using the methods discussed in the later part of this thesis. With this method it is possible to increase the effectiveness and accuracy of the DOT method.

Recovering functional information with DOT is extremely useful if framed in the early detection framework discussed above. Although our research initially considered the case of tumor anomalies in breast tissue, it is clear that overall vascular structures

need to be considered. Traditional imaging modalities, such as X-ray and CT, which rely on anatomical information are insensitive to tumors in early stages of growth due to smaller sizes and lower attenuation of X-rays, which focuses early detection on the recovery of functional information of the breast such as oxygenation and vascularity using optical modalities [23]. This drives the need to be able to discriminate and estimate structures embedded in breast tissue, including major vascular structure. To this end, work in this thesis will involve how we are able to estimate three-dimensional (3D) tubular structures, relating to vascular shapes detected in breast tissue, by extending the method we have developed for image reconstruction for DOT. To estimate these structures and parameters the light propagation through tissue must be modeled. Although the interaction of light and tissue is a highly complex problem, there have been significant advances in recent years to solve the problem efficiently, both in terms of theoretically modeling the physics and developing useful codes for simulating the process.

Due to these advances, the DOT method has become the prime candidate for future breast cancer detection systems. X-ray radiation in CT travels generally in a straight line, excluding Compton and Rayleigh scattering, resulting in a much simpler problem than what is found for optical modalities. In the case of diffuse optical tomography the photon's mean free path of travel between two scattering events is very short due to high scattering, most often only a fraction of a millimeter. Because of this, most photons travelling through a human breast undergoes numerous scattering

events. Thus, unlike CT where the physics of the problem is basically straight line propagation and yields a linear relationship between the quantity of interest tissue density and the observed data, for DOT a more complex model is required [95]. More specifically, the physics of light interaction with the tissue is well modeled using the diffusion approximation to the radiative transport equation (RTE) which yields a nonlinear relationship between the chromophore concentrations and the observations of scattered light [95]. This is called the diffusion equation which expresses the photon density as a function of absorption coefficient and scattering coefficient and solving it will provide the forward model needed to solve the inverse problem [48, 13].

The significant computational challenge of DOT is that it is an ill-posed inverse scattering problem due to the physics of the diffusion process just described and in some cases the limited ability to collect quantities of data. Additionally, another challenge is the fact that the measurement is related non-linearly to the parameters of interest, which is often addressed with linear approximations [13]. The ill-posedness poses a more substantive problem than the non-linearity since it leads to large changes in parameters when fairly small changes occur in the data. In some sense this is a physics-based phenomenon, which means there is a lack of sensitivity in the data to the parameters. It also means that in the image formation process (if done naively), small changes in the data from noise and unmodeled effects can cause very large changes to the estimated profiles. In other words the reconstruction process is highly sensitive to small perturbations in the data. Adding to these difficulties is the fact that in many

cases one seeks to recover more degrees of freedom (voxel values times number of chromophores) than one has data points [13]. Taken together, the physics-based ill-posedness coupled with non-linearity pose a significant challenge for recovering optical properties in DOT. Additionally, this thesis considers limited acquisition geometries that result in underdetermined systems that dramatically complicates our ability to stably recover useful information about the state of the tissue from DOT data. While there do exist camera based systems which are overdetermined, where a significant amount of source-detector pairs are placed around the medium, our work focuses around a specific source detector setup described in Chapter 4 [86].

Considering anomalous structures like tumors or simply regions of interest, like vessels, the imaging problem can be formed as a segmentation problem, detecting one class of objects from the background [7]. This approach can help to constrain the problem, decreasing the need for explicit regularization for the inverse problem. Similarly, shape-based methods that utilize segmentation methods are promising for performing image reconstruction by taking advantage of information from other imaging modalities such as optical or X-ray mammography, where prior information regarding tumor location, vessel structure or adipose tissue can be implemented [38].

Researchers have developed several instrumentation types for optical mammography, some are similar to X-ray by compressing the breast but others use cone like arrangement of sources and detectors which do not require compression [24, 113]. When the compression technique is used a laser source illuminates on one plate,

which is transparent while a detector on the opposite plate measures over several measurement locations for each source position [95]. This arrangement reduces the thickness of the transilluminated tissue. This technique has of course been used for several years in X-ray mammography and has been proven to improve the detectability of deeply embedded objects. One down side of the compression method is that it can cause blood to drain from the breast, thereby unpredictably altering the optical properties [19].

The other method, with sources and detectors situated in a plane around an uncompressed breast, has the patient lying prone on a table with the unsupported breast suspended in a cavity [86]. The data acquisition might consist of a set of fixed sources and detectors or a rotating system that scans the breast's surface. This setup can provide a more complete sampling data over the boundary, but makes defining the problem's geometry more difficult and requires higher sensitivity of detectors, due to the longer photon path. This results in higher sensitivity near the skin but much lower near the center of the breast. This also has the advantage that it should be much more comfortable for the patient since numerous patients have felt the compression method to be uncomfortable and sometimes painful.

1.3 The purpose of this work

The key contribution of this work is developing a method to perform shape-based image reconstruction for DOT, both in terms of tumor detection through recovering chromophore concentrations utilizing hyperspectral data, and estimating vascular structures of breast tissue. For reconstructing chromophore concentrations we focus on two-dimensional (2D) images, based on its simplicity and usefulness to judge the performance of our method using both simulated data and experimental measurements. Considering the vascular structures we extend our method of generating 2D images to estimate tubular objects representing vessels in breast tissue, using a simplified model with extremely limited data.

In traditional inversion methods for DOT image regions are discretized into large collections of voxels over which absorption, scattering or chromophore concentrations are assumed constant. In this framework inversion needs to be carried out for a large number of unknowns to estimate the image representing optical properties of the breast. Due to the previously discussed ill-posedness of the problem pixel based reconstruction can pose significant challenges for image recovery. Instead of developing methods to improve a pixel or voxel based reconstructions we utilize a shape-based method which assumes that areas of interest in breast tissue can be divided into two distinct piece-wise constant regions: background breast tissue, and structures of interest, either anomalous areas or tubular structures, representing blood vessels. We then aim to recover a low order accurate estimation of the underlying structures for

scenarios where the optical absorption contrast between the background and structure of interest is within a range commonly found in realistic situations [44].

Our method emphasizes the use of simplified models describing the photon migration through tissue, where accurate representation of areas of interest can be achieved by reducing the dimensionality of the problem. This renders the inversion computationally feasible and easily expandable for other accurate models calculated for a variety of geometries.

1.4 Thesis Outline

The thesis is structured as follows. In Chapter 2 we discuss the fundamental concepts of DOT, for image reconstruction and review previous efforts to recover images of the female breast using DOT. In Chapter 3 the forward models used to compute the photon migration in several different scenarios considered in this thesis are detailed. Chapter 4 discusses experimental methods employed in this thesis to verify our claims. In Chapter 5 the low order shape based method is described and compared to a pixel based method. Chapter 6 contains brief discussion regarding a dictionary method for the low order method followed by our method for recovering 3D structures with 2D primitives in Chapter 7. Finally, Chapter 8 contains discussion regarding future efforts for this project.

Chapter 2

Background

This section will briefly discuss the formulation and concepts to be used in this thesis. The main problem of recovering images will be discussed in general to be followed with more detailed discussion in Chapters 5, 6 and 7. Throughout we reference major works in the field of image reconstruction for DOT, which allows the reader to further explore the topic.

2.1 Image reconstruction for DOT

The process of recovering images for DOT involves defining the forward problem, which models the transport of photons through the relevant medium, as well as addressing the challenges of the inverse problem mentioned in Chapter 1.

Lets assume that the domain to be imaged is defined by \mathcal{F} , a compact domain in \mathbb{R}^n , $n \geq 2$, where a physical model \mathbf{K} acts on its properties. In the case of our

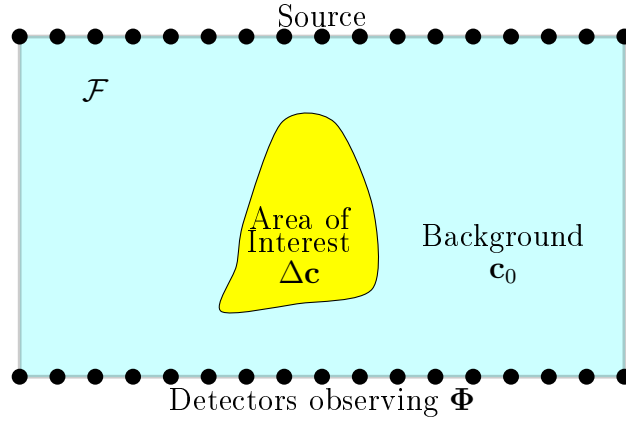


Figure 2.1: *Basic setup of the imaging problem in this thesis. It demonstrates where optical properties \mathbf{c} are separated into foreground and background. The model \mathbf{K} acts on the entire domain, \mathcal{F} , to generate Φ*

application these properties include optical absorption or chromophore concentrations and scattering defined by a vector of parameters, \mathbf{c} , where the effect of \mathbf{K} on \mathcal{F} generates a set of observations, or a measurement, Φ . As discussed in Chapter 1 the measurement can be CW, time-domain or frequency domain data, where for this thesis we consider the CW case. We define a non-linear forward model represented by

$$\Phi = \mathbf{K}(\mathbf{c}) \quad (2.1)$$

where \mathbf{c} itself belongs to a Hilbert space $\mathbb{S}_{\mathbf{c}}$. We define the inverse problem—the process of recovering an estimate $\hat{\mathbf{c}}$ of \mathbf{c} from the measurement Φ —as a variational approach where we set up the estimation of $\hat{\mathbf{c}}$ as an optimization problem defining

the inverse problem as

$$\begin{aligned}\hat{\mathbf{c}} &= \operatorname{argmin}_c \mathcal{G}(c) \\ \text{where} \\ \mathcal{G}(\mathbf{c}) &= \frac{1}{2} \|\mathbf{K}(\mathbf{c}) - \Phi\|_2^2.\end{aligned}\tag{2.2}$$

The data mismatch term in (2.2) is in a least square form which assumes that the estimate, $\hat{\mathbf{c}}$, is mathematically consistent with the data, Φ . However, the underlying physics of photon migration, and limited data generally acquired in a traditional DOT measurement setup, result in a solution that is highly sensitive to noise and system errors. Because of this challenge, and the fact that the basic forward model in (2.1) is non-linear, significant care is required when performing the reconstruction.

As detailed by Arridge [3] researchers have taken established solution methods from other applications and extended them to the optical tomography problem. Methods adapted from computed tomography have used the assumption that the Radon transform could be applied to the DOT problem, where closed form solutions and backprojection schemes are proposed [49]. Methods using linear matrix formulation that are analogous to transfer functions in single photon emission computed tomography have also been considered [49].

Essentially there are two types of image reconstruction schemes for DOT; linear methods, where approximations are applied to linearize (2.1) and non-linear methods that can be more accurate, but more computationally intensive. The remainder of this chapter will discuss these different methods and regularization techniques applied

to the optimization problem in (2.2).

2.2 Linear approximations

The non-linear problem in (2.1) can be linearized if certain assumptions are made of the imaging medium. Detailed by Gibson et al. [49] the model can be linearized if the actual optical properties are close to an initial estimate $\hat{\mathbf{c}}_0$ and the measured data Φ are close to the simulated data $\Phi_0 = \mathbf{K}(\mathbf{c}_0)$, generated by the forward model. This approach is frequently used in difference imaging where data is collected before and after an event that changes the optical properties, for example the injection of a contrast agent or breathing exercise [49]. The linear approximation is defined by Taylor series as

$$\Phi = \Phi_0 + \mathbf{K}'(\hat{\mathbf{c}}_0)(\mathbf{c} - \hat{\mathbf{c}}_0) + \mathbf{K}''(\hat{\mathbf{c}}_0)(\mathbf{c} - \hat{\mathbf{c}}_0)^2 + \dots \quad (2.3)$$

where \mathbf{K}' and \mathbf{K}'' are the first- and second-order Fréchet derivatives of \mathbf{K} [4]. The Fréchet derivative can be considered a linear integral operator that maps functions in image space to measurement space. The kernel of this integral can be computed by analytical Green's functions, an approach used by Boas et al [14].

By neglecting higher order terms and strictly considering changes in optical properties $\Delta \mathbf{c} = \mathbf{c} - \mathbf{c}_0$ and data $\Delta \Phi = \Phi - \Phi_0$ the linear problem in (2.3) can be expressed as

$$\Delta \Phi = \mathbf{K} \Delta \mathbf{c} \quad (2.4)$$

where \mathbf{K} is now the linear forward model. Ignoring the higher order terms this way gives way to implementing two different linear approximations, the Born and Rytov approximations, respectively.

2.2.1 Born Approximation

Sometimes referred to as single scatter method, the Born approximation consists of taking the incident field in place of the total field as the driving field at each point in the scatterer. This is equal to writing the total field as a sum of an incident field, Φ^i and a scattered field Φ^s given by

$$\Phi = \Phi^i + \Phi^s. \quad (2.5)$$

Physically it amounts to treating each point in an inhomogeneity as if it existed in isolation from the rest of the inhomogeneity ignoring the contributions of perturbations of the scattered field from one part of an inhomogeneity on the field incident on another part [48]. It is well established that the Born approximation deviates from the true result when the perturbation $\Delta\mathbf{c}$ exceeds a certain limit [91] where extensive analysis has been performed on the error in optical absorption images due to the approximation [54] and error modeling has been used to perform corrections for the Born approximation [103]. However, taking these limitations into account, the Born approximation can be a useful tool to simplify the inverse problem and has been extensively used in DOT, both for simulations and clinical setting [48, 105]. It provides a straightforward method to compute and linearize the forward model, which can be

used to test reconstruction algorithms. Additionally, as noted by [91] the method can be extended into higher orders, rendering more accurate results. For the purpose of this thesis the Born approximation is used, and is discussed further in Chapter 3.

2.2.2 Rytov Approximation

Another approach is the Rytov Approximation which is computed by linearizing the log intensity which reduces the dynamic range of Φ , which assumes that the total field can be computed as

$$\Phi = \Phi^i \exp(\Phi^s). \quad (2.6)$$

It has been reported that Rytov approximation is better suited for experimental data, in that it is less ill-posed than the Born Approximation [3], where it accounts for some non-linear saturation due to increasing perturbation in the absorption coefficient. However, where the Born approximation is only suitable for lower optical contrasts, the Rytov approximation assumes that the scattered wave varies slowly, thus being more suitable for larger perturbations [81]. Boas [11] reported that the Rytov approximation has a discrepancy of about four times greater than the Born approximation, but suggested that the Rytov approximation could be empirically modified. Recently the Rytov approximation has successfully been employed for image reconstruction for experimental and clinical measurements [79].

Using either of these linear approximations allows for directly inverting the \mathbf{K}

matrix in (2.4). To this end a variety of common techniques are available including singular value decomposition, truncated singular value decomposition, Tikhonov regularization or algebraic reconstruction technique (ART) [48].

2.3 Regularization techniques

Before applying regularization techniques, prior anatomical information can be considered for the purpose of regularizing the solution of the inverse problem that can improve estimation of chromophore concentrations. Such prior information can be included in the forward model, which usually involves implementing complex geometries with numerical models. To this end various methods can be applied, including the finite difference method discussed in Chapter 3. Including this kind of information in the forward model allows for taking advantage of anatomical prior information while using various forward models, as it has been shown that it is beneficial for both linear and non-linear reconstructions [12]. Notably, prior information from X-ray images has proven to be useful to define the segmentation between adipose and fibroglandular tissue in the breast. Fang et al [38] demonstrated that constructing a regularization matrix that incorporated structural priors from X-ray data into a finite element DOT inversion resulted in accurate estimation for clinical data.

When prior structural information is not available, various techniques exist to regularize the inverse solution. Throughout this thesis, we consider standalone DOT device, and as such structural prior information is hard to come by. This requires

implementing other methods for regularizing the inverse solution.

2.3.1 Reconstruction using the singular value decomposition

For \mathbf{K} a $m \times p$ matrix with $m > p$, the singular value decomposition (SVD) takes the form

$$\mathbf{K} = \mathbf{U}\mathbf{\Sigma}\mathbf{V}^T = \sum_{i=1}^p u_i \sigma_i v_i^T \quad (2.7)$$

where \mathbf{U} is an $m \times m$ unitary matrix, the matrix $\mathbf{\Sigma}$ is $m \times p$ diagonal matrix with nonnegative real numbers on the diagonal, and \mathbf{V} is an $p \times p$ unitary matrix.

The common convention is to order the diagonal entries $\Sigma_{i,j}$ in non-increasing fashion. The diagonal entries of $\mathbf{\Sigma}$ are known as the singular values of \mathbf{K} . The number of non-zero singular values, r , is the rank of \mathbf{K} . Then $\mathbf{\Sigma}$ is written as:

$$\mathbf{\Sigma} = \text{diag}(\sigma_1, \sigma_2, \dots, \sigma_r) \quad (2.8)$$

The pseudo inverse of \mathbf{K} , \mathbf{K}^+ , is defined as

$$\mathbf{K}^+ = \mathbf{V}\mathbf{\Sigma}^+\mathbf{U}^T \quad (2.9)$$

where $\mathbf{\Sigma}^+$ is formed by

$$\mathbf{\Sigma}^+ = \text{diag}(\sigma_1^{-1}, \sigma_2^{-1}, \dots, \sigma_r^{-1}) \quad (2.10)$$

This pseudo inverse is then used to obtain $\widehat{\Delta\mathbf{c}} = \mathbf{K}^+ \Delta\Phi$

$$\widehat{\Delta\mathbf{c}} = \sum_{i=1}^r \frac{1}{\sigma_i} v_i \langle u_i, \Delta\phi_i \rangle = \mathbf{V}\mathbf{\Sigma}^+\mathbf{U}^T \Delta\Phi \quad (2.11)$$

When dealing with a matrix, \mathbf{K} , where the singular values decay over many orders of magnitude towards zero, like in the DOT case, the problem becomes more complicated due to the evaluation of σ^{-1} .

To see how the SVD gives insight into the ill-conditioning of \mathbf{K} , consider the following relations [57]:

$$\begin{aligned} \mathbf{K}\mathbf{v}_i &= \sigma_i\mathbf{u}_i, & \|\mathbf{K}\mathbf{v}_i\|_2 &= \sigma_i \\ \mathbf{K}^T\mathbf{u}_i &= \sigma_i\mathbf{v}_i, & \|\mathbf{K}^T\mathbf{u}_i\|_2 &= \sigma_i \end{aligned} \tag{2.12}$$

where \mathbf{u}_i , \mathbf{v}_i are left and right singular vectors, basis for the row and column spaces of \mathbf{K} , respectively and represent the i^{th} elements in the \mathbf{V} and \mathbf{U} matrices. It can be seen that a small singular value σ_i , relative to $\sigma_1 = \|\mathbf{K}\|_2$, means that there exists a certain linear combination of the columns of \mathbf{K} , characterized by the elements of the right singular vector \mathbf{v}_i , such that $\|\mathbf{K}\mathbf{v}_i\|_2 = \sigma_i$ is small. The same holds for u_i and the rows of \mathbf{K} . In other words, a situation with one or more small σ_i implies that \mathbf{K} is nearly rank deficient, and the vectors \mathbf{u}_i and \mathbf{v}_i associated with the small σ_i are the numerical null vectors of \mathbf{K}^T and \mathbf{K} respectively. From this property it can be concluded that the matrix corresponding to a discrete ill-posed problem is always highly ill-conditioned.

The SVD is an invaluable tool for analysis of problems with ill-conditioned matrices and the truncated SVD (described below) has been used successfully to solve a variety of ill-posed problems of the form 2.4. When $\Delta\Phi$ in (2.4) is perturbed by errors then the solution to the perturbed problem is very likely to be dominated by

large amplitude, high frequency errors with structure of singular vectors correlated to small singular values [56]. It is therefore necessary to use some sort of regularization to compute a solution that is less sensitive to the perturbations. The Tikhonov method is commonly used in this respect and will be discussed in detail in Section 2.3. An alternative method for regularization of (2.2) is the Truncated SVD. TSVD uses a reduced rank approximation to \mathbf{K} that is obtained by setting all but the first l largest singular values equal to zero and using only the first columns of \mathbf{U} and \mathbf{V} . Thus the TSVD solution, $\widehat{\Delta\mathbf{c}}_l$, is defined by

$$\begin{aligned}\widehat{\Delta\mathbf{c}}_l &\approx \sum_{i=1}^l v_i \langle u_i, g \rangle = \mathbf{V} \Sigma_l^+ \mathbf{U}^T \Delta\Phi \quad \text{where} \\ \Sigma_l^+ &= \text{diag}(\sigma_1^{-1}, \sigma_2^{-1}, \dots, \sigma_l^{-1}, 0, \dots, 0)\end{aligned}$$

The integer l is called the truncation parameter. The TSVD becomes especially useful when dealing with ill-posed problems such as the forward model matrices for the DOT problem which are often poorly conditioned with a very wide range of singular values. The singular value spectrum for the DOT problem can have a range of seven orders of magnitude in the singular values [48].

2.3.2 Tikhonov Regularization

Considering the objective function in (2.2) the ill-posed inverse problem poses an instability in the solution with respect to small variations. This results in non-uniqueness of solutions where large changes in optical properties result in small changes in the

estimated solution to (2.2) which suggests the importance of augmenting the objective function by including regularization terms which modifies the objective function. This approach allows for more accurate reconstruction compared to TSVD where regularization terms can be specifically defined to incorporate prior information or suppress edge artifacts. The objective function is then defined by

$$\mathcal{G}(\mathbf{c}) = \|\mathbf{K}(\mathbf{c}) - \Phi\|_2^2 + \alpha\|\mathbf{L}\mathbf{c}\|^2. \quad (2.13)$$

The second term includes the regularization matrix \mathbf{L} weighted by the regularization parameter α . Considering the linearized form of the forward model in (2.4) the objective function in (2.13) can be expressed by

$$\mathcal{G} = (\mathbf{K}\widehat{\Delta\mathbf{c}} - \Delta\Phi)^T(\mathbf{K}\widehat{\Delta\mathbf{c}} - \Delta\Phi) + \alpha\widehat{\Delta\mathbf{c}}^T \mathbf{L}^T \mathbf{L} \widehat{\Delta\mathbf{c}}. \quad (2.14)$$

Optimizing this equation is done by taking the partial derivative with respect to $\widehat{\Delta\mathbf{c}}$ and setting equal to zero

$$\begin{aligned} \frac{\delta\mathcal{G}}{\delta\widehat{\Delta\mathbf{c}}} &= 2\mathbf{K}^T \mathbf{K} \widehat{\Delta\mathbf{c}} - 2\mathbf{K}^T \Delta\Phi + 2\alpha\mathbf{L}^T \mathbf{L} \widehat{\Delta\mathbf{c}} \\ 0 &= 2\mathbf{K}^T \mathbf{K} \widehat{\Delta\mathbf{c}} - 2\mathbf{K}^T \Delta\Phi + 2\alpha\mathbf{L}^T \mathbf{L} \widehat{\Delta\mathbf{c}} \\ \widehat{\Delta\mathbf{c}} &= (\mathbf{K}^T \mathbf{K} + \alpha\mathbf{L}^T \mathbf{L})^{-1} \mathbf{K}^T \Phi \end{aligned} \quad (2.15)$$

There are multiple options for choice of the regularization matrix, \mathbf{L} , which serves the purpose of regularizing the solution to increase the quality of the reconstructed image. In essence its choice requires taking into account *a priori* information regarding the imaging medium at hand, which for our application, is breast tissue. When it is chosen to be identity the implicit prior assumption is that the concentrations of

chromophores are small, when α is chosen to be sufficiently large. When the imaging medium is discretized on a relatively coarse grid the optical properties in the breast can be considered being slowly varying, so the system can be assumed to be smooth. This prior information leading to a reasonable choice of a spatial differential operator as \mathbf{L} .

The challenge in choosing the α parameter is of even greater importance when implementing regularization in (2.13). Formal methods exist and are widely employed, such as generalized cross-validation (GCV) or the L-curve method, which usually verified with other error metrics and visual inspection. In the L-curve method a plot of $\log(\|\mathbf{L}\hat{\mathbf{c}}\|^2)$ is generated against $\log(\|\mathbf{W}(\mathbf{K}(\hat{\mathbf{c}}) - \mathbf{\Phi})\|^2)$ as α is varied. Larger α makes the system better conditioned, but this new augmented system is farther away from the original system, without regularization. Assuming no noise, any sufficiently small value of α will produce the same result, but with increasing noise the need of larger α grows. Gradient like regularization matrix and the L-curve method is applied for multiple chromophores for pixel based reconstruction as in Chapter 5, while an adjusted regularization matrix is utilized for estimating 3D shapes in Chapter 7.

2.4 Non-linear reconstruction

The aim of non-linear image reconstruction is to calculate optical properties at each point within the model using measurements of light fluence from the tissue surface. This is performed if the inverse problem cannot be assumed to be a recovery of

values relative to a known background or a difference measurement, but a recovery of absolute values of the optical properties. Solving the non-linear problem involves iterating the objective function \mathcal{G} in (2.2) which minimizes the mismatch between modeled data from $\mathbf{K}(\hat{\mathbf{c}})$ and measured data Φ . As before in the case of breast imaging $\hat{\mathbf{c}}$ is the images of optical properties. Finding the best estimate of \mathbf{c} to minimize the data mismatch term requires an iterative reconstruction, which can be separated into two distinct approaches; gradient-based reconstruction, which has been extensively studied by Arridge & Schiewer [6, 3] and Hielser et al [60], or Newton-like methods [93].

Gradient based methods avoid the problem of Newton methods which involve the algorithm becoming intractable as the size of the problem domain increases [6]. In gradient based algorithms such as conjugate gradient, a set of conjugate search directions is generated to find the minimum of the objective function. At each iteration step a one-dimensional line minimization along the current search direction is performed. The update in gradient methods is computed from initial value $\mathbf{c}^{(0)}$ to obtain the estimate $\hat{\mathbf{c}}$

$$\hat{\mathbf{c}}^{(i+1)} = \hat{\mathbf{c}}^{(i)} - \rho^{(i)} \mathcal{G}'(\hat{\mathbf{c}}) \quad (2.16)$$

where i represents the number of iteration, where each step is taken along the minus derivative direction of \mathcal{G} , ρ is the step size which needs to reduce cost and be large enough to reduce number of iterations and \mathcal{G}' represents the Fréchet derivative of \mathcal{G} . It should be noted that the gradient based method can be sensitive to variable

scaling, which can effect problems where estimation is performed for different types of unknowns with different orders of intensity [49]. This problem is encountered in shape-based methods, where estimation is performed for both value of absorption and shape, detailed in Chapter 5. This sensitivity can also be encountered when inverting multiple chromophores, and scattering amplitude, where the parameters with larger sensitivities are updated faster compared to low sensitivity unknowns, which does not iterate some chromophore images from initial guess.

Newton methods seek to find a zero of the gradient of \mathcal{G} by expanding the estimate at each iteration with Taylor expansion. This leads to an update at each iteration computed by

$$(\mathbf{J}^T \mathbf{J} + \rho \mathbf{H}) \mathbf{h} = -\mathbf{J}^T \boldsymbol{\epsilon} \text{ with } \rho \geq 0 \quad (2.17)$$

where $\mathbf{J} = \mathbf{K}'$ is the Jacobian of the data mismatch term and \mathbf{H} is a Hessian matrix. Commonly employed algorithm used to solve the non-linear reconstruction with Newton methods is the Levenberg Marquardt algorithm which involves defining a large initial ρ and reducing it dynamically through iterations [3]. Reconstructions for the shape-based method in this thesis are performed implementing the Levenberg-Marquardt algorithm, detailed in Chapter 5.

What these two approaches share is that great care has to be taken when defining when the optimal solution $\hat{\mathbf{c}}$ has been achieved. This usually involves stopping the iteration when the update to $\hat{\mathbf{c}}$ is below a certain threshold, or a defined noise level has been reached. Working with the Levenberg-Marquardt algorithm in this thesis

we chose the second stopping criteria, detailed in Chapter 5.

2.5 Shape Based Methods

Wide variety of applied imaging problems involve determining a two dimensional (2D) area or three-dimensional (3D) volume in a larger field of regard. In the context of this thesis, this area of interest can be a cancerous tumor or a tubular like structure representing vessels in breast tissue. One way to approach these problems and estimation of these structures is to reconstruct regions of interest without constraints of the shapes of anomalous locations [59, 48, 33]. These reconstructions require post processing where the segments of the recovered images are identified in terms of background and area of interest. An alternative way is to directly estimate areas of interest and the values of optical properties associated with each. These approaches are known as shape-based methods and have been gaining interest for optical imaging methods [1, 112, 16, 67, 7].

Shape-based methods involve separating the estimation of \mathbf{c} in (2.1) into recovery of two distinct classes, foreground and background. This approach then estimates the boundary of the area of interest, or foreground, and assigns a value for optical properties inside this region and outside for background. The formulation presented in this thesis assumes that values in the two separate areas are piecewise constant, however adding texture functions to estimate variable concentrations in these areas is straightforward [1]. Throughout this thesis we separate \mathbf{c} by defining it over the

domain \mathcal{F} as

$$\mathbf{c} = c^a \chi(x, y) + c^b [1 - \chi(x, y)] \quad (2.18)$$

Here the function χ is defined as a characteristic function defined as 1 inside of the boundary of \mathbf{c} defined as Ω and 0 outside of it. Recovering the boundary of Ω is the main goal in shape-based estimation, and is shown within the imaging domain \mathcal{F} in Fig. 2.2. Estimating this boundary can be done by evaluating a dense collection of pixels, as is done in traditional image reconstruction for optical imaging. Another approach is to parametrize the boundary of Ω and generate an estimate of \mathbf{c} by estimating derivatives of the domain mapping the measurement to the optical parameters of interest. Constraining the image formation with this segmentation approach and a parametric curve lessens the need of added regularization terms in the objective function (2.2) since the estimate is implicitly regularized through the formulation [1]. A significant drawback to this method is that *a priori* information is required to define the number of areas of interest which is a significant issue concerning medical imaging modalities where the ground truth is hard to come by.

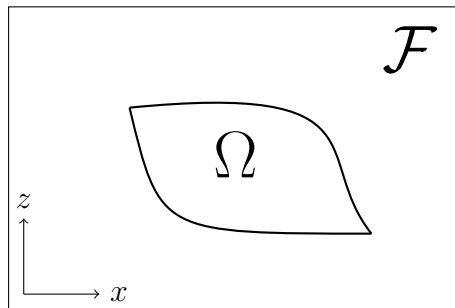


Figure 2.2: *Definition of anomalous region Ω within the imaging domain \mathcal{F} used for shape-based methods.*

The need of prior information to estimate the curve can be circumvented by estimating the boundary of Ω using a level-set representation of the unknown parameters [114]. This is the primary approach considered in this thesis. In [34] level sets were used in a two-step method for shape estimation assuming that prior information of the absorption parameter was known. Schweiger et al. [94] and Kilmer et al. [67] employed level sets for the DOT problem estimating parameter distributions using a piecewise basis. Arridge et al. [7] investigated shape based methods by estimating level-sets, specifically investigating an explicit method using basis functions and an implicit shape reconstruction to recover absorption and diffusion coefficients assuming a known background [7]. For a detailed review of the use of level sets in inverse scattering problems we point the reader to [35].

The approach we consider in this thesis is significantly different from those in [94, 34, 7]. In addition to the fact that none of these papers have considered the fully hyperspectral case, some of these methods [94, 34, 67] require the recovery of unknown quantities defined on a fine scale pixelated discretization of the region of interest. More specifically in [7] absorption and scattering are estimated using level sets assuming those of the background are known. With the Born approximation we assume the absorption and diffusion coefficients are known in the background but here we estimate chromophore concentrations and scattering amplitude of the object of interest as well as chromophore concentration in the background. Traditional image reconstructions methods use a pixel-based grid, estimating each pixel unconstrained by segmentation,

while traditional level set methods work with a level set function defined on a pixel-based grid. In both cases, regularization is required to obtain adequate results and one is faced with the corresponding challenge of choosing regularization parameters [85, 94].

In this thesis we consider the use of a shape-based approach to the hyperspectral DOT problem based on a newly-developed parametric level set (PaLS) formulation. In [1], a basis function expansion was used to provide a low order representation of the level set function and yielded more accurate results for a number of highly ill-posed inverse problems including a restricted form of the DOT problem where a single wavelength was employed to determine only optical absorption. The method required no explicit regularization and, due to the low-order nature of the model (number of parameters significantly less than number of pixels) was amenable to Newton-type inversion algorithms known to converge more rapidly than gradient-based schemes. Moreover, in [1] it was demonstrated that experiments indicated a robustness to the selection of initial guess for the inversion algorithm.

Considering the case of DOT, the breast is a highly heterogeneous medium, whereas in the level set method we assume the images to be recovered to be piecewise constant. This assumption is supported in the literature. For example Schweiger et al. assumed anatomical prior information to derive a piecewise constant region basis [92]. In this thesis the choice of the piece-wise approximation is sufficient due to the

underdetermined nature of our setup, where data is acquired with limited source-detector pairs. This results in a high ill-posedness where high resolution information is difficult to recover, making the piece-wise approximation useful.

Considering the heterogeneous medium encountered in this application, we explore the application of implementing the low-order model by taking advantage of redundant dictionaries. This entails essentially creating a large matrix, containing a library of shapes that can be used to estimate the underlying structure. In this context, a sparse representation means recovering the unknown optical properties by including only few elements from the dictionary matrix.

2.5.1 Primitives for 3D shape estimation

Considering the case of estimating vascular structures of the breast, which as discussed in Chapter 1 is important for breast imaging, the recovery of 3D structures is vital. To this end researchers have implemented accurate numerical models which discretize the imaging medium into voxels and recover 3D structures by assigning values to each element [31], or reconstructed cross-sections of 3D objects to estimate their total volume and location [33]. In the case of the ill-posed DOT problem, this can be computationally intensive and hard to generate voxel meshes for different geometries without prior information.

An alternative approach to reconstruction of 3D shapes is presented in [18]. In this paper the authors represent this 3D object by a collection of vertically stacked

unit height cylinders, which they refer to as *primitives*. The cross sectional density of each primitive is represented as a function, $f(\mathbf{r}, \gamma)$, of a position vector \mathbf{r} and a vector of shape parameters γ . Specifically, in [18] the function $f(\mathbf{r}, \gamma)$ is the indicator function for an ellipse where the shape of each primitive is defined by a parameter vector that holds the center and radius of the ellipse, the ratio of its semi-axes and the orientation angle between its semi-axes. Under this model, each object primitive is centered at a point, which corresponds to the vertical positioning of the center axis for that primitive. However, since this model was developed for generalized cylinders, where a known training set or prior information would optimize the selection of the model parameters it is most effective when the objects are modeled as such [18]. Additionally, the approach in [18] restricted structures to not intersect in 3D space and implemented a statistical method to determine if primitives in adjacent slices should be connected.

Inspired by [18], we introduce a new, flexible approach to the modeling and estimation of 3D shapes. We define a 3D object using a set of 2D shapes, which we also refer to as primitives [18]. Our model defines each primitive as a cross-section, an infinitesimally thin area, whose structure is defined by a vector of parameters that consists of a collection of basis functions defined by their center locations, weighting factors and axis length, or dilation. This formulation allows for implementation of the shape-based method to handle the estimation for each slice, and correlate them. The overall 3D object structure is defined by “stacking” the primitive images together,

creating a parametrized approximation to a 3D object. Specifically, in 3D Cartesian coordinates (denoted by $x - y - z$), if z is assumed to correspond to the “vertical”, then each primitive resides in an $x - z$ plane. This takes advantage of the tubular nature of vessels commonly found in parallel plate breast imaging (where the breast is compressed) and the fact that major vessels in breast tissue generally travel perpendicular to the chest wall [62]. The reconstruction algorithm is capable of “deactivating” any unnecessary basis functions and thereby discovering the required number of active and passive primitives to effectively reconstruct the object’s shape structure. As such, the model can effectively image multiple spatially separate anomalies against a background of potentially unknown structure. Correlating adjacent slices we implement a regularization approach to augment the optimization method with a cost term associated with the assumed linear relationship between adjacent primitives. The source detector setup used for the purpose of this thesis, where source and detector is scanned in tandem, relates our method to an optical mammography device currently being designed by Prof. Sergio Fantini’s group at the Tufts University Biomedical engineering department. Our method of recovering shape, volume and absorption estimates can utilize depth and oxygen saturation information acquired by Prof. Fantini’s system as well as advancing the modality towards a standalone device. This consideration is discussed further in Chapter 7.

2.6 Hyperspectral information

Research for DOT has shown that including multiple wavelengths in measurements can increase the accuracy of the measurement. Multispectral measurements made it possible for Boverman et al. [15, 99] to obtain hemoglobin images of the concentration and the hemoglobin oxygen saturation. Corlu et al. [30] showed that using multiple wavelengths are the key for obtaining physiologically relevant tissue parameters with CW light. Indeed, a factor in detecting breast cancer is the discrimination of actual cancer and benign lesions or normal tissue inhomogeneities in the breast. Multi-wavelength information has been shown to be useful to make this distinction [42], which is due to the fact that determining the level of blood oxygenation in the breast can show the local supply and demand of oxygen. Since cancer tumors were suspected to have low-oxygen levels this information can be clinically useful in making the difference between tumors and benign artifacts [42].

Multispectral data has also potential to reduce the non-uniqueness of the solution to the DOT problem. This concept is not new and has been researched extensively for the past 20 years [5]. In the case of CW measurements, it has been shown that different sets of absorption and scattering parameters can yield identical data. Also, inversions can suffer from cross-talk between absorption and scattering [5]. Cross-talk happens when a reconstructed image of a chromophore shows traces of concentrations from other chromophores. These "ghost" images greatly reduce accuracy of the overall reconstruction. Corlu et al. [30] showed how this nonuniqueness problem could

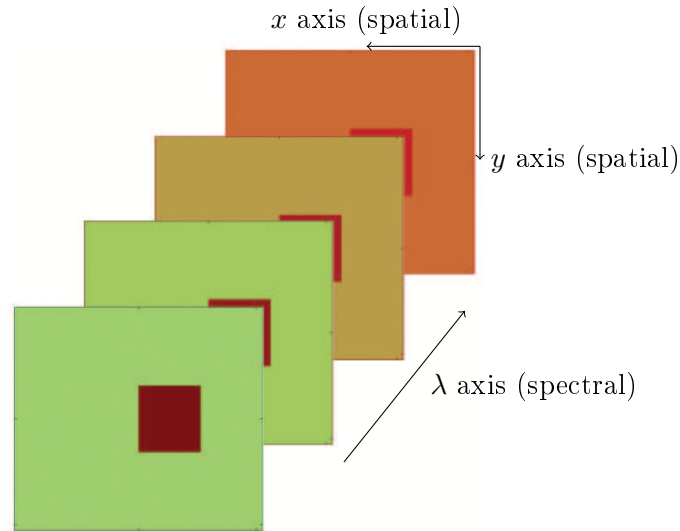


Figure 2.3: *Example of hyperspectral cube considered for multi wavelength imaging. Each pixel in each image on the spectral axis corresponds to an absorption value in the near-infrared spectrum.*

be solved by using multispectral data, provided that it is used with the correct wavelengths.

Implementing multispectral information for DOT requires an informed choice of wavelengths to recover specific chromophore concentrations. Increasing the amount of data used eliminates this choice and opens the option of generalizing the model to simultaneously recovering multiple chromophores. Considering this it is imperative to discuss how many wavelengths should be included in the measurement, and how to optimally choose the added wavelengths. This is where hyperspectral measurements come into play, which involves using a great number of wavelengths for the measurement. However there is no set number of wavelengths that defines hyperspectral imaging from multispectral imaging. Comparing hyperspectral vs. multispectral

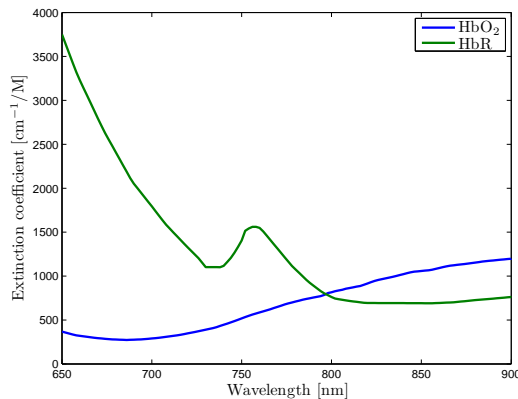


Figure 2.4: *Molar extinction coefficients for oxy-hemoglobin (HbO_2) deoxy-hemoglobin (HbR) shown as a function of wavelength.*

imaging, the wavelengths available for a reconstruction is on the scale of ~ 100 in the hyperspectral case and that for the multispectral case is less than ~ 10 spectral bins [22].

Hyperspectral imaging has been used extensively in the fields of remote sensing and geology of natural and man-made materials that are indistinguishable using standard color imagery [69, 96]. The fundamental basis for space-based remote sensing is that information is potentially available from the electromagnetic energy field arising from the earth's surface and, in particular, from the spatial, spectral and temporal variations in that field. This information is often represented by a 3D cube, where the two face axes represent spatial locations, and the depth axis of the cube represents spectral variations. This is referred to as a hyperspectral cube, shown in Fig. 2.6. Researchers have moved on to look at how the spectral variations might be used in cases where imaging modalities work with data with low spatial resolution. In the

case of DOT, these spectral variations are represented by the extinction coefficients of the different chromophores being estimated, where the extinction coefficient spectrum for oxyhemoglobin and deoxyhemoglobin are shown in Fig. 2.6.

When reconstructing images for concentrations of chromophores in DOT there are generally two ways of using spectral information. In this project these two methods will be referred to as the direct method and the indirect method. The indirect method generally requires three steps to obtain the concentration images. First, measurements are taken at two or more wavelengths. Second, images of the absorption and reduced scattering coefficients at the different wavelengths are reconstructed separately. Last, the concentration of the separate chromophores are derived from the optical properties. On the other hand the direct method skips the step of constructing the spectral absorption images and directly reconstructs the chromophore images from measured data [73]. For this thesis we implement the direct method for recovering chromophore images.

In this thesis, we will explore the value of hyperspectral data for addressing the many issues associated with ill-posedness encountered with DOT. It will be examined how hyperspectral data can increase resolution and reduce cross-talk. In other words, the ability to localize small perturbations from individual species and ability to separate multiple species.

Chapter 3

Forward Models

In this chapter we consider the forward models used to model photon migration for the methods in this thesis. We consider the physics of mass transport as it is applied to photon migration.

3.1 Diffusion approximation

For the purpose of this thesis we consider the diffusion approximation of the radiative transport equation (RTE), an integro-differential equation, considered the most general model for photon migration. Due to its complexity and high dimensionality its solutions are generally solved using Monte Carlo or numerical methods like finite element, finite difference or spherical harmonics method [77]. The diffusion approximation assumes that the specific intensity develops a nearly isotropic angular

distribution due to the multiple scattering effects. Additionally the diffusion approximation replaces the use of the RTE scattering phase function with a single parameter, the reduced scattering coefficient, defined by

$$\mu'_s = \mu_s(1 - g) \quad (3.1)$$

where g is defined as the cosine of the scattering angle and the scattering coefficient μ_s is equal to the reciprocal of the transport scattering length. This length is defined by the distance when a collimated beam becomes effectively diffuse, which is about 1 mm for near-infrared light in biological tissue. It should be noted that the RTE can be derived by first principles by applying Maxwell's equations to the problem of multiple electromagnetic scattering in discrete random media [78].

In the time dependent case, the diffusion approximation assumes that the photon current is constant in time, where in general terms the assumption is that the absorption coefficient, μ_a , is dominated by scattering, stated by $\mu_a \ll \mu'_s$, such that the ratio $\mu'_s/(\mu_s + \mu_a)$ is close to unity. From this, the diffusive assumption can be justified when scattering effects are predominant over absorption. Lastly the source-detector separation must be greater than $1/\mu'_s$ which is in the range of 1 mm. Considering our application of breast imaging in transmission geometry, this constraint is upheld.

A model of light propagation in a highly scattering medium is necessary both to compute the simulated fluence at the detectors and to map the fluence back to the chromophore concentrations. Utilizing the diffusion approximation to the RTE we obtain a useful and commonly employed model for the photon fluence in a highly

scattering medium, which is often referred to as the Helmholtz frequency domain diffusion equation

$$\nabla \cdot D^0(\mathbf{r}, \lambda) \nabla \Phi(\mathbf{r}, \lambda) + (j\omega - v\mu_a^0(\mathbf{r}, \lambda)) \Phi(\mathbf{r}, \lambda) = -vS(\mathbf{r}, \lambda) \quad (3.2)$$

where $\Phi(\mathbf{r}, \lambda)$ is the photon fluence rate at position \mathbf{r} due to light of wavelength λ injected into the medium, v is the electromagnetic propagation velocity in the medium, $\mu_a^0(\mathbf{r}, \lambda)$ is the spatially varying absorption coefficient, and $S(\mathbf{r}, \lambda)$ is the photon source with units of optical energy per unit time per unit volume. For the work in this thesis the source is considered to be delta sources in space and can be written as $S(\mathbf{r}, \lambda) = S_0(\lambda)\delta(\mathbf{r} - \mathbf{r}_s)$ with $S_0(\lambda)$ the source power at wavelength λ . We note that (3.2) includes the term $j\omega$ where ω is the modulation frequency of the light intensity [108]. Throughout this thesis we consider exclusively problems for which $\omega = 0$, representing CW measurements. For spatially varying scattering we assume that the diffusion coefficient $D^0(\mathbf{r}, \lambda)$ follows Mie scattering theory where a scattering prefactor Ψ depends on the size and density of scatterers while a scattering exponent b depends on the size of the scatterers. Using this, we write the diffusion coefficient as

$$D^0(\mathbf{r}, \lambda) = \frac{v}{3\Psi} \left(\frac{\lambda}{\lambda_0} \right)^b = v\Psi' d(\lambda). \quad (3.3)$$

The arbitrarily chosen reference wavelength λ_0 is introduced to achieve a form of the Mie model where Ψ has the units of mm^{-1} and Ψ' has units of mm .

3.2 Discrete model and integral equation

Now as discussed in Chapter 2 we decompose the diffusion and absorption coefficient as

$$\begin{aligned} D^0(\mathbf{r}, \lambda) &= D(\lambda) + \Delta D(\mathbf{r}, \lambda) \\ \mu_a^0(\mathbf{r}, \lambda) &= \mu_a(\lambda) + \Delta\mu_a(\mathbf{r}, \lambda). \end{aligned} \tag{3.4}$$

By this we can show that the perturbation in $\Delta\mu_a$ and ΔD are related by an integral transformation to the data which can be defined as

$$\Phi(\mathbf{r}, \lambda) = \Phi^i(\mathbf{r}, \lambda) + \Phi^s(\mathbf{r}, \lambda) \tag{3.5}$$

where Φ^i and Φ^s are the incident and scattered field, respectively, as discussed in Chapter 2. Using this we can rewrite (3.2) as

$$\nabla \cdot (D(\lambda) + \Delta D(\mathbf{r}, \lambda)) \nabla \Phi(\mathbf{r}, \lambda) + (j\omega - v(\mu_a(\lambda) + \Delta\mu_a(\mathbf{r}, \lambda))) \Phi(\mathbf{r}, \lambda) = -vS(\mathbf{r}, \lambda). \tag{3.6}$$

The solution to (3.6) obeys the integral equation

$$\Phi(\mathbf{r}, \lambda) = \Phi^i(\mathbf{r}, \lambda) + \int_V G(\mathbf{r}, \mathbf{r}', \lambda) [\nabla \cdot \Delta D(\mathbf{r}', \lambda) \nabla - v \Delta\mu_a] \Phi(\mathbf{r}', \lambda) d\mathbf{r}' \tag{3.7}$$

where Φ^i is the incident field and $G(\mathbf{r}, \mathbf{r}', \lambda)$ is the Green's function that satisfies the diffusion equation defined as

$$\left[\nabla^2 + \frac{v\mu_a(\mathbf{r}, \lambda) - j\omega}{D(\lambda)} \right] G(\mathbf{r}, \mathbf{r}', \lambda) = \delta(\mathbf{r} - \mathbf{r}'). \tag{3.8}$$

In general the Green's function G must satisfy boundary conditions on the boundaries where sources and detectors are located as well as (3.8). The Green's functions differ

in terms of what geometry is considered, where throughout this thesis we consider transmission geometry. In this kind of setup, demonstrated in Fig. 2.1, where a source and detector are on opposite sides of the medium to be imaged, light is injected into the medium from the source, which migrates through it and absorbs or scatters and resulting signal is picked up by the detector.

3.3 Green's Functions

Analytical solutions exist that directly compute the value of the Green's functions relating to each geometry. Working with Green's functions require a choice of geometry that is best suitable for the experimental setup at hand [77] where they are computed when the source is considered to be a spatial and temporal delta function. Green's functions are commonly employed to compute the forward problem in image reconstruction, especially when the medium can be approximated as a slab or an infinite half-space, which is often considered for reflectance measurements. As noted by Gibson [49] some researches have extended this approach by implementing the Kirchhoff approximation, which models the Green's function between two points in a medium of arbitrary geometry by summing together Green's functions in infinite space and Green's functions computed for waves reflected multiple times off the boundary [90]. Various geometries can be considered for this situation, and here we consider three cases, the infinite medium, slab medium with boundary conditions on source and detector planes, and a box with boundary conditions on all sides.

For the case of an infinite medium, free-space Green's functions are used to compute $G(\mathbf{r}, \mathbf{r}', \lambda)$ in (3.20) and 3.17 [48]. Physically this amounts to embedding the source and detector in the medium and no boundary conditions are considered for the photon fluence, although fields are required to obey asymptotic decay conditions. As discussed by Fabrizio et. al [77] the geometry of the infinite medium is mainly useful for understanding the intrinsic characteristics of photon migration, since this geometry allows for studying only the effects due to optical properties, not boundaries. Obviously this setup is not realistic for a non-invasive imaging modality like DOT, however, considering infinite boundaries allows for relatively simple computations and is a good starting point to test algorithms. Expanding each method to a more complicated geometry, incorporating boundaries is relatively straightforward. For the infinite medium, the free-space Green's function is computed by

$$G(\mathbf{r}, \mathbf{r}', \lambda) = \frac{-1}{4\pi D(\lambda) |\mathbf{r} - \mathbf{r}'|} e^{jk_0(\lambda)|\mathbf{r} - \mathbf{r}'|} \quad (3.9)$$

As discussed above, throughout this thesis a transmission geometry is considered, shown in Fig. 2.1, as it is most commonly used for the female breast imaging scenario. A natural progression from infinite boundary is to consider infinite slab geometry, where boundary conditions on the plane of the source and detector are taken into account. In other settings we consider a infinite slab geometry where boundaries are applied to the planes where sources and detectors reside. For the case of constant scattering and where the estimation of absorption values is the goal the

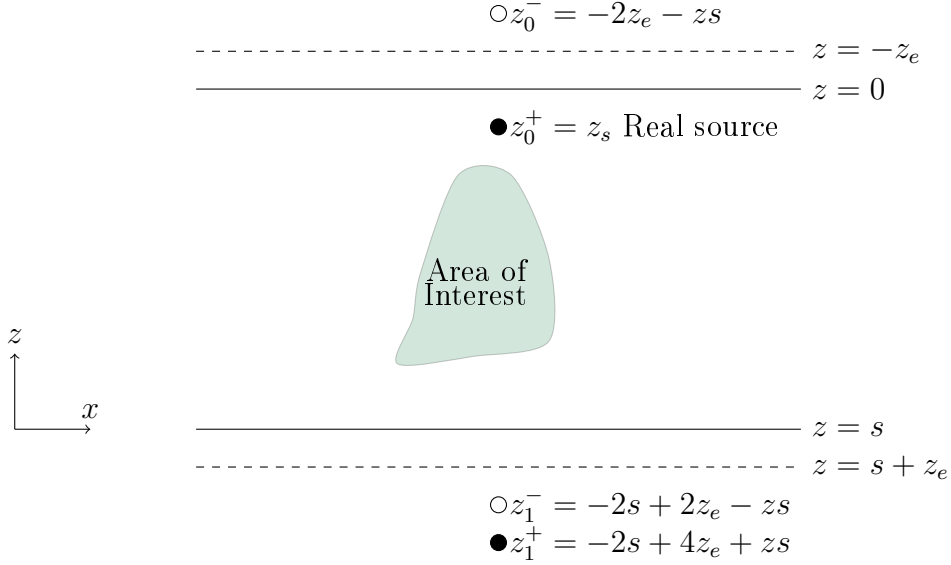


Figure 3.1: *Setup of the slab geometry with example mirror sources used for calculating the slab geometry Green's function. Figure is not to scale.*

Green's function is [77]

$$G(\mathbf{r}, \lambda) = \frac{-1}{4\pi D(\lambda)} \sum_{m=-\infty}^{m=+\infty} \left\{ \frac{\exp\left[-\mu_{eff}(\lambda)\sqrt{\rho^2 + (z - z_m^+)^2}\right]}{\sqrt{\rho^2 + (z - z_m^+)^2}} - \frac{\exp\left[-\mu_{eff}(\lambda)\sqrt{\rho^2 + (z - z_m^-)^2}\right]}{\sqrt{\rho^2 + (z - z_m^-)^2}} \right\} \quad (3.10)$$

and μ_{eff} is

$$\mu_{eff}(\mathbf{r}, \lambda) = \sqrt{\mu_a(\mathbf{r}, \lambda)/D(\lambda)} = \sqrt{3\mu_a(\mathbf{r}, \lambda)\mu'_s(\lambda)} \quad (3.11)$$

where $\rho = \sqrt{x^2 + y^2}$. This solution is obtained by the method of images, sometimes called “mirror images.” The method makes use of boundary conditions that assume the fluence equal to zero on the physical boundary of the diffusive medium or on an extrapolated surface at a certain distance from the physical boundary [58]. The method of images allows for a solution of the photon fluence in the slab geometry as

a superposition of solutions for the infinite medium. In this formulation, z_m^+ and z_m^- represent real positive and negative source locations, respectively. As shown in Fig. 3.1 these sources are placed along the z -axis at

$$\begin{aligned} z_m^+ &= 2m(s + 2z_e) + z_s \\ z_m^- &= 2m(s + 2z_e) - 2z_e - z_s \end{aligned} \tag{3.12}$$

where m are the summation terms in (3.10), s denotes the thickness of the slab, and z_e denotes the extrapolated boundary. This simplifies computations somewhat, when the solution for the infinite medium has already been established, and provides a useful model when experiments are performed for a phantom with boundary conditions.

3.4 Born Approximation

To formulate the integral equation which is used for our inversion methods, we employ the Born approximation, which as discussed in Chapter 2 consists of taking the incident field Φ^i , shown in (3.5), in place of the total field Φ in the scatterer.

Now considering the perturbation theory for ΔD and $\Delta\mu_a$ and the assumption that $\Phi^i(r, \lambda) \gg \Phi^s(r, \lambda)$, which gives us a approximated solution of (3.2) as

$$\begin{aligned} \Phi^s(\mathbf{r}, \lambda) &\approx - \left(\int \Delta\mu(\mathbf{r}', \lambda) G(\mathbf{r}_d, \mathbf{r}', \lambda) \Phi^i(\mathbf{r}', \mathbf{r}_s, \lambda) d\mathbf{r}' \right. \\ &\quad \left. + \int \Delta D(\mathbf{r}', \lambda) \nabla G(\mathbf{r}_d, \mathbf{r}', \lambda) \cdot \nabla \Phi^i(\mathbf{r}', \mathbf{r}_s, \lambda) d\mathbf{r}' \right) \end{aligned} \tag{3.13}$$

where \mathbf{r}_d is the location of the detector and $\Phi^i(\mathbf{r}, \mathbf{r}_s, \lambda)$ is used here to denote the incident field at position \mathbf{r} and wavelength λ due to a delta-source located at \mathbf{r}_s .

Examining (3.13) provides a linear relationship between the scattered fluence and the absorption perturbation.

This equation can be discretized by considering only voxel points in the medium. Then the value \mathbf{r}_i is defined as the position vector, denoting location in the medium with \mathbf{r}_i denoting the location of the i^{th} such point within \mathcal{F} . More formally, we expand $\Delta\mu_a(\mathbf{r}', \lambda)$ and $\Delta D(\mathbf{r}', \lambda)$ using Dirac delta functions

$$\begin{aligned}\Delta\mu_a(\mathbf{r}', \lambda) &= a \sum_{\mathbf{r}_i}^{N_v} \Delta\mu_a(\mathbf{r}_i, \lambda) \delta(\mathbf{r}' - \mathbf{r}_i) \\ \Delta D(\mathbf{r}', \lambda) &= a \sum_{\mathbf{r}_i}^{N_v} \Delta D(\mathbf{r}_i, \lambda) \delta(\mathbf{r}' - \mathbf{r}_i)\end{aligned}\tag{3.14}$$

where a represents the area of a pixel and N_v number of field points, or pixels considered. Inserting (3.14) into equation (3.13) allows for discretization, by

$$\begin{aligned}\Phi^s(\mathbf{r}, \lambda) &\approx - \left(\int a \sum_{\mathbf{r}_i}^{N_v} \Delta\mu_a(\mathbf{r}_i, \lambda) \delta(\mathbf{r}' - \mathbf{r}_i) G(\mathbf{r}_d, \mathbf{r}', \lambda) \Phi^i(\mathbf{r}', \mathbf{r}_s, \lambda) d\mathbf{r}' \right. \\ &\quad \left. + \int a \sum_{\mathbf{r}_i}^{N_v} \Delta D(\mathbf{r}_i, \lambda) \delta(\mathbf{r}' - \mathbf{r}_i) \nabla G(\mathbf{r}_d, \mathbf{r}', \lambda) \cdot \nabla \Phi^i(\mathbf{r}', \mathbf{r}_s, \lambda) d\mathbf{r}' \right) \\ &\approx - \left(a \sum_{\mathbf{r}_i}^{N_v} \Delta\mu_a(\mathbf{r}_i, \lambda) \int \delta(\mathbf{r}' - \mathbf{r}_i) G(\mathbf{r}_d, \mathbf{r}', \lambda) \Phi^i(\mathbf{r}', \mathbf{r}_s, \lambda) d\mathbf{r}' \right. \\ &\quad \left. + a \sum_{\mathbf{r}_i}^{N_v} \Delta D(\mathbf{r}_i, \lambda) \int \delta(\mathbf{r}' - \mathbf{r}_i) \nabla G(\mathbf{r}_d, \mathbf{r}', \lambda) \cdot \nabla \Phi^i(\mathbf{r}', \mathbf{r}_s, \lambda) d\mathbf{r}' \right) \\ &\approx - \left(a \sum_{\mathbf{r}_i}^{N_v} \Delta\mu_a(\mathbf{r}_i, \lambda) G(\mathbf{r}_d, \mathbf{r}_i, \lambda) \Phi^i(\mathbf{r}_i, \mathbf{r}_s, \lambda) \right. \\ &\quad \left. + a \sum_{\mathbf{r}_i}^{N_v} \Delta D(\mathbf{r}_i, \lambda) \nabla G(\mathbf{r}_d, \mathbf{r}_i, \lambda) \cdot \nabla \Phi^i(\mathbf{r}_i, \mathbf{r}_s, \lambda) \right)\end{aligned}\tag{3.15}$$

Considering (3.15) a linear relationship between absorption, diffusion coefficient and measurement data has been established.

As discussed in Chapter 1 some reconstruction results and methods strictly consider reconstructing absorption values or chromophore concentrations. In this scenario the diffusion coefficient in (3.3) is assumed to be spatially invariant as

$$D(\lambda) = \frac{v}{3\mu'_s}. \quad (3.16)$$

This changes (3.2) significantly and simplifies computations somewhat. We utilize the same approach as before with the Born approximation, resulting in the linearized discretized model is computed by

$$\Phi^s(\mathbf{r}_d, \lambda) = -a \sum_{j=1}^{N_v} G(\mathbf{r}_d, \mathbf{r}_j, \lambda) \Phi^i(\mathbf{r}_j, \mathbf{r}_s, \lambda) \Delta\mu_a(\mathbf{r}_j, \lambda). \quad (3.17)$$

Now as mentioned in Chapter 1, DOT is often used to image the concentration of oxyhemoglobin and deoxy-hemoglobin along with other chromophores in tissue. The technique exploits the fact that oxyhemoglobin, HbO_2 , and deoxy-hemoglobin, HbR , are dominant absorbers in the infrared region [72]. It can be assumed that the absorption coefficient is dominated by the hemoglobin, then for these two chromophores the absorption coefficient would be written as

$$\Delta\mu_a(\mathbf{r}, \lambda) = \varepsilon_{\text{HbO}_2}(\lambda) \Delta c_{\text{HbO}_2}(\mathbf{r}) + \varepsilon_{\text{HbR}}(\lambda) \Delta c_{\text{HbR}}(\mathbf{r}). \quad (3.18)$$

where ε_X are the extinction coefficient of chromophore X and Δc_X represents the concentration of the X^{th} chromophore. The dependence of \mathbf{r} in (3.18) comes from the concentration of each chromophore. Even though the DOT method benefits from the reactions of hemoglobin to infrared light, it can be extended to image other

chromophores, like water or lipids for example. For the case of N_c chromophores (3.18) would become,

$$\Delta\mu_a(\mathbf{r}, \lambda) = \sum_{k=1}^{N_c} \varepsilon_k(\lambda) \Delta c_k(\mathbf{r}) \quad (3.19)$$

Using (3.19), we write (3.15) as

$$\begin{aligned} \Phi^s(\lambda) = & -a \sum_{k,j=1}^{N_c, N_V} \left(G(\mathbf{r}_d, \mathbf{r}_j, \lambda) \Phi^i(\mathbf{r}_j, \mathbf{r}_s, \lambda) \varepsilon_i(\lambda) \Delta c_{k,j} \right. \\ & \left. + \nabla G(\mathbf{r}_d, \mathbf{r}_j, \lambda) \cdot \nabla \Phi^i(\mathbf{r}_j, \mathbf{r}_s, \lambda) \Delta D_j(\mathbf{r}, \lambda) \right). \end{aligned} \quad (3.20)$$

Similarly, (3.19) can be used with (3.17) to relate chromophore concentrations to measurement data, with uniform spatial scattering.

The computational tractability of the inversion scheme we implement in this thesis arises from the linear algebraic structure associated with (3.20). We start by defining $\mathbf{c}_k \in \mathbb{R}^{N_v}$ as the vector obtained by lexicographically ordering the unknown concentrations associated with the k^{th} chromophore and $\Phi^s(\mathbf{r}_j, \mathbf{r}_s, \lambda)$ to be the vector of observed scattered fluence rate associated with all source-detector pairs collecting data at wavelength λ . Now, with N_λ the number of wavelengths used in a given experiment, (3.20) is written in matrix-vector notation as

$$\begin{bmatrix} \Phi^s(\lambda_1) \\ \Phi^s(\lambda_2) \\ \vdots \\ \Phi^s(\lambda_{N_\lambda}) \end{bmatrix} = \begin{bmatrix} \varepsilon_1(\lambda_1) \mathbf{K}_1^a & \varepsilon_2(\lambda_1) \mathbf{K}_1^a & \dots & \varepsilon_{N_c}(\lambda_1) \mathbf{K}_1^a & \mathbf{K}_1^d \\ \varepsilon_1(\lambda_2) \mathbf{K}_2^a & \varepsilon_2(\lambda_2) \mathbf{K}_2^a & \dots & \varepsilon_{N_c}(\lambda_2) \mathbf{K}_2^a & \mathbf{K}_2^d \\ \vdots & \vdots & \vdots & \vdots & \vdots \\ \varepsilon_1(\lambda_{N_\lambda}) \mathbf{K}_{N_\lambda}^a & \varepsilon_2(\lambda_{N_\lambda}) \mathbf{K}_{N_\lambda}^a & \dots & \varepsilon_{N_c}(\lambda_{N_\lambda}) \mathbf{K}_{N_\lambda}^a & \mathbf{K}_{N_\lambda}^d \end{bmatrix} \begin{bmatrix} \Delta \mathbf{c}_1 \\ \Delta \mathbf{c}_2 \\ \vdots \\ \Delta \mathbf{c}_{N_c} \\ \Delta \Psi' \end{bmatrix} \quad (3.21)$$

where \mathbf{K}_l^a represents the first term in the sum of (3.20) relating to chromophore concentrations and \mathbf{K}_l^d is the second term relating to the scattering amplitude. For the case of a constant diffusion coefficient as in (3.17) the formulation in (3.21) omits the \mathbf{K}_l^d terms and $\Delta\Psi'$, which represents the perturbation in diffusion amplitude.

It should be noted in (3.21) that the matrix has elements which are also the matrices \mathbf{K}_l^a and \mathbf{K}_l^d . The $(m, j)^{th}$ element of them both represents the m^{th} source-detector pair and as before j represents the j^{th} voxel. Assuming that for a given experiment N_{sd} source detector pairs operate at all N_λ wavelengths, then each \mathbf{K}_l has N_{sd} rows and N_v columns so that the whole matrix \mathbf{K} is of size $N_{sd}N_\lambda \times N_vN_c$. If, for example, in an experimental setup where $N_{sd} = 57$, $N_c = 2$ chromophores, and image reconstruction is done for 1800 pixels, $N_v = 1800$, and $N_\lambda = 126$ results in a \mathbf{K} matrix of size 7182×3600 . Combining the matrix elements in (3.21) we write it in a more simple way as

$$\Phi^s = \mathbf{K}\Delta\mathbf{c}. \quad (3.22)$$

Chapter 4

Experimental methods

4.1 Measurements

Measurements are performed in collaboration with Prof. Sergio Fantin's group in the Biomedical Engineering Department at Tufts University. Two groups of experiments were conducted. The first group involved a liquid phantom made to have realistic optical properties comparable to the female breast. The purpose of these experiments was to test the improvements of including hyperspectral information to solve the inverse problem discussed in Chapter 2. The second group of experiments involved a solid phantom made of cured silicon. These experiments were performed to provide experimental validation of our method to recover 3D tubular structures, detailed in Chapter 7.

4.2 Milk and Water phantom

Experiments were performed to simulate a problem in an unbounded domain. To that end, a clear fish tank was filled with a milk and water solution in which sources and detectors were submerged in the center away from edges in order to simulated infinite boundaries. An example image of this experimental setup is shown in Fig. 4.4.

4.2.1 Liquid phantom

The background medium consists of water and milk in the ratio of 2:1, respectively. Milk, with 2% fat, is used due to the similarities of the optical properties to human breast tissue. Black India ink and blue food dye were added to mimic tissue chromophores. The ink and dye are mixed into the background of milk and water to achieve $\mu_a = 0.029 \text{ cm}^{-1}$, at 600 nm, which is in the range of optical absorption of the female breast [36, 98]. The absorption spectra for the ink and dye inclusions, shown in Fig. 4.1(b), have the most significant effect in the 450-700 nm range. These chromophores are chosen because the spectral shapes of their absorption are similar to those of HbO₂ and HbR and have been widely used in literature [31, 75].

In order to obtain multi- and hyperspectral reconstruction values for $\mu_a(\lambda)$ and $D(\lambda)$ the background has to be known and in the experimental measurements we assume uniform scattering. Therefore we have the unperturbed representation of the reduced scattering coefficient, μ'_s , which is given by

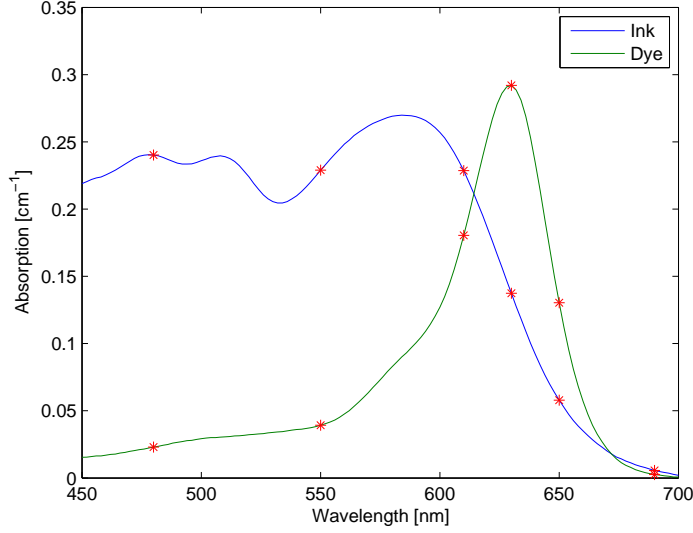


Figure 4.1: *Absorption spectra of the ink and dye solutions chromophores used in experimental measurements. Specifically chosen wavelengths are marked with an asterisk.*

$$\mu'_s = \Psi \left(\frac{\lambda}{\lambda_0} \right)^{-b}. \quad (4.1)$$

This relates to the diffusion coefficient, $D(\lambda)$, as it is defined in (3.16). Phase, amplitude and average intensity data are obtained at two wavelengths using a frequency-domain tissue spectrometer to estimate the Ψ and b parameters in (4.1). This allows us to extrapolate values for μ'_s at any wavelength [51].

The measurement to obtain values for the μ'_s calculation and to verify that μ_a is close to the values used from literature is performed at two wavelengths, 690 nm and 830 nm. The measurement give AC, DC and phase data for a signal travelling in the medium which can be used to calculate μ'_s and μ_a for the medium. In greater detail,

this information is obtained by moving a detector away from a light source inside of the medium. The change in AC amplitude, DC amplitude and phase is plotted as a function of the position. Then S_φ , S_α and S_δ are defined as the slopes when the phase, $\ln(DC \cdot r)$ and $\ln(AC \cdot r)$ are plotted respectively as a function of position of r the source-detector separation, respectively. As shown by Fantini et al. [39] the absorption coefficient and scattering coefficient can then be calculated from S_α by using

$$\mu_a = \frac{\omega}{2v} \left(\frac{S_\varphi}{S_\alpha} - \frac{S_\alpha}{S_\varphi} \right) \quad \mu'_s = \frac{S_\alpha^2 - S_\varphi^2}{3\mu_a}.$$

where ω is the modulation frequency set at 110 MHz, v is the speed of light divided by the index of refraction set as $n = 1.4$ [40]. To verify these values, a separate computation are made with, S_δ , by using these relations

$$\mu_a = -\frac{\omega}{2v} \left(\frac{S_\varphi^2}{S_\delta^2} + 1 \right)^{-\frac{1}{2}} \quad \mu'_s = \frac{S_\delta^2}{3\mu_a} - \mu_a$$

Using this method the values in (4.1) were computed to be $\Psi = 6.5 \text{ cm}^{-1}$ and $b = 0.4$.

Since μ_a does not follow a defined law like μ'_s , another approach has to be used by estimating values by estimating extinction coefficient data for ink, dye, milk and water. These extinction coefficient are measured in a standard spectrophotometer.

In our experiments, two phantom inclusions, named set 1 and set 2, are created for different absorption contrasts relative to the background in the range of 3:1 to 1:1. The inclusion in set 1 contains 10% ink and 90% dye and the inclusion for set 2 contains 70% dye and 30% ink. This contrast range is comparable to traditional tumour contrasts reported in literature, which have been close to 3:1 and lower [84].

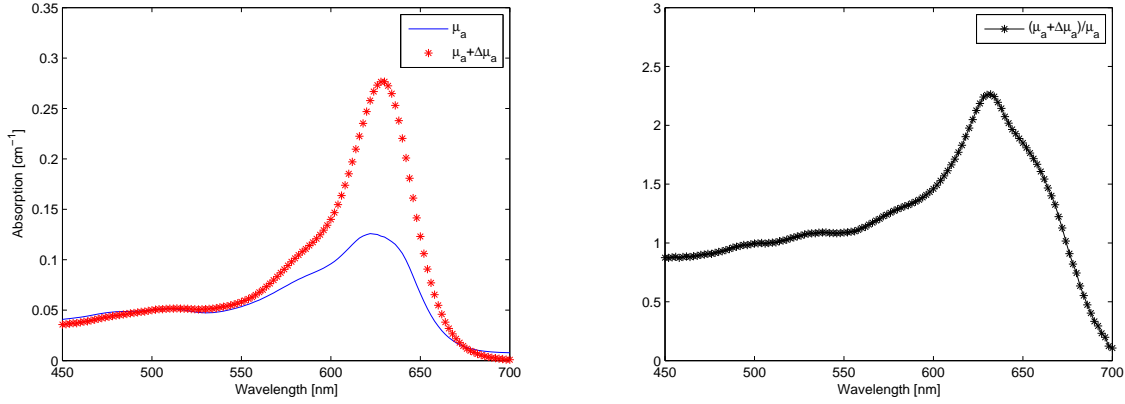


Figure 4.2: (a) Absorption spectra for the background, μ_a , and the inclusion, $\mu_a + \Delta\mu_a$, in experimental set 1, containing 10% ink and 90% dye. (b) Contrast between the background and the inclusion for experimental set 1.

The reconstructions in Chapter 5 are done for 176 wavelengths equally spaced over the whole spectrum and six specifically chosen wavelengths as $\lambda = [480, 550, 610, 630, 650, 690]$ nm. The wavelengths are chosen around the isosbestic point, at 610 nm in Fig. 4.1, where the contrast between the chromophores is the highest and where each chromophore has highest absorption. The absorption spectra and the contrast over the spectrum for set 1 and set 2 are shown in Fig. 4.2 and Fig. 4.3, respectively.

4.2.2 Measurement setup

In experimental sets 1 and 2 one cylindrical inclusion containing ink and dye solutions are placed in the background medium. These inclusions are 25 cm long transparent tubes so that optical properties are assumed constant along the z-axis. The light

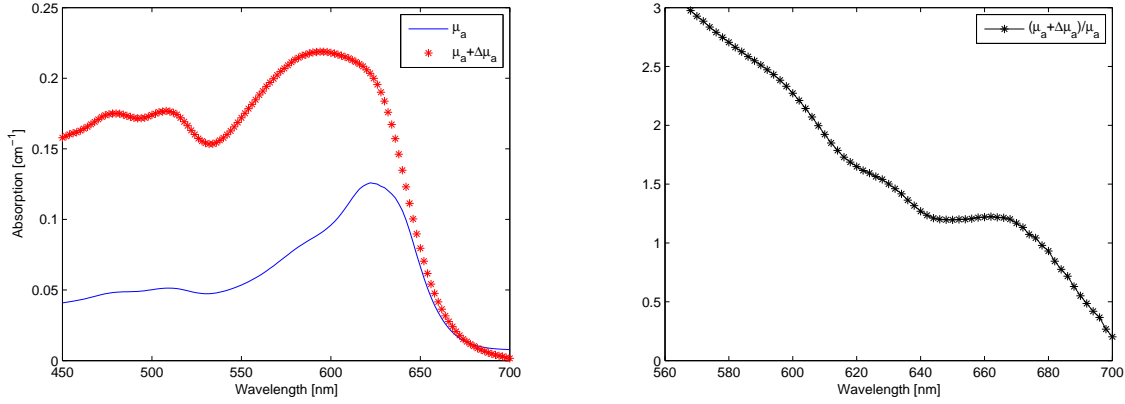


Figure 4.3: (a) Absorption spectra for the background, μ_a , and the inclusion, $\mu_a + \Delta\mu_a$, in experimental set 2, containing 70% ink and 30% dye. (b) Contrast between the background and the inclusion for experimental set 2.

source is an arc lamp (Model No.6258, Oriel Instrument, Stratford, CT) whose emission is first spectrally filtered (400 -1000 nm) to reject ultraviolet and infrared light, and then focused onto a 3-mm-diameter illumination optical glass fiber bundle, which delivers light with an average illumination power of 280 mW, which translates into a power density of 3.96 W/cm². A 5 mm diameter collection optical glass fiber bundle is located at three positions on the x axis, at $x_d = \{-1, 0, 1\}$ where the source location is defined as $x_s = 0$. As discussed above, we consider transmission geometry, so sources are on the opposite side of the inclusions at a y -axis separation of 5 cm and linearly scanned.

Experiments are made with the light source placed in succession at 8 positions with 1 cm increments for a total of 24 source-detector pairs. The collection optical fiber delivers light to a spectrograph (Model No. SP-150, Acton Research Corp., Acton,

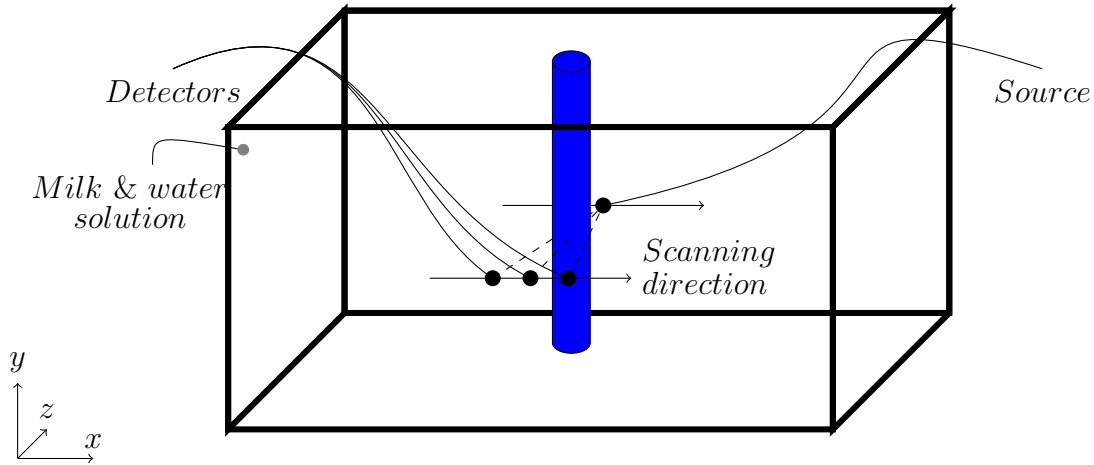


Figure 4.4: *The setup of sources and detectors for infinite geometry using liquid milk and water phantom.*

MA), which disperses the light onto the detector array of a charge coupled device (CCD) camera (Model No. DU420A-BR-DD, Andor Technology, South Windsor, CT). Two exposure times are used for the CCD camera to ensure that approximately the same number of photons are collected for reconstructions using 6 wavelengths and for 176 wavelengths. Longer exposure time of 10 s is used for the 6 wavelength case and 500 ms for the 176 wavelength case. In Chapter 5, we will demonstrate the improvement of including hyperspectral information, therefore, we setup the stage by presenting an ideal case where the signal to noise ratio is large, thereby providing a best-case scenario for the few-wavelength reconstruction against which we compare our approach as well as using realistic absorption contrasts for the inclusions. The spectrograph features a grating blazed at 700 nm with 350 g/mm, resulting in a dispersion of 20 nm/mm at the exit port. The size of the CCD camera pixels of 26

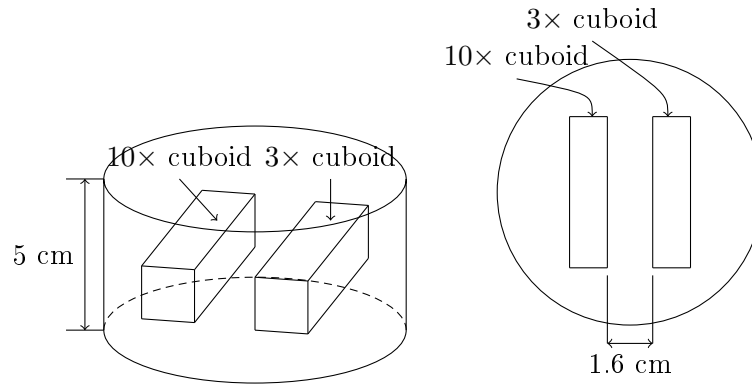


Figure 4.5: *Silicon phantom used for experimental measurements. Homogeneous cylindrical slab, with two absorbing inclusions.*

$\mu\text{m} \times 26 \mu\text{m}$ results in a spectral sampling rate of two data points per nanometer, even though the spectral resolution is not as high because of the size of the entrance slit (2 mm) used to accommodate the large collection optical fiber bundle. From the data we only retain the wavelength band 650-900 nm where the signal-to-noise ratio is adequate.

In our experiments the incident field is a data set taken before the perturbation is put into the medium. The scattered field is then computed as a dataset that has the original unperturbed dataset subtracted from it.

4.3 Silicon phantom

This experimental set was taken to validate our method to recover 3D tubular structures by reconstructing multiple 2D slices. To that end a silicon phantom was constructed by Elizabeth Rosenberg, undergraduate student in the Biomedical Engineering Department, and scans were acquired by Pamela G. Anderson, a doctoral student in Prof. Fantini's lab at the Tufts Medical Center.

4.3.1 Construction of Cylinder

The structure of the silicon phantom is shown in Fig. 4.5. It is made of two cylindrical slabs, both made of identical homogeneous solutions, where one of them contains two higher absorbing inclusions. The two slabs are cured independently, where the one containing inclusions is fitted with cuvettes to create gaps where they are placed. The homogeneous background slabs were made with 360 mL of PDMS (Silicone Inc, P-4). The procedure begins by mixing 36 mL of curing agent (Silicone Inc, P-4) with 0.288 g TiO_2 powder for 30 minutes, and the PDMS is mixed with 0.1008 g of India ink and cured for 15 minutes. The PDMS/INK mixture is then placed into a vacuum chamber to remove air bubbles. The two mixtures are then poured into a cylindrical mold to form each half of the cylinder, which is then placed into a vacuum chamber again for 15 minutes, after which each cylindrical slab which make up the phantom take 24 hours to cure.

The two halves combined together form a 5 cm thick homogeneous slab, with

measured $\mu_a = 0.16 \text{ cm}^{-1}$ and $\mu'_s = 10.1 \text{ cm}^{-1}$ at 690 nm. The two absorbing inclusions are each a cuboid with height and width of 1 cm and length of 4.5, separated by 1.6 cm.

The cuboid inclusions have the same μ'_s as the slab and the cuboids have 10 and 3 times the absorption of the background, respectively. The $10\times$ absorption results in a highly absorbing rod, where we define $\Delta\mu_a = 1.28 \text{ cm}^{-1}$ for ground truth comparison, whereas the $3\times$ cuboid has $\Delta\mu_a = 0.33 \text{ cm}^{-1}$. Although the $10\times$ absorbing rod has high absorption, the $3\times$ rod is closet to realistic values found for breast tumours. This experimental setup allows us to test our algorithm to recover realistic tubular structures accurately even when highly absorbing areas, exceeding the Born approximation limit, are present in the medium [84, 43].

4.3.2 Scanning measurments

Two different measurements are performed to test the robustness of the approach when inclusions are angled with respect to scanning direction. The angle φ is defined as the angle between the direction of the cuboids and the scanning direction, as shown in Fig. 4.6. The first set is obtained where the inclusions are exactly perpendicular to the scanning direction, $\varphi = 90^\circ$, and a second set where $\varphi = 30^\circ$. These source detector placement is shown in Fig. 4.6 where the ground truth used for error metric for each case is shown in Fig. 4.7. Both of these experiments are performed at the Tufts Medical Center. The instrument in the clinic performs a two dimensional planar

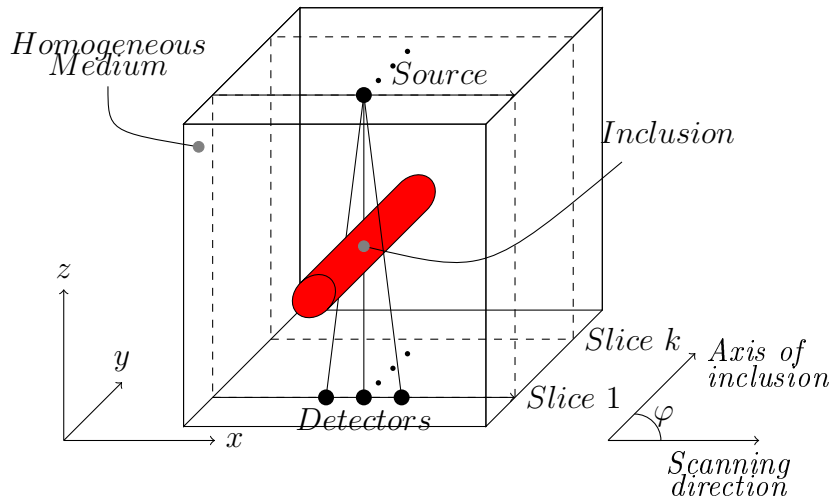


Figure 4.6: *The setup of sources and detectors for simulation reconstructions. Same orientation of axes is used for experimental data. The angle φ represents the angle between the axis of the inclusion, along y in the figure, and the scanning direction, along x in the figure.*

scan, with an illumination and detection fiber operating in transmission geometry. For three different detector positions at $x_d = \{\pm 1, 0\}$ cm a 4 mm diameter fiber is placed on the opposite side of the phantom. For each scan 32 light sources are considered with 0.2 increments resulting in 96 source-detector pairs for each slice, where slices are spaced 0.2 cm along the y -axis. Using a Xenon arc lamp light source emitting 13 mW, optical data is then found by spatially sampling 25 points/cm² at wavelengths from 650-900 nm. The light is collected by the fiber attached to a spectrograph (Model No. SP-150, Acton Research Corp., Acton, MA) with a 2 mm wide slit entrance. The wavelengths are resolved by a cooled CCD Camera (Model No. DU420A-BR-DD, Andor Technology, South Windsor, CT) giving a spectral sampling rate of 0.5 nm⁻¹. Reconstructions are performed for wavelength 690 nm.

As in Section 4.2 the incident field needs to be estimated in order to apply the Born approximation. To achieve this an extra homogeneous slab was cured, to generate a solid 5 cm thick cylinder with the background absorption coefficient and scattering detailed in Section 4.3.1. As with the actual phantom, it was ensured that no air gap formed between the slabs. As discussed in Section 3.3, image reconstructions in this experimental setup we utilize analytical Green's functions for the forward model in 3.22, where we consider slab geometry Green's function given by (3.10).

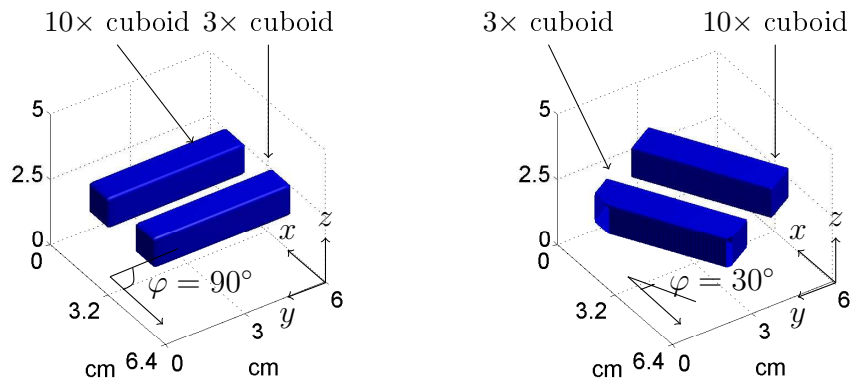


Figure 4.7: *Calculated ground truth images for phantom angled at $\varphi = 90^\circ$ and $\varphi = 30^\circ$ relative to scanning direction along the x-axis.*

Chapter 5

Hyperspectral PaLS Based Reconstruction

5.1 Parametric level-set method

To counter the ill-posedness of the DOT problem we employ a Parametric Level-Set Method (PaLS) [1]. For the purpose of this thesis we assume that all chromophore concentrations and diffusion coefficient perturbations are co-located. This choice is supported by reports in literature, where increase in hemoglobin and water concentration along with scattering power are located at the cancer location and the lipid concentrations increase at the same location [20, 97, 115]. This means that the geometry of the anomaly in the medium is the same for all chromophores and diffusion amplitude. The domain $\Omega \subset \mathcal{F}$ represents the support of the objects of interest, and

\mathcal{F} represents the homogeneous background within which the abnormality is located, shown in Fig. 5.1(a).

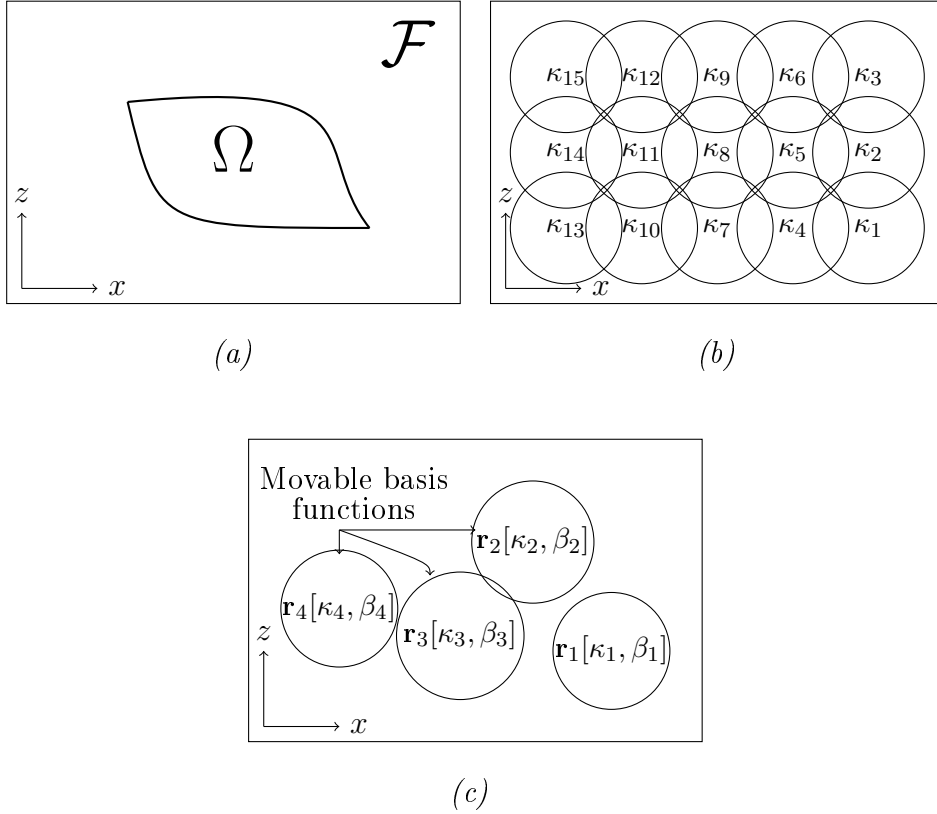


Figure 5.1: (a) Definition of domains used for the parametric level-set methods as shown in Chapter 2. (b) Circles represent example basis functions placed on a fixed grid in the imaging medium. The iteration process evolves κ_i to the estimated anomaly structure. (c) Example of movable basis functions placed in the imaging medium. The iteration process evolves κ_i and ψ_i towards the estimated anomaly structure

Since the same support is used for each chromophore concentration the characteristic function describing the shape is defined as

$$\chi(\mathbf{r}) = \begin{cases} 1 & \text{if } (\mathbf{r}) \in \Omega, \\ 0 & \text{if } (\mathbf{r}) \in \mathcal{F} \setminus \Omega. \end{cases} \quad (5.1)$$

Then each image to be reconstructed can be written as

$$\mathbf{c}_k(\mathbf{r}) = \chi(\mathbf{r})c_k^a + [1 - \chi(\mathbf{r})]c_k^b \quad (5.2)$$

where $i = 1, 2, \dots, N_c + 1$. In this formulation the unknown values are the constant concentration values of the anomaly and background, c_i^a and c_i^b respectively.

The characteristic function $\chi(\mathbf{r})$ is defined to be the τ -level set of a Lipschitz continuous object function $\mathcal{O} : \mathcal{F} \rightarrow \mathbb{R}$ such that

$$\begin{cases} \mathcal{O}(\mathbf{r}) > \tau & \forall \mathbf{r} \in \Omega \\ \mathcal{O}(\mathbf{r}) = \tau & \forall \mathbf{r} \in \delta\Omega \\ \mathcal{O}(\mathbf{r}) < \tau & \forall \mathbf{r} \in \mathcal{F} \setminus \Omega \end{cases}$$

We assume that the general form of $\mathcal{O}(\mathbf{r})$ is known, so that the evolution of \mathcal{O} is required to solve the inverse problem at hand, which we achieve by expanding \mathcal{O} with known basis functions and evolving parameters that govern them.

Using $\mathcal{O}(\mathbf{r})$, $\chi(\mathbf{r})$ is written as

$$\chi(\mathbf{r}) = H(\mathcal{O}(\mathbf{r}) - \tau) \quad (5.3)$$

where H is the Heaviside step function. Shape-based reconstruction, as is presented here, requires a smooth version of $H(\cdot)$. One common approximation of $H(\cdot)$ is called the C^∞ regularization and is computed as [1]

$$H_{1,\epsilon} = \frac{1}{2} \left(1 + \frac{2}{\pi} \arctan \left(\frac{\pi x}{\epsilon} \right) \right). \quad (5.4)$$

This version has been commonly used in shape based applications, and is discussed in detail by [1]. Chan et al.[21] demonstrated that an alternative choice of the regularized Heaviside function is the C^2 regularization computed as

$$H_{2,\epsilon}(x) = \begin{cases} 1 & \text{if } x > \epsilon, \\ 0 & \text{if } x < -\epsilon. \\ \frac{1}{2} \left[1 + \frac{x}{\epsilon} + \frac{1}{\pi} \sin\left(\frac{\pi x}{\epsilon}\right) \right] & \text{if } |x| \leq \epsilon. \end{cases}$$

and its derivative, $\delta_{2,\epsilon}$, is derived from H_ϵ [21, 114]. By using $H_{2,\epsilon}$ the corresponding delta function $\delta_{2,\epsilon}$ is compactly supported so $\delta_{2,\epsilon}$ is only non zero for $\tau - \epsilon < \psi < \tau + \epsilon$. This choice of implementing the τ -level set is similar to a “narrow-banding” approach discussed in [1], where the values of the level set function are only updated on a narrow band around the zero level set and hence reducing the computational load. For the case of using τ level sets, this band is moved to $\tau - \epsilon < \psi < \tau + \epsilon$ and the basis functions which do not intersect with this band do not evolve at the corresponding iteration. To achieve this τ is chosen to be close to zero, while maintaining $|\tau| \geq \epsilon$.

As will be discussed in Section 6.1 we represent the object function $\mathcal{O}(x, y)$ parametrically, so instead of using a dense collection of pixel or voxel values [80], we expand \mathcal{O} and represent it by using basis functions.

$$\mathcal{O}(\mathbf{r}) = \sum_{l=1}^L \kappa_l \psi_l(\mathbf{r}) \quad (5.5)$$

where κ_l 's are the weight coefficients of each basis function and L is the number of basis functions used. The choice of basis functions is inherently an important part of

the algorithm when working with PaLS. Basis functions, belonging to the set

$$\mathcal{P} = \{\psi_1, \psi_2, \dots, \psi_L\} \quad (5.6)$$

are used to represent $\mathcal{O}(x, y)$, and can be chosen from a variety of options including polynomial or radial basis functions. For the purpose of this thesis we use compactly supported radial basis functions (CSRBFs) where we choose τ to be close to zero. These functions become exactly zero after a certain radius, while still retaining various orders of smoothness, which reduces computational cost through the sparsity that they provide. In the DOT case, where the physics in the forward model will only allow for a coarse reconstruction of the underlying structure, the use of CSRBFs is sufficient, especially for the relatively simple geometries and concentrations presented in this chapter. Letting $\psi \geq 0$ be a smooth CSRBF we denote each basis function in (5.5) as

$$\psi_l = \psi(\beta_l \|\mathbf{r} - \mathbf{r}_l\|) \quad (5.7)$$

where β_l defines the dilation factor of the CSRBF. Here $\|\cdot\|$ denotes the Euclidean norm and \mathbf{r}_l are the centers of the l^{th} CSRBF. In order to make the PaLS function (5.5) globally differentiable with respect to β and \mathbf{r}_l we implement a smooth approximation of the Euclidean norm given by

$$\|\mathbf{x}\|^\star = \sqrt{\|\mathbf{x}\|^2 + n^2} \quad (5.8)$$

where $n \neq 0$ is a small real number. Assembling our model we have

$$\mathcal{O}(\mathbf{r}) = \sum_{l=1}^L \kappa_l \psi_l(\|\mathbf{r} - \mathbf{r}_l\|) \quad (5.9)$$

For the case of fixed basis grid, shown in Fig. 5.1(b) the centers and sizes of the ψ 's in (5.9) are fixed so that the evolution of \mathcal{O} strictly involves estimating κ_l . In the case of DOT it can be useful to reduce the number of unknowns by fixing the basis functions in this way. An example of a grid like this is shown in Fig. 5.1(b). When optimizing with basis functions on a fixed grid, the width and number of the CSRBFs determines how coarse or fine the reconstruction will be. A choice of few basis functions will, on the one hand, result in a reduced number of unknowns. It will on the other hand, give a coarser estimation of the shape, which can be a problem for imaging finer more complex structures. This framework restricts the adaptability of the method to different shapes, where if a basis function is fixed to a grid point, off center relative to a center of an anomaly, will result in a reconstruction error.

A more general approach can be used where each basis function is allowed to “roam” within the imaging medium. This allows the PaLS function to pick more details, and estimating the dilation factor β allows the evolution to scale the CSRBFs where it is required. Removing the fixed grid, and instead estimating the centers of the basis functions allows for greater accuracy and adaptability for the method. Additionally, fixing the basis functions to a grid requires care along the edges of the medium, due to singularities and edge artifacts that can be encountered in DOT, as was discussed in 3. Using this approach we estimate the centers, \mathbf{r}_l , of the CSRBFs in (5.7) along with the weighting factor κ_l and the dilation factor β_l which together control the size of the basis function. For the case of a movable basis functions all

the parameters of the model would be gathered in one vector

$$\boldsymbol{\theta}^T = [c_1^a, c_2^a, \dots, c_{N_c}^b, \boldsymbol{\kappa}^T, \boldsymbol{\beta}^T, \mathbf{r}^T] \quad (5.10)$$

where

$$\begin{aligned} \boldsymbol{\kappa} &= [\kappa_1, \dots, \kappa_L]^T \\ \boldsymbol{\beta} &= [\beta_1, \dots, \beta_L]^T \\ \mathbf{r} &= [\mathbf{r}_1, \dots, \mathbf{r}_L]^T. \end{aligned} \quad (5.11)$$

For the case of a fixed grid, the parameter vector $\boldsymbol{\theta}$ does not include $\boldsymbol{\beta}$ and \mathbf{r} so $\boldsymbol{\theta}^T = [c_a^1, c_a^2, \dots, c_b^l, \boldsymbol{\kappa}^T]$. Now our linear forward model in (3.22) can be expressed as

$$\boldsymbol{\Phi}^s = \mathbf{K}(\boldsymbol{\theta}) = \mathbf{K}\mathbf{c}(\boldsymbol{\theta}) \quad (5.12)$$

The forward model has now been parametrized with a vector containing all of the unknowns, which are far fewer than what a pixel based method would attempt to estimate.

5.2 Inversion using PaLS

The inverse problem, that of using $\boldsymbol{\Phi}^s$ to recover the value of \mathbf{c} , is solved with the PaLS algorithm by implementing it with a Levenberg-Marquardt optimization problem of the form

$$\hat{\mathbf{c}} = \underset{\mathbf{c}}{\operatorname{argmin}} \|\mathbf{W}(\mathbf{K}(\boldsymbol{\theta}) - \boldsymbol{\Phi}^s)\|_2^2 \quad (5.13)$$

The \mathbf{W} matrix reflects the structure of the noise corrupting the data, containing the reciprocal of the covariance of the measurement [48]. While a Poisson model is

technically the most appropriate for DOT data, as is frequently done [55] for large photon counts we employ a Gaussian approximation in which independent, zero mean Gaussian noise is added to each simulated datum. The reason for this is that with a sufficiently large number of detected photons, the Poisson statistics can be approximated by a Gaussian distribution [85]. Letting σ_m^2 denote the variance of the noise corrupting the m^{th} elements of Φ^s , \mathbf{W} is constructed as a diagonal matrix with $1/\sigma_m$ the m^{th} element along the diagonal. For the experimental and simulated data the variance is calculated from

$$\sigma_m^2 = \Omega(m)10^{-\frac{SNR_m}{10}}. \quad (5.14)$$

where $\Omega(m)$ corresponds to the photon count for each source-detector pair. The SNR for each element of Φ^s is then calculated from

$$SNR_m = 10\log_{10}(\Omega(m)/\sqrt{\Omega(m)}). \quad (5.15)$$

In experimental data $\sqrt{\Omega(m)}$ is the standard deviation of the Poisson noise distribution.

The minimization of the cost function is then achieved by the Levenberg-Marquardt algorithm. For that purpose an error vector is introduced

$$\epsilon = \mathbf{W}(\mathbf{K}(\theta) - \Phi^s). \quad (5.16)$$

which can be used to write the cost function in term of ϵ as

$$M(\theta) = \epsilon^T \epsilon \quad (5.17)$$

In order to employ the Levenberg-Marquardt algorithm, the calculation of the Jacobian matrix \mathbf{J} is required. The Jacobian contains derivatives of $\boldsymbol{\epsilon}$ with respect to each element in the parameter vector $\boldsymbol{\theta}$

$$\mathbf{J} = \left[\frac{\partial \boldsymbol{\epsilon}(\boldsymbol{\theta})}{\partial \{c_a^1, \dots, c_b^l, \boldsymbol{\kappa}\}} \right] \quad (5.18)$$

where details on calculating \mathbf{J} are given in Appendix A. The solution is then obtained by updating $\boldsymbol{\theta}$ at each iteration as $\boldsymbol{\theta}^{n+1} = \boldsymbol{\theta}^n + \mathbf{h}$ where \mathbf{h} is the solution to the following linear system, previously discussed in Section 2.4,

$$(\mathbf{J}^T \mathbf{J} + \rho \mathbf{I}) \mathbf{h} = -\mathbf{J}^T \boldsymbol{\epsilon} \text{ with } \rho \geq 0 \quad (5.19)$$

where \mathbf{I} is the identity matrix, ρ is the damping parameter affecting the size and direction of \mathbf{h} and found via an appropriate line search algorithm [76].

The damping parameter ρ in (5.19) is noted to have several effects, most notable, for all $\rho > 0$ the coefficient matrix is positive definite, which ensures that \mathbf{h} is a descent direction. The damping parameter influences both the direction and the size of the step, which leads to a method without a specific line search. The choice of initial ρ value is related to the size of elements in $A_0 = \mathbf{J}(\mathbf{x}_0)^T \mathbf{J}(\mathbf{x}_0)$, by letting

$$\rho_0 = \eta \cdot \max_j (a_{jj}^{(0)}) \quad (5.20)$$

where η is manually chosen to be $\eta = 10^{-3}$. This value can be decreased to 10^{-6} if there is confidence that the initial guess is close to a good estimation.

To judge when the Levenberg-Marquardt algorithm has reached an optimal solution we employ the discrepancy principle [106] as a stopping criteria when iterating

(5.19). In that the iterations are stopped when the norm of the residual has reached the noise level within a certain tolerance, given by

$$\|\mathbf{K}(\boldsymbol{\theta}_u) - \boldsymbol{\Phi}^s\|_2 < \delta. \quad (5.21)$$

When estimating the parametric vector, we employ a cyclic coordinate decent strategy [109] Essentially this is equivalent to estimating the shape only at even iterations and the concentration values at odd iterations. This is repeated until stopping criteria is reached. This process is expressed in pseudo-code in Algorithm 1, where \mathbf{J}_v and \mathbf{J}_s denote the Jacobian strictly for the concentration value and shape, respectively, and τ_i represents a tolerance for the stopping criteria.

Algorithm 1 Matlab-like pseudo-code for estimating shape and concentration value simultaneously

```

while  $\epsilon \leq \tau_1$  do
  while  $\epsilon \leq \tau_2$  do
     $(\mathbf{J}_v^T \mathbf{J}_v + \rho^n \mathbf{I}) \mathbf{h}_{values} = -\mathbf{J}_v^T \boldsymbol{\epsilon}$ 
  end while
  while  $\epsilon \leq \tau_3$  do
     $(\mathbf{J}_s^T \mathbf{J}_s + \rho^n \mathbf{I}) \mathbf{h}_{shape} = -\mathbf{J}_s^T \boldsymbol{\epsilon}$ 
  end while
   $\boldsymbol{\theta}^{n+1} = \boldsymbol{\theta}^n + [\mathbf{h}_{values}; \mathbf{h}_{shape}]$ 
end while

```

5.3 Comparing to a Pixel-based reconstruction

To judge the improvement of moving to a low-order parametric model, we perform pixel-based reconstructions to compare with the results obtained with the PaLS algorithm. Pixel based reconstruction for DOT involves a significantly rank-deficient problem, where the number of pixels far out number the number of measurements. For the pixel-based image formation the reconstruction method presented as the solution to a non-negative least squares optimization problem of the form

$$\hat{\mathbf{c}} = \underset{\mathbf{c} \geq 0}{\operatorname{argmin}} \|\mathbf{W}(\Phi^s - \mathbf{K}\mathbf{c})\|_2^2 + \|\mathbf{L}\mathbf{c}\|_2^2 \quad (5.22)$$

where for any vector \mathbf{x} , $\|\mathbf{x}\|_2^2 \equiv \mathbf{x}^T \mathbf{x}$ is the squared two-norm of \mathbf{x} . The first term in (5.22) requires that the reconstructed concentration images yield simulated data that are consistent with the observations Φ^s . Following [48], the weight matrix \mathbf{W} reflects the structure of the noise corrupting the data.

The second term on the right-hand side in (5.22) represents the regularization. As discussed in the Chapter 2, in this work we use a smoothness-type regularizer in which the amount of regularization is allowed to vary for each chromophore. Due to sensitivity of the reconstruction to the regularization parameters the optimal parameter for one chromophore is not necessarily the optimal value for another. Separating the parameters for each chromophore allows the reconstruction to optimize it for each chromophore and easily include many different species of chromophores.

The non-negative least squares (NNLS) problem is solved by using the *lsqnonlin* algorithm in MATLAB. This algorithm uses a trust-region reflective algorithm that

employs matrix-vector products instead of having to compute the value of the sum of squares from (5.22) [26]. The \mathbf{K} matrix is the Jacobian matrix of the measurements used in our reconstruction scheme. For the case of DOT NNLS becomes highly attractive for its computational efficiency when compared to a direct solution of traditional least squares. This is due in part to the fact that computing $\mathbf{K}^T\mathbf{K}$ can require large amounts of computational overhead. The number of voxels in a given solution becomes somewhat limited by the necessity of solving the system defined by $\mathbf{K}^T\mathbf{K}$ or some regularized version thereof. Because of the design of \mathbf{K} when the number of voxels increases, the size of $\mathbf{K}^T\mathbf{K}$ and the computation required for elimination both increase much more rapidly than with NNLS [82].

As discussed in the introduction a good initial guess is important to obtain a good results. The approach we use here is as follows. We start by solving (3.2) ignoring the positivity constraint in (5.22) with *lsqnonlin* and using the the method discussed in Section 5.3.1 below for determining the optimal regularization parameters. Setting all negative values in the \mathbf{c} vector to zero then provides the initial guess for the constrained form of the problem. This initialization process allows us to obtain good results from both simulation and experimental data. Like the unconstrained problem the constrained problem is solved with *lsqnonlin* and optimal regularization parameters are chosen independently in each case.

5.3.1 Selecting optimal regularization for multiple chromophores

The challenge lies in how to choose the α parameter embedded in \mathbf{L} in (5.22). There exist formal methods for choosing the parameter, such as generalized cross-validation (GCV) or the L-curve, but it is not necessary to use them in all cases [61]. The appropriate value may be selected by trial and error and visual inspection. Larger α makes the system better conditioned, but this new system is farther away from the original system, the system without regularization. Under the noise-free assumption, the algorithm is insensitive to the choice of α , making it straightforward to select small values for α to generate results with high accuracy. When noise is encountered, however, α may need to be made much larger. Furthermore the effect of having two separate regularization parameters α_1 and α_2 is explored. It is shown how the mean square error behaves for reconstruction of two chromophores and how having separate parameters for each hemoglobin increases the quality of the reconstruction. For that case the regularization parameters are incorporated into the matrix and then \mathbf{L} takes the form

$$\mathbf{L} = \begin{bmatrix} \alpha_1 \begin{bmatrix} \nabla_x \\ \nabla_y \end{bmatrix} & 0 \\ 0 & \alpha_2 \begin{bmatrix} \nabla_x \\ \nabla_y \end{bmatrix} \end{bmatrix} \quad (5.23)$$

To generalize this to n chromophores, one might want to have different regularization parameters for each chromophore. Given the structure of the vector \mathbf{c} defined in (3.21), the regularization matrix takes the form

$$\mathbf{L} = \mathcal{D}(\boldsymbol{\alpha}) \otimes \begin{bmatrix} \nabla_x \\ \nabla_y \end{bmatrix} \quad (5.24)$$

where $\boldsymbol{\alpha}^T = [\alpha_1 \ \alpha_2 \ \dots \ \alpha_{N_c}]$ is a vector of N_c regularization parameters, $\mathcal{D}(\mathbf{x})$ is a diagonal matrix with the elements of the vector \mathbf{x} on the main diagonal, ∇_x and ∇_y are matrices representing first difference approximations to the gradient operators [50] in the horizontal and vertical directions respectively, and for matrices \mathbf{A} and \mathbf{B} , $\mathbf{A} \otimes \mathbf{B}$ is the Kronecker product [70] of \mathbf{A} and \mathbf{B} .

The choice of the optimal regularization parameters is done by inspecting the L-hypersurface, which are plotted in Fig. 5.4 for the concentrations images shown in Fig. 5.3 [10]. To construct the L-hypersurface we introduce the following quantity

$$\mathbf{z}(\boldsymbol{\alpha}) = \|\Phi^s - \mathbf{K}\hat{\mathbf{c}}(\boldsymbol{\alpha})\|_2^2 \quad (5.25)$$

For a single constraint the L-hypersurface reduces to the conventional L-curve which is simply a plot of the residual norm versus the norm of the regularized solution drawn in an appropriate scale for a set of admissible regularization parameters. This allows us to optimize the regularization to compromise between the minimization of these two quantities. For a hypersurface the optimal regularization parameters then should appear where the curvature is greatest in the surface, in other words in the corner of the surface. This corner in the hypersurface which should correspond to a point

where the error estimation is minimal. This curvature is computed as a special case of Gaussian curvature [46] from

$$\mathbf{H} = \frac{\mathbf{r}\mathbf{t} - \mathbf{s}^2}{\mathbf{w}^4} \quad (5.26)$$

where we have

$$\mathbf{w}^2 = 1 + \mathbf{p}^2 + \mathbf{q}^2.$$

In (5.26) each element is a partial derivative of the surface which we write as

$$\mathbf{p} = \frac{\partial \mathbf{z}}{\partial \alpha_1}, \quad \mathbf{q} = \frac{\partial \mathbf{z}}{\partial \alpha_2}, \quad \mathbf{r} = \frac{\partial^2 \mathbf{z}}{\partial \alpha_1^2}, \quad \mathbf{t} = \frac{\partial^2 \mathbf{z}}{\partial \alpha_2^2}, \quad \mathbf{s} = \frac{\partial^2 \mathbf{z}}{\partial \alpha_1 \partial \alpha_2}. \quad (5.27)$$

Using this, an optimal regularization parameter can be chosen for the pixel based reconstructions, as demonstrated in Section 5.6.1.

5.4 Implementing Hyperspectral information

Due to computational load, hyperspectral information has to be implemented efficiently when constructing the forward model. Even though computational power increases year to year, the amount of data that can be included with hyperspectral information is significant. This is especially important when performing pixel based reconstructions where for realistically sized problems, it is difficult to store the full \mathbf{K} matrix in memory. The processing methods developed in this thesis require only the result of multiplying \mathbf{K} or \mathbf{K}^T (the transpose of \mathbf{K}) by appropriately sized vectors. Hence, we need only compute and store the N_λ matrices \mathbf{K}_l as well as the $N_\lambda \times N_c$

array of extinction coefficients. Then computation of the product $\mathbf{K}\mathbf{c}$ can be carried out using the Matlab-like pseudo-code in Algorithm 2 with a similar approach possible for evaluating $\mathbf{K}^T\boldsymbol{\Phi}^s$.

Algorithm 2 Matlab-like code for computing $\mathbf{K}\mathbf{c}$ product

```

for  $l = 1$  to  $N_\lambda$  do
    for  $k = 1$  to  $N_c$  do
         $\Phi_c^s = \Phi_c + \varepsilon_k(\lambda_l)\mathbf{K}_k$ ;
    end for
     $\boldsymbol{\Phi}^s = [\boldsymbol{\Phi}^s; \boldsymbol{\Phi}_c^s]$ ;
end for
```

5.5 Simulation analysis

To best understand the utility of a hyperspectral data set, we employ the Born model to generate simulated data. Though this may not be realistic, it allows us to avoid the confounding factor of model mismatch in evaluating the inversion method being considered in this chapter. Moreover, the shortcomings of this approach will be mitigated in Section 5.6.2, where we consider the processing of experimental data which, obviously, are not the product of the Born model. Specifically, the data we use for our simulation analysis are computed as

$$\boldsymbol{\Phi}^s = \mathbf{K}\mathbf{c} + \mathbf{n} \quad (5.28)$$

where \mathbf{c} represents the simulated concentration images for all chromophores and diffusion amplitude, whereas \mathbf{n} represents additive noise. Specifically, as in [48] \mathbf{n} is

a vector of zero mean, independent Gaussian random variables with variances σ_m^2 , defined in (2.8), chosen such that a pre-determined signal-to-noise ratio (SNR) is achieved. This SNR is calculated from (5.15).

The reconstructed images are evaluated in three ways: 1) through visual inspection, 2) using mean square error (MSE) as a measure of overall quantitative accuracy for each chromophore, and 3) examining the Dice coefficient to judge how well the concentrations are localized [65, 107]. For the k^{th} chromophore, the MSE is computed by using the following equation

$$MSE_k = \frac{\|\mathbf{c}_k - \hat{\mathbf{c}}_k\|_2}{\|\mathbf{c}_k\|_2} \quad (5.29)$$

If S is the reconstructed image and G is the ground truth created for each set, the Dice coefficient between S and G is

$$D(S, G) = \frac{2|S \cap G|}{|S| + |G|}. \quad (5.30)$$

Since $|S \cap G|$ contains all pixels that belong to the detected segment as well as the ground truth segment, if S and G are equal the Dice coefficient is 1, indicating an accurate reconstruction. To compute the $D(S, G)$ we use the characteristic function, χ , which essentially works as a binary map of the reconstructed anomaly where the object of interest is represented by 1's.

The simulated data was generated in infinite geometry where separations were set to 5 cm. In simulations, we reconstruct concentration images of oxygenated and deoxygenated hemoglobin, HbO_2 and HbR respectively, along with lipid and water

concentration and scattering amplitude. These chromophores are chosen since they mainly cause near-infrared absorption in the breast [17], and breast cancer tumours have been found to have higher HbO₂ and HbR concentrations than normal tissue [100].

The concentration in the simulated images are defined in units of millimolars or millimoles per liter, mM, for HbO₂ and HbR. Values for Ψ and b used to generate data are obtained from [102] for the female breast. Values for μ_a are calculated from the extinction coefficients, in the unit of cm⁻¹/mM, obtained from data tabulated by Scott Prahl [88]. For water and lipid the concentrations are in percent by volume and the diffusion amplitude is measured in units of millimeter. The background has HbR concentration of 0.01 mM, HbO₂ concentration of 0.01 mM, lipid concentration of 32%, water concentration of 13% and Ψ' is set to 1.6 mm. The target concentration of the object of interest is set to 0.015 mM, 0.012 mM, 50 %, 20 % and 0.25 mm for HbO₂, HbR, lipid, water and $\Delta\Psi'$, respectively.

The simulation set is created with all chromophore concentrations and diffusion perturbations in the same location with different target values. The ground truth images for simulations are shown in Fig. 5.3. Reconstruction is done for these images to explore effects of adding hyperspectral information to the problem, i.e. the improvement in quantitative accuracy and the reduction of crosstalk where a concentration of one chromophore creates a false concentration in an image for another chromophore as well as the performance of the shape based approach. The process

is initialized with 21 Gaussian basis functions with width of approximately 8 pixels placed uniformly on a grid over the whole medium to be imaged. A representative image of the order of the basis functions is shown in Fig. 5.1(b). For all experiments presented in this chapter, the κ_l 's weight coefficients are initialized to 1.

5.6 Results

5.6.1 Simulations

Table 5.1: *The MSE is compared for each chromophore for multiple wavelength choices. For the 8 wavelength case optimal wavelengths are used, where 176 wavelengths are equally spaced.*

Pixel based method					
# λ	MSE HbO ₂	MSE HbR	MSE Lipid	MSE H ₂ O	MSE D
8	0.075	0.030	0.048	0.010	0.052
176	0.062	0.021	0.034	0.015	0.030
PaLS method					
# λ	MSE HbO ₂	MSE HbR	MSE Lipid	MSE H ₂ O	MSE D
8	0.070	0.030	0.120	0.060	0.080
176	0.019	0.008	0.010	0.020	0.010

In Fig. 5.2 reconstruction results using the pixel based method are shown for 8 wavelengths, $\lambda = [660, 734, 760, 808, 826, 850, 930, 980]$ nm and hyperspectral reconstruction using 176 wavelengths, which are equally spaced over the 650-1000 nm range. In the 8 wavelength case the 6 first wavelengths are optimally chosen according

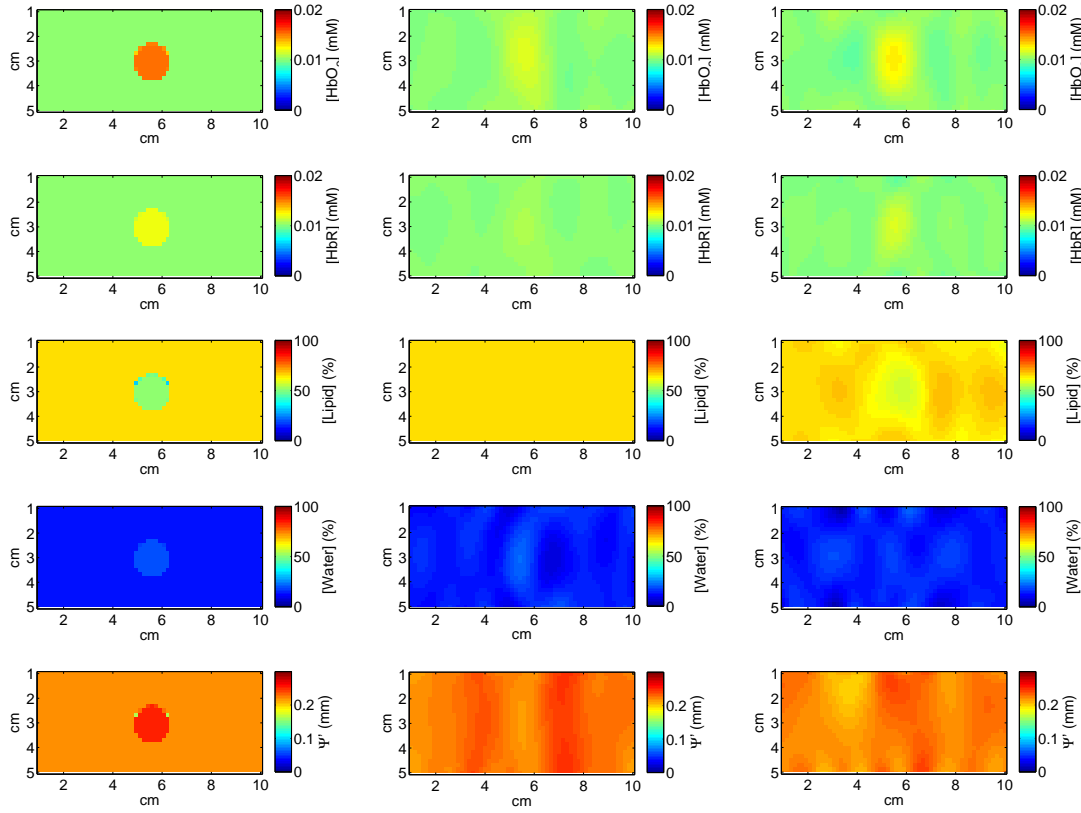


Figure 5.2: *Reconstruction using a pixel based method. Leftmost column are ground truth images, middle column of images are generated with 8 wavelengths and rightmost images are generated with 176 wavelengths. From top to bottom the rows show HbO_2 , HbR , lipid, water and diffusion amplitude, respectively. Concentration units are in mM .*

to [37] with two wavelengths added where water and lipids have peak absorption. Reconstructed images created with the PaLS method are shown in Fig. 5.3. In simulations the SNR is set to 30 dB, as it is defined by (5.14) and (5.15). When comparing the pixel based reconstruction in Fig. 5.2 to the PaLS reconstruction in Fig. 5.3, it is evident that the PaLS method provides superior reconstructions. Examining the PaLS results, the 8 wavelength case shows reasonable accuracy along

Table 5.2: $D(S, G)$ is compared for each chromophore for multiple wavelength choices. In each case the reconstructions are done with equally spaced wavelengths over the spectrum except for the 8 wavelength case. $D(S, G)$ is calculated comparing 80% of the target peak to the reconstruction.

Pixel based method					
# λ	$D(S, G)$ HbO ₂	$D(S, G)$ HbR	$D(S, G)$ Lipid	$D(S, G)$ H ₂ O	$D(S, G)$ D
8	0.12	0.088	0.089	0.65	0.8
176	0.554	0.1085	0.043	0.41	0.09

PaLS method	
# λ	$D(S, G)$
8	0.60
176	0.99

the x axis but rather diffuse results in y . We also see noticeable artifacts in the reconstructions. Considering the concentration values, the values for HbO₂, HbR and water concentration come close to the actual value. Moving to hyperspectral information, the reconstruction becomes more accurate, estimating the shape close to the ground truth. It should also be noted that the runtime for each reconstruction for the PaLS method is significantly shorter compared to the pixel-based method. A PaLS reconstruction takes around 30 seconds, which is 3-4 times faster than a pixel-based method. Additionally, we do not employ any regularization parameters, removing the computational load of selecting the optimal regularization parameters. This is a major improvement in moving from a pixel-based approach to the PaLS method.

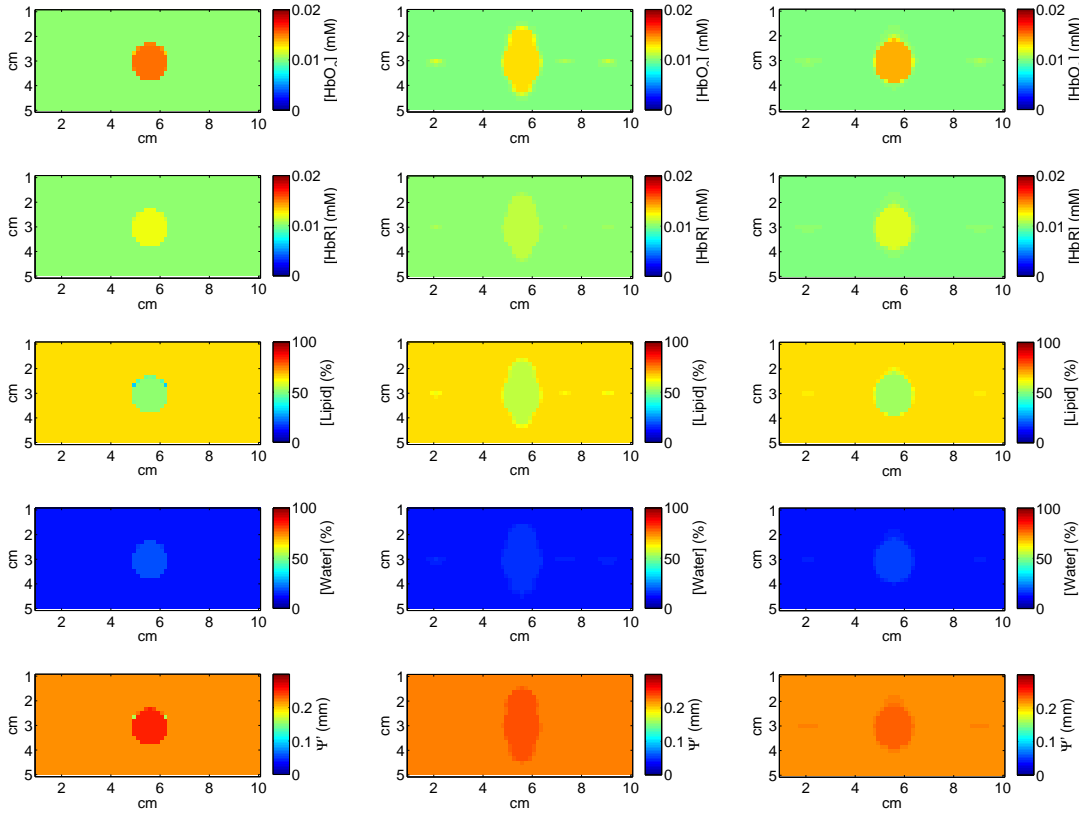


Figure 5.3: *Reconstruction using the PaLS method. Leftmost column are ground truth images, middle column of images are generated with 8 wavelengths and rightmost images are generated with 176 wavelengths. From top to bottom the rows show HbO_2 , HbR , lipid, water and diffusion amplitude, respectively. Concentration units are in mM.*

The comparison of the Dice coefficient between the PaLS method and pixel-based is tricky, since for the pixel-based method the Dice coefficient is plotted as a function of a threshold. This threshold is required to create a binary map of the location on the anomaly. If the threshold is chosen to only leave extreme peak concentration values in each image, the Dice coefficient would be low due to edge artifacts as in Fig. 5.6(b). Therefore, in simulations we compare $D(S, G)$ for the pixel based reconstructions

using a threshold of 80% to $D(S, G)$ of the PaLS reconstructions. The improvement of the PaLS method is confirmed quantitatively through $D(S, G)$ and MSE displayed in Table 5.2 and Table 5.1, respectively. The Dice coefficient, shown in Table 5.2, gives a clear view of how the shape estimation improves by added wavelengths, where $D(S, G)$ approaches 1 for the hyperspectral case and the PaLS method shows superior performance in the MSE values.

Because we know the ground truth for these simulations, it is possible to determine optimal values (i.e., the one that minimized the MSE) for α_1 and α_2 . For a simple chromophore concentrations as shown here, choosing the regularization parameters is an easy problem. The reason for separating the regularization parameters in this case is that the MSE for HbR reaches a lower value for a slightly different parameter than HbO₂.

The importance of separating the regularization parameters becomes even more evident when regularizing more complex concentration sets. When doing reconstruction for more complicated sets the lowest MSE values for HbO₂ and HbR occur at two very different values. For this set the separation of the regularization parameters is very important. Using only one regularization parameter in this set and more complicated ones, would result in a trade off between reconstructions of chromophores. To reduce that trade off the separation of the chromophores becomes very important. This separation becomes even more important when dealing with data sets with low

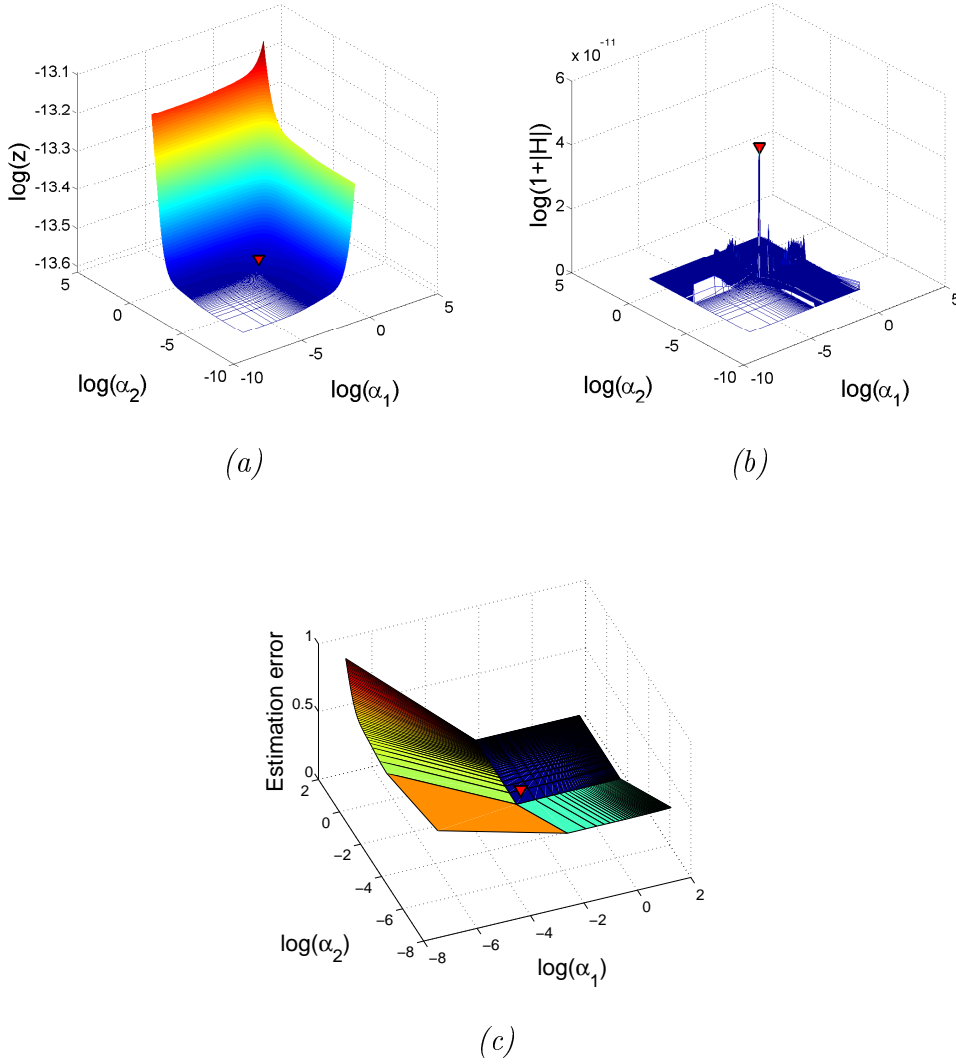


Figure 5.4: (a) L -hypersurface, defined by (5.25) plotted against regularization parameters. (b) H curvature, defined by (5.26), computed for the L -hypersurface. (c) Error estimation surface, defined by (5.31), plotted against regularization parameters. The optimal regularization parameters are marked in each case with a red arrow.

SNR values such as true measurement data. The L -hypersurface and curvature computation are additionally compared to the estimation error, which is available when the ground truth is known, as in simulations presented here. The estimation error e

is computed by

$$e = \|\mathbf{c} - \hat{\mathbf{c}}\|_2^2 \quad (5.31)$$

Demonstrating the choice of the α parameters, example reconstruction for HbO_2 and HbR with corresponding hypersurface is shown in Fig. 5.5 and 5.4, respectively.

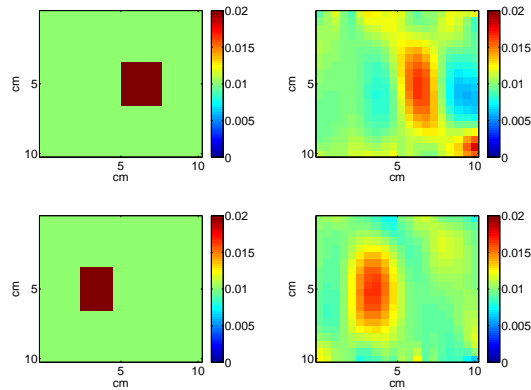


Figure 5.5: *Reconstruction for HbO_2 and HbR using a pixel based method. Upper row is for the HbO_2 chromophore and the lower for HbR . Concentration units are in mM. Reconstruction performed for 176 equally spaced wavelengths.*

By examining hypersurface and curvature in Fig. 5.4 it is evident that this method is useful when different levels of regularization is needed. In pixel-based reconstructions that are presented in Section 5.4 the choice of α for HbO_2 , HbR and $\Delta\Psi$ were performed using the hypersurface method, while it was unnecessary for the regularization for water and lipid which were less sensitive to regularization.

5.6.2 Experimental validation

Pixel based reconstructions of absolute concentrations for both experimental sets are shown in Fig. 5.6 and PaLS approach reconstructions in Fig. 5.7.

A comparison of the absolute concentrations, $\widehat{\mathbf{c}}_i$ and relative concentration, $\widehat{\mathbf{c}}_i^r$ to target concentration values is done to test the accuracy of the reconstructions. The relative concentrations for ink are calculated as

$$\widehat{\mathbf{c}}_{ink}^r = \widehat{\mathbf{c}}_{ink} / (\widehat{\mathbf{c}}_{ink} + \widehat{\mathbf{c}}_{dye}) \quad (5.32)$$

and similarly for dye [41, 47]. The relative concentration is calculated from the peak concentration value in each reconstruction. This allows us to inspect how well our approach manages to separate and estimate each species of chromophores in the process.

As expected, the hyperspectral information provides improved reconstruction for both the pixel-based and PaLS methods. Focusing on the PaLS methods, it is evident that forming the reconstruction with shape-based constraints yields improved results. The estimation of relative concentrations and MSE of the absolute values are examined in Table 5.4 and Table 5.5 for the pixel-based and PaLS method, respectively. The relative concentration values are better estimated in both cases using the PaLS method, although the hyperspectral method does not show significant improvement for experimental set 2, which was also the case for the pixel based method. Examining the images along with the MSE values for experimental set 1, Fig. 5.6-5.7(a) and (c), it is noticeable how the reconstruction does not resolve the structure particularly well along the x axis. This is somewhat unexpected since in DOT resolving depth information, on the y axis, is usually the more difficult problem. This is noticeable for both the pixel based and PaLS methods, although the PaLS method outperforms

the pixel based method, especially in removing edge artifacts. This smear in the x direction is most likely a combination of how the Gaussian basis are placed within the imaging medium, and measurement error in placing the source and detectors when taking the reference measurement.

For both experimental sets, the PaLS method resolves the location and the shape of the inclusion more accurately, which is verified by the calculation of the Dice coefficient shown in Table 5.3. The improvement is notable when compared to the pixel-based reconstruction. As discussed in Section 5.6.1 a choice of a threshold is needed to compare $D(S, G)$ between pixel based reconstructins and the PaLS method. For the experimental reconstructions we use a threshold of 50% to compare $D(S, G)$ of the PaLS reconstructions. This demonstrates the usefulness of the PaLS method for correctly and accurately localizing the anomaly. The PaLS method does very well with eliminating edge artifacts that were severe when doing pixel-based reconstructions for the same data set. These effects are very noticeable in Fig. 5.6(b) and (d), where, especially in the multispectral case, the edge artifacts were significant. Comparing that to the same data in Fig. 5.7(b) and (d) it is obvious that the improvement is significant. It is notable in Fig. 5.7(b) and (d) that the reconstructed inclusion appears a little bit off center from where the actual location is centered. This is due to the fixed grid of basis functions, where the closest grid point is off center from the true location.

Table 5.3: $D(S, G)$ is compared for each chromophore for multiple wavelength choices. In each case the reconstructions are done with equally spaced wavelengths over the spectrum except for the 6 wavelength case where we use optimally chosen wavelengths. $D(S, G)$ is calculated comparing the half maximum of the target peak to the reconstruction.

Pixel based method					PaLS method		
	$D(S, G)$ Set 1		$D(S, G)$ Set 2		# λ	$D(S, G)$ Set 1	$D(S, G)$ Set 2
# λ	Ink	Dye	Ink	Dye			
6	0.143	0.113	0.139	0.145	6	0.27	0.33
126	0.142	0.114	0.145	0.140	126	0.37	0.80

5.7 Discussion

In this chapter, using simulations and experimental measurements we have shown that the PaLS method provides more accurate estimation of chromophore concentrations than a regularized pixel-based inversion scheme. Hyperspectral information results in improved performance in terms of both MSE and spatial localization as measured using the Dice coefficient. The parametric approach is shown to give significant improvements to image reconstruction, decreasing run time of the iterative process and increasing the quality of reconstructed images. The PaLS method is also easily expandable to more complicated problems where multiple geometries need to be considered.

Physical measurements were also performed to demonstrate these advantages for actual measurement data. Although exact concentration values were not achieved,

Table 5.4: Comparison of $\hat{\mathbf{c}}_i$ and $\hat{\mathbf{c}}_i^r$ to target concentration values for experimental results, for the pixel-based method. Best performance is highlighted in bold.

Experimental set 1, 10% ink and 90% dye					
Fig.	# λ	Species	$\hat{\mathbf{c}}_i$ [%]	$\hat{\mathbf{c}}_i^r$ [%]	MSE
5.6(a)	6	Ink	1	4	1.8
5.6(a)	6	Dye	27	96	1.3
5.6(c)	126	Ink	17	16	2.8
5.6(c)	126	Dye	88	84	1.2

Experimental set 2, 70% ink and 30% dye					
Fig.	# λ	Species	$\hat{\mathbf{c}}_i$ [%]	$\hat{\mathbf{c}}_i^r$ [%]	MSE
5.6(b)	6	Ink	56	82	1.8
5.6(b)	6	Dye	12	18	1.0
5.6(d)	126	Ink	65	61	1.4
5.6(d)	126	Dye	41	39	2.0

there is a notable improvement associated with hyperspectral information in conjunction with the PaLS method. Additionally, improved localization of inclusions was observed for both sets when using hyperspectral information. This emphasizes the advantage of hyperspectral information when doing reconstructions for more than one chromophore.

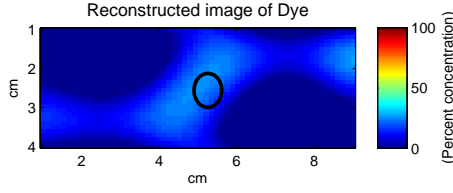
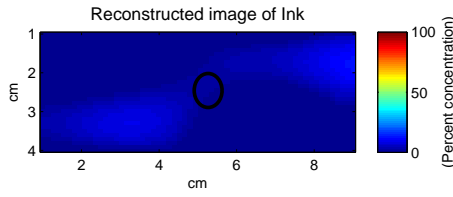
Based on the results in this chapter, we want to extend the work to address more realistic, clinical conditions. The results here show significant promise, and are encouraging to move to a more realistic situations considering more complicated shape reconstructions and placing boundary conditions on the medium. We achieve this

Table 5.5: Comparison of $\hat{\mathbf{c}}_i$ and $\hat{\mathbf{c}}_i^r$ to target concentration values for experimental results, for the PaLS method. Best performance is highlighted in bold.

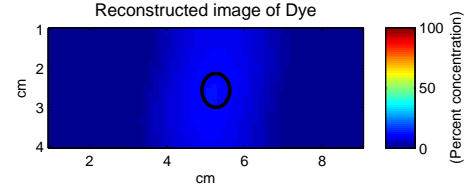
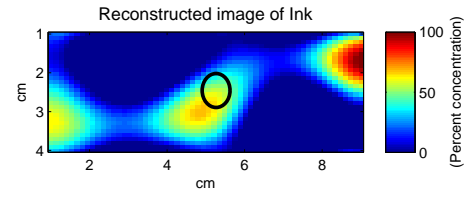
Experimental set 1, 10% ink and 90% dye					
Fig.	# λ	Species	$\hat{\mathbf{c}}_i$ [%]	$\hat{\mathbf{c}}_i^r$ [%]	MSE
5.7(a)	6	Ink	4.8	21.0	1.2
5.7(a)	6	Dye	17.9	79.0	0.9
5.7(c)	126	Ink	5.8	7.7	1.1
5.7(c)	126	Dye	69.0	92.3	0.8

Experimental set 2, 70% ink and 30% dye					
Fig.	# λ	Species	$\hat{\mathbf{c}}_i$ [%]	$\hat{\mathbf{c}}_i^r$ [%]	MSE
5.7(b)	6	Ink	38.3	80.0	1.1
5.7(b)	6	Dye	9.6	20.0	0.8
5.7(d)	126	Ink	27.6	81.0	0.6
5.7(d)	126	Dye	6.4	19.0	0.7

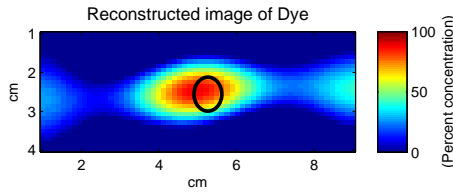
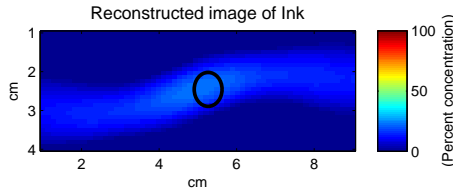
by first considering how we can expand the fixed grid basis to ensure recovery of various different shapes of chromophore concentrations, discussed in Chapter 6. To be able to estimate all shapes possible, we aim to increase the number of basis functions to include different types. To avoid over complicating the image reconstruction with a high number of basis functions we aim to pose the image reconstruction in a compressed sensing framework where few optimal basis functions estimate a complex shape. Additionally we expand the method to the estimation of 3D structures with adaptable basis functions in Chapter 7.



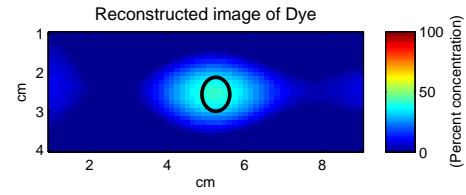
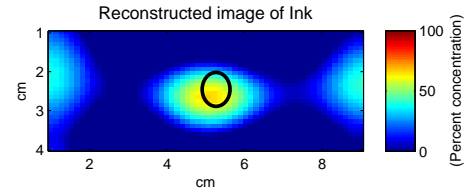
(a) 10% ink and 90% dye,
6 wavelengths used.



(b) 70% ink and 30% dye,
6 wavelengths used.

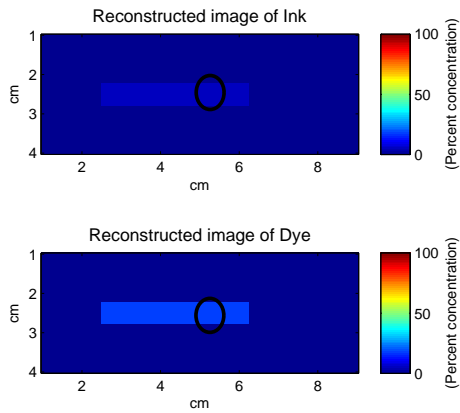


(c) 10% ink and 90% dye,
126 wavelengths used.



(d) 70% ink and 30% dye,
126 wavelengths used.

Figure 5.6: *Pixel reconstruction from both experimental sets, set 1 containing 10% ink and 90% dye and set 2 70% ink and 30% dye. Black circle denotes the true location of the inclusion.*



Chapter 6

Dictionary Approach

6.1 Introduction

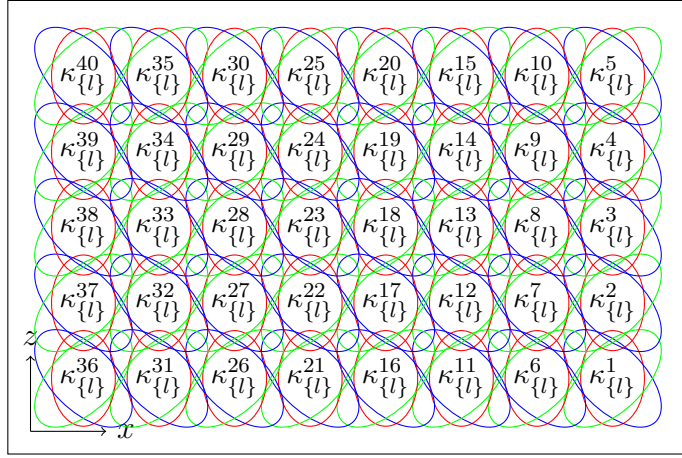


Figure 6.1: *Example basis functions placed on a fixed grid in the imaging medium, where each grid point, f , has a set of different shaped basis functions, denoted by $\{l\}$.*

As discussed in Chapter 1 the ability to recover a varied array of shapes is of great importance for DOT, so image recovery methods need to be adaptable and able to

reconstruct a wide range of shapes with accuracy. To achieve this, we consider a case where our set of basis functions \mathcal{P} is a large collection of a variety of shapes. This kind of approach has been considered extensively in compressed sensing problems where an array of known functions in a dictionary is used to recover sparse signals [45, 89]. Although our problem is not a compressed sensing problem, we consider the framework presented in [45], which is directly applicable to our problem where we consider the case of the fixed basis set, described in Section 5.1. Rauhut et al. [89] noted that most works with compressed sensing that assume sparsity, take the assumption with respect to an orthonormal basis. This can be a strict limitation in practice, and for some applications, it is more applicable to assume sparsity with respect to a defined frame or dictionary. Essentially, the method could be applied to a wide range of basis functions, to include polynomials, wavelets and Gaussians, but for our application we aim to include differently dilated CSRBFs to recover small details of the underlying structure, with selectively chosen basis functions.

For the fixed grid shown in 5.1(b) each grid point is the center for a specific ψ_l basis function. To create a redundant dictionary for our problem we amend our basis set \mathcal{P} so it contains a set of different basis functions, ψ_l^f , at each grid point f . An example of this setup is shown in Fig. 6.1. The method from Chapter 5 is modified so that the objective function \mathcal{O} described by (5.5) is created by using a dictionary matrix \mathbf{B} which contains the dense collection of basis functions at a total of F gridpoints,

defined by

$$\mathbf{B} = \begin{bmatrix} \boldsymbol{\psi}_1^1 & \boldsymbol{\psi}_2^1 & \dots & \boldsymbol{\psi}_L^F \end{bmatrix} \quad (6.1)$$

by this we define the object function using, \mathbf{B} , the redundant dictionary matrix

$$\mathcal{O} = \mathbf{B}\boldsymbol{\kappa} \quad (6.2)$$

With this formulation our parametric vector is $\boldsymbol{\theta}^T = [c_a^1, c_a^2, \dots, c_b^l, \boldsymbol{\kappa}^T]$ where $\boldsymbol{\kappa} = [\kappa_1^1, \dots, \kappa_L^F]^T$ is the weighting vector, and the c values denote the chromophore concentration values for each chromophore. Now for the set of model parameters $\boldsymbol{\theta}$, the forward model is considered to be of the linear form as written in (3.22).

In this framework we strive to achieve a sparse estimate of $\boldsymbol{\kappa}$ since \mathbf{B} contains multiple $\boldsymbol{\psi}$'s at each grid point. This directs the estimate of the shape to only select shapes from the redundant dictionary matrix \mathbf{B} that best estimate the problem. In traditional minimization problems the sparseness is induced on the solution using a ℓ_1 regularization as an added term in the cost function. Instead of employing this kind of soft constraint we restrict the $\boldsymbol{\kappa}$ to be sparse by projecting it to the ℓ_1 -norm ball at each iteration. Visual representation of this relation is shown in Fig. 6.2.

This makes the method somewhat robust to the different shapes encountered as well as using far fewer unknowns than traditional pixel based methods. To provide an accurate and simple reconstruction we implemented a hard ℓ_1 -norm constraint, described below, to improve the estimation and generate accurate images with the fewest possible basis functions. The development of this method improves on parametric shape based methods for the DOT application, especially when paired with

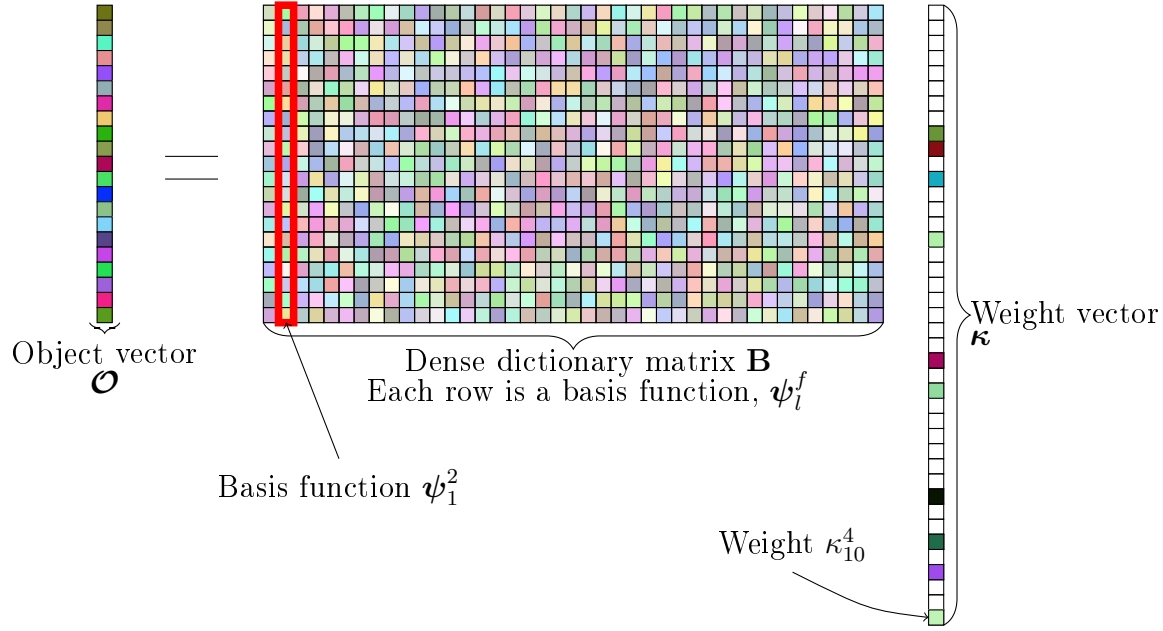


Figure 6.2: *Example of the object function \mathbf{O} as defined by (6.2). The aim is to estimate a $\boldsymbol{\kappa}$ weighting vector with induced sparsity to pick out optimal basis functions from a dense dictionary matrix \mathbf{B} where ψ_l^f represent the l^{th} function at gridpoint f .*

optical mammograms which can be used to provide prior spatial information of the medium. For the purpose of this section we considered the infinite geometry discussed in Section 3.3 as it serves as a good testing point for this approach.

6.2 Projected Levenberg-Marquardt

As before we consider the inverse problem, that of using Φ^s to recover the value of $\boldsymbol{\theta}$, but now add a extra constraint. We seek the solution to the following optimization problem.

$$\arg \min_{\boldsymbol{\theta}} \|\mathbf{W}(\mathbf{K}\mathbf{c}(\boldsymbol{\theta}) - \Phi^s)\|_2^2 \quad \text{subject to} \quad \|\boldsymbol{\kappa}\|_1 \leq q \quad (6.3)$$

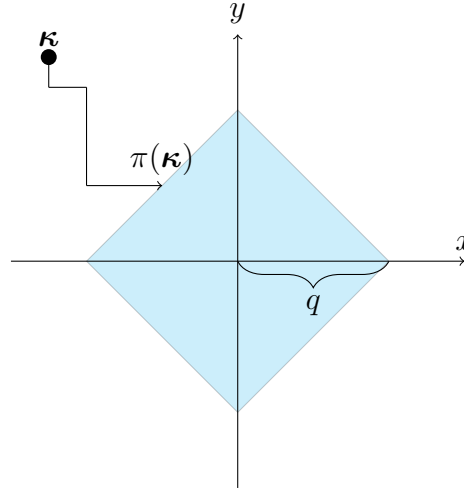


Figure 6.3: *Projection, $\pi(\kappa)$ of the weight vector κ to the ℓ_1 norm ball to induce sparseness. This results in selecting the optimal collection of basis functions representing the shape.*

The \mathbf{W} matrix reflects the structure of the noise corrupting the data and q represents the radius of the ℓ_1 norm ball. This constraint ensures sparsity of the solution, which is dependent on the choice of q . The minimization of the cost function is achieved by a projected Levenberg-Marquardt algorithm, where the minimization of (6.3) is accomplished using a variant of the approach in [66].

As before we employ the Levenberg-Marquardt algorithm, the calculation of the Jacobian matrix \mathbf{J} is required which is computed from the derivative of ϵ with respect to each element in the parameter vector $\boldsymbol{\theta}$, as is shown in (5.19). When estimating the parametric vector, we employ a cyclic coordinate decent strategy which is equivalent to estimating the shape only at even iterations and the concentration values at odd iterations.

To sparsify the κ_i values we want to ensure that the lowest number of basis functions is being added to the recovery of the unknown shape. This is done by enforcing the ℓ_1 -norm constraint by projecting the guess of the weights at each iteration, $\boldsymbol{\kappa}^{n+1}$, to the ℓ_1 -norm ball. This is done through Euclidean projection which is formally defined by

$$\pi(\boldsymbol{\kappa}) = \arg \min_{\mathbf{x}: \|\mathbf{x}\|_1 \leq q} \|\mathbf{x} - \boldsymbol{\kappa}\|_2^2. \quad (6.4)$$

This is represented visually in Fig. 6.3. We solve (6.4) by casting the projection as a root finding problem as described in [74]. This is achieved by introducing a Lagrangian variable ξ for the constraint $\|\mathbf{x}\|_1 \leq q$ so that the Lagrangian of (6.4) can be expressed as

$$L(\mathbf{x}, \xi) = \frac{1}{2} \|\mathbf{x} - \boldsymbol{\kappa}\|^2 + \xi(\|\mathbf{x}\|_1 - q). \quad (6.5)$$

If the \mathbf{x}^* is the primal optimal point, and ξ^* the dual optimal point, they should satisfy $\|\mathbf{x}^*\|_1 \leq q$ and $\xi^* \geq 0$. Liu et al. [74] showed that the \mathbf{x}^* can be computed if ξ^* is defined as known. So \mathbf{x}^* is the optimal solution to the problem defined as

$$\mathbf{x}^* = \underset{\mathbf{x}}{\operatorname{argmin}} L(\mathbf{x}, \xi^*) \quad (6.6)$$

which has a unique solution since $L(.,.)$ is strictly convex in the first argument. By decoupling the variables in (6.6) we have

$$x_i^* = \underset{x_i}{\operatorname{argmin}} = \frac{1}{2}(x_i - \kappa_i)^2 + \xi^*(|x_i| - q) \quad (6.7)$$

where x_i and κ_i are the i^{th} elements of \mathbf{x} and $\boldsymbol{\kappa}$, respectively. This equation can be expressed as

$$x_i^* = \text{sgn}(\kappa_i) \max(|\kappa_i| - \xi^*, 0) \quad (6.8)$$

where $\text{sgn}(\cdot)$ is the signum function. Through this methodology, the problem in (6.4) can be solved by first solving for the dual optimal point ξ^* , which is then used to obtain \mathbf{x}^* using (6.8). This turns the Euclidean projection into a root finding problem using auxiliary function which can be computed through a bisection algorithm which is computationally efficient. We direct the reader to [74] for further details on this approach.

Our approach uses a large dictionary ($L = 220$) to ensure that many different shapes can be recovered. These functions are on a 11 by 5 grid over the imaging domain where at each point there are 4 CRBFs at different dilations and rotations, ensuring different angles can be recovered at each point.

To test the approach we consider simulated data for three different cases. Case I only contains a small elliptical shaped perturbation, which is expected to only need very few basis functions to recover, resulting in a very sparse $\boldsymbol{\kappa}$ vector. For Case II and III, we consider the perturbation in the shape of two ellipses overlapping and a collection of blob like structures, respectively. For these two cases the $\boldsymbol{\kappa}$ vector is expected to stay sparse, although the larger areas with more complicated structures will recover the inclusion of more basis functions. In all cases we consider a realistic optical perturbation, using the same concentration values for HbO_2 and

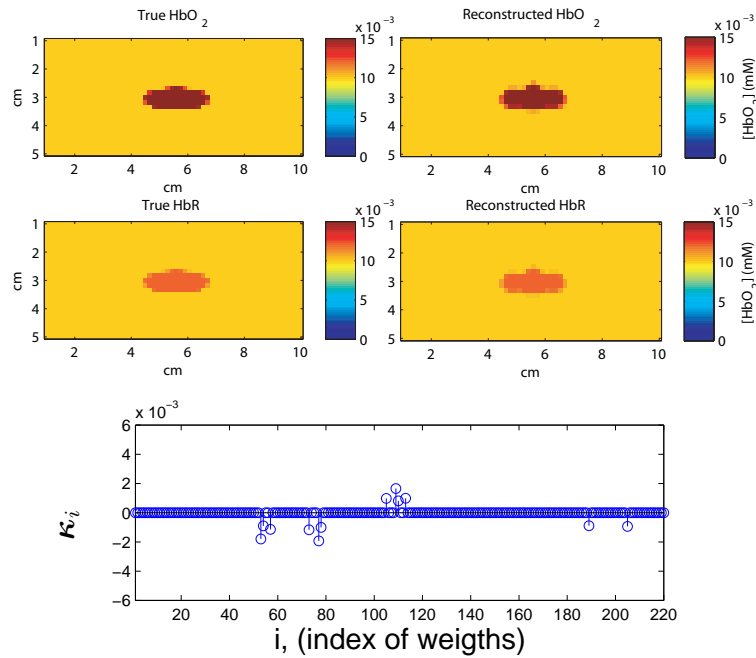


Figure 6.4: *Reconstructions for Case I of low complexity. Top row shows HbO_2 , middle is HbR and bottom row displays weights used in the reconstruction. Signal to noise ratio is set to 50 dB.*

HbR as in Chapter 5. Simulated data is generated with 40 source-detector pairs for 100 wavelengths. The source-detector pairs are aligned along the x -axis with 5 cm separation. As before, we verify our shape recovery by calculate the Dice coefficient for the estimated characteristic functions.

6.3 Results and Discussion

Figures 6.4-6.6 show reconstruction results for Case I, II and III, respectively. As discussed in Section 6.2 all reconstruction use the same dictionary matrix of 220 basis

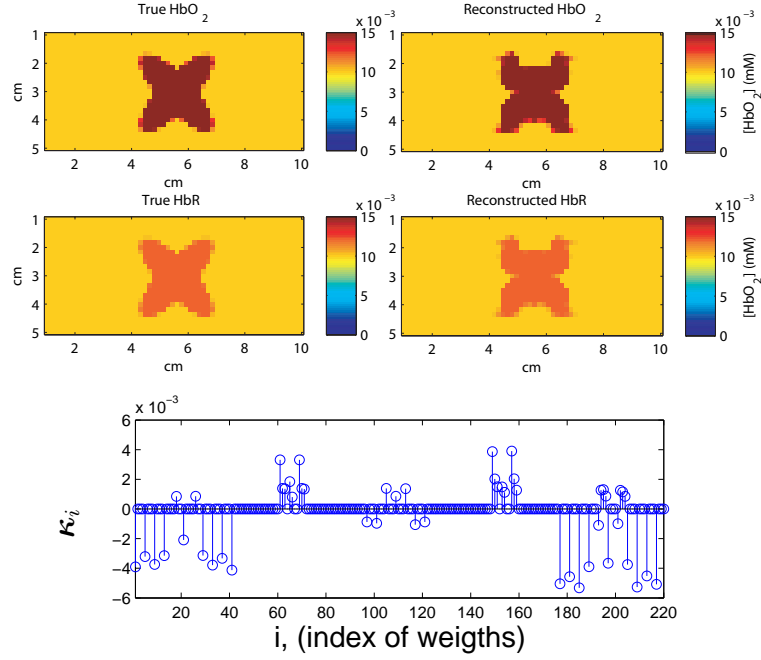


Figure 6.5: *Reconstructions for Case II of medium complexity. Top row shows HbO_2 , middle is HbR and bottom row displays weights used in the reconstruction. Signal to noise ratio is set to 50 dB.*

functions. It is clear that implementing the sparsity constraint ensures that method uses few functions to represent the shape. It is notable for the more complicated shapes that cover a larger area, the weight vector remains sparse, utilizing less than a third of all the CRBFs in the dictionary. As is expected in simulations the concentration values of both HbO_2 and HbR are recovered close to the ground truth values. The Dice coefficient varies from $D(S, G) = 0.86$ for Case III, $D(S, G) = 0.90$ for Case II and $D(S, G) = 0.95$ for Case I. For the reconstruction results shown here, q was chosen by visual inspection and verified by error metrics.

Although these preliminary results are encouraging, the redundant dictionary

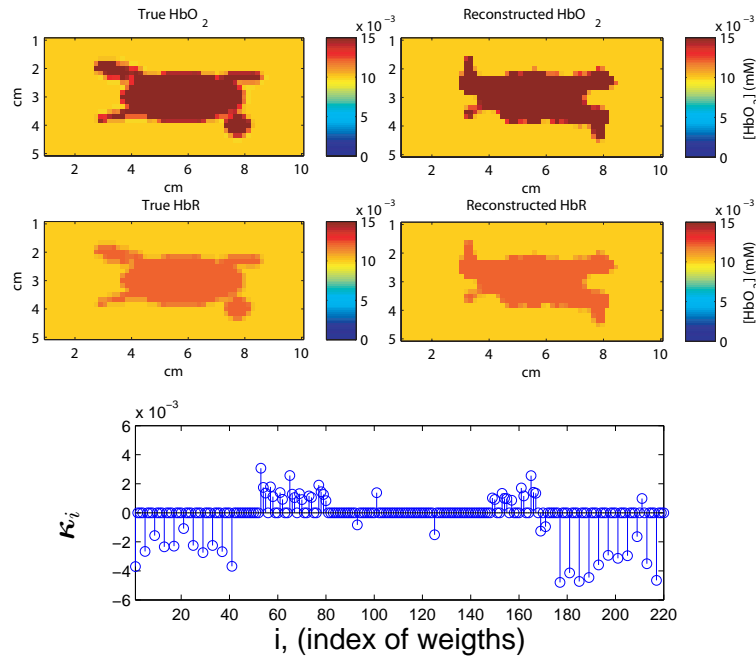


Figure 6.6: *Reconstructions for Case III of high complexity. Top row shows HbO_2 , middle is HbR and bottom row displays weights used in the reconstruction. Signal to noise ratio is set to 50 dB.*

method still has noticeable drawbacks. Considering a basis set \mathcal{P} as it is applied here, it does not show promise for a large improvement over a regular fixed grid. Due to the low spatial resolution of DOT the discrimination between the different basis functions at each grid point, becomes a challenging problem involving selecting the optimal radius of the ℓ_1 norm ball. Examining the properties of the modality and elements of \mathcal{P} we observe the the DOT modality is best suitable for recovering “blob” like structures, as well it is well established that reconstructed images are generally more diffuse along the axis of source detector separation, considered as the z axis here. This reduces the impact of this method, where the limitation of diffusion negates the

approach. Additionally as is noted in the results discussion in Chapter 5, the location of the fixed points becomes an issue, where structures off center relative to the grid points are reconstructed with less accuracy. With this in mind and considering the two main limitations, the limited data encountered in the DOT case and low spatial resolution, we consider a move to a more adaptable and elegant method where the need of a redundant dictionary is less, by incorporating movable basis functions which are entirely made of uniform CSRBFs. This is discussed in detail in Chapter 7.

Although we do not extend the dictionary approach further, it is encouraging to consider this approach for the PaLS method for applications that deal with well-posed problems.

Chapter 7

Parametric estimation of 3D tubular structures using primitives

Expanding on the methods developed in Chapters 5 and 6, we aim to recover the depth, volume and absorption values of fully 3D structures using “coupled” 2D reconstructions within the PaLS framework. As discussed in Chapter 6 the adaptability of the basis functions is imperative, so in this chapter we consider the case of movable basis functions, as was detailed in Chapter 5, and shown in 5.1(c). Additionally, all results discussed here consider bounded (at least partially bounded) domains, a more realistic case than the infinite geometry setup studied in previous chapters.

In this chapter we consider a data limited problem as in Chapter 5 but recover optical absorption images with only single wavelength data. This limits the data further, where we cannot take advantage of multi- or hyperspectral information. This

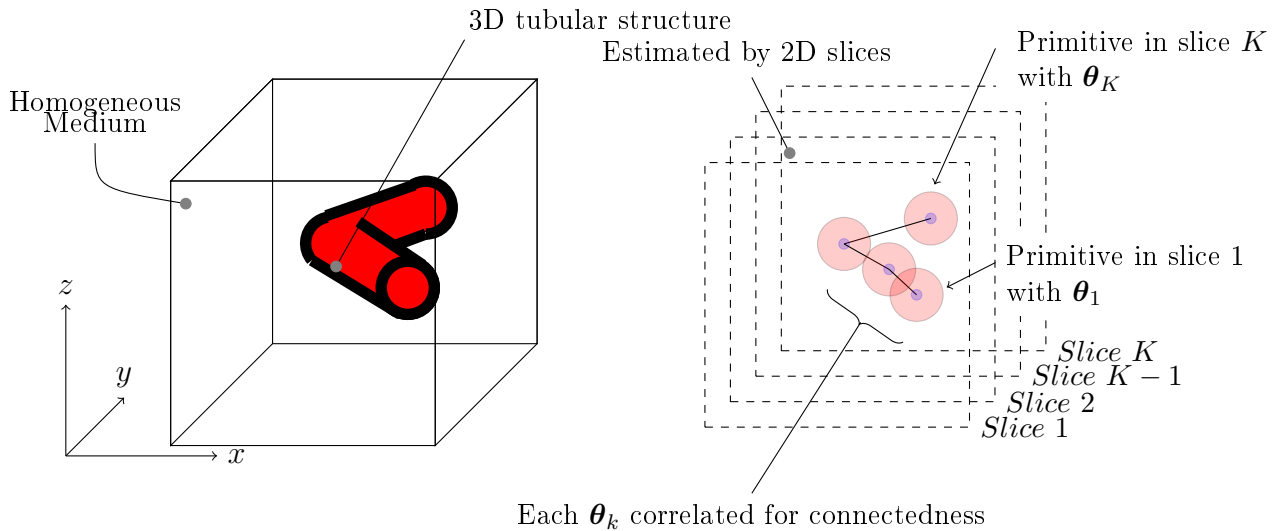


Figure 7.1: *Example of how 2D slices are used to estimate 3D structure with data from measurements collected as in Fig. 4.6. Each 2D primitive is estimated with vector θ_k . Regularization term in the objective function, (7.2), correlates each slice primitive together, to generate a connected structure*

is done for convenience since computing a hyperspectral data set using the finite difference model would be significantly computationally intensive. In spite of these limitations we demonstrate accurate reconstruction of 3D structures by using the PaLS method to reconstruct images for each slice along the y axis in Fig. 4.6. These individual slices are then combined by “stacking” them together in order to estimate the underlying structure along with optical properties, demonstrated in Fig. 7.1. To this end, we setup our model to perform independent 2D image reconstruction from the data collected in each slice, but impose a regularizing term on the low-order parametric vector, to correlate the slices together. This takes advantage of the connected nature of the tubular structures and improves the reconstruction.

7.1 Forward Model for 2D slices

In order to approximate a 3D tubular structure using the model described in Eq. (3.17) we aim to reconstruct slices of a 3D medium and combine them together to estimate the underlying geometry. The physical setup is described in Fig 4.6, where the source and detector are moved in tandem along the x axis, yielding K scans along the y axis. Using our forward model we define $\mathbf{c}_k \in \mathbb{R}^{N_v}$ as the vector of discretized μ_a associated with the k^{th} slice in the rectangular region and Φ_k^s the data collected from the corresponding slice. Using this notation we can write the forward model used for inverse processing for the whole rectangular region in matrix vector notation as

$$\begin{bmatrix} \Phi_1^s \\ \Phi_2^s \\ \vdots \\ \Phi_K^s \end{bmatrix} = \begin{bmatrix} \mathbf{K}_1 & 0 & \dots & 0 \\ 0 & \mathbf{K}_2 & \dots & 0 \\ \vdots & \vdots & \ddots & \vdots \\ 0 & 0 & \dots & \mathbf{K}_K \end{bmatrix} \begin{bmatrix} \mathbf{c}_1 \\ \mathbf{c}_2 \\ \vdots \\ \mathbf{c}_K \end{bmatrix} \Leftrightarrow \Phi^s = \mathbf{K}\mathbf{c} \quad (7.1)$$

where the $(m, j)^{th}$ element of the \mathbf{K}_k represents the m^{th} source-detector pair and j^{th} pixel in the k^{th} slice of the 3D medium. Assuming that for a given experiment N_{sd} source-detector pairs are used for all K slices then if N_p is the number of pixels in each slice the dimensions of the whole matrix \mathbf{K} is $N_{sd}K \times N_pK$.

It should be noted that the block diagonal nature of the model in 7.1 is a reflection of the approximation we are making in which we ignore the effects of “out of plane” physics in each slice of the reconstruction. Our method, detailed in Sections 5.1 and

7.2, of parameterizing the shape and regularization is able to recover accurate 3D structures in spite of this severe physical model mismatch, even with limited data sets. Additionally this approach is easily expandable, by filling in the off-diagonal blocks of \mathbf{K} which will be considered in future developments discussed in Chapter 8.

7.2 Image reconstruction

The image reconstruction method, recovering \mathbf{c} from Φ^s , is formed as an regularized optimization problem of the form

$$\hat{\boldsymbol{\theta}} = \operatorname{argmin} \|\mathbf{W}(\Phi^s - \mathbf{K}\mathbf{c}(\boldsymbol{\theta}))\|_2^2 + \alpha\|\mathbf{L}\boldsymbol{\theta}\|^2 \quad (7.2)$$

where \mathbf{W} represents the structure of the noise corrupting the data. The first term in (7.2) requires that the estimated value of \mathbf{c} is consistent with the observed measurement of Φ^s . The second term of (7.2) is a regularization term that correlates the parameter vector between slices. Considering the prior information of tubular structure anatomy of breast tissues, it encourages correlating reconstructions between slices in the cost functional. Therefore the second term (7.2) ensures that a reconstruction between slices will result in connected structures, which provides better approximation of the structure than a unregularized function. We structure \mathbf{L} to penalize the difference between similar parameters on adjacent primitives. That is to say, we impose a penalty for the difference between centers, \mathbf{r}_i and \mathbf{r}_{i+1} for $i = 1, \dots, N - 1$, the

value of absorption, c_K^a and weight κ_K so that \mathbf{L} is given by.

$$\mathbf{L} = \mathbf{L}_d \otimes \mathbf{I} \quad (7.3)$$

Where \mathbf{I} is a diagonal matrix where number of diagonal elements are the same as number of elements in $\boldsymbol{\theta}_i$, and $\mathbf{A} \otimes \mathbf{B}$ is the Kronecker product [70] of \mathbf{A} and \mathbf{B} and \mathbf{L}_d is written as

$$\mathbf{L}_d = \begin{bmatrix} 1 & -1 & 0 & \dots & 0 & 0 \\ 0 & 1 & -1 & \dots & 0 & 0 \\ \vdots & \ddots & \ddots & \ddots & \ddots & \vdots \\ 0 & \dots & 0 & 1 & -1 & 0 \\ 0 & \dots & 0 & 0 & 1 & -1 \end{bmatrix} \quad (7.4)$$

In order to demonstrate the effectiveness of our regularization method, we evaluate a tomographic reconstruction over a range of values for the regularization parameter α . As α is varied the algorithm trades off the cost associated with the regularization penalty against the cost associated with the data. To select the optimal regularization parameter we employ the commonly used L-curve method, detailed in Section 7.4 [10].

The \mathbf{W} matrix reflects the structure of the noise corrupting the data [48]. We employ a Gaussian noise in which independent, zero mean Gaussian noise is assumed to corrupt each datum where, as in Chapter 5, σ_m^2 and the SNR_m are computed by (5.14) and (5.15), respectively. In experimental data $\sqrt{\Omega(m)}$ is the standard deviation of the Poisson noise distribution.

The minimization of the cost function is then achieved by the Levenberg-Marquardt

algorithm. For that purpose an error vector,

$$\boldsymbol{\epsilon} = [\boldsymbol{\epsilon}_1^T, \boldsymbol{\epsilon}_2^T] \quad (7.5)$$

is introduced where each term relates to the corresponding term in (7.2) given as

$$\boldsymbol{\epsilon}_1 = \mathbf{W}(\mathbf{K}(\boldsymbol{\theta}) - \Phi^s) \quad (7.6)$$

$$\boldsymbol{\epsilon}_2 = \sqrt{\alpha} \mathbf{L} \boldsymbol{\theta}. \quad (7.7)$$

We denote by K the total number of primitives, and the plane in which the i^{th} primitive resides as $y = y_i$, $i = 1, \dots, K$ and the number of basis functions by L in each plane where $l = 1, \dots, L$. For simplicity, we assume that the primitives are equally spaced, though this assumption can be easily relaxed. Thus far, our model only defines the object at K points on the y -axis, as shown in Fig. 7.1, where in essence the primitives may be interpreted as cross section of the overall 3D object. The object description at all other points on the y axis is recovered independently, and then combined to represent the 3D structure.

In order to employ the Levenberg-Marquardt algorithm, the calculation of the Jacobian matrix \mathbf{J} is required, where details are given in Appendix A. The Jacobian contains derivatives of $\boldsymbol{\epsilon}$ with respect to each element in the parameter vector $\boldsymbol{\theta}$

$$\mathbf{J} = \left[\frac{\partial \boldsymbol{\epsilon}(\boldsymbol{\theta})}{\partial \{c_1^a, \dots, c_{N_c}^a, (\boldsymbol{\kappa}_1^T, \dots, \boldsymbol{\kappa}_K^T)^T, (\boldsymbol{\beta}_1^T, \dots, \boldsymbol{\beta}_K^T)^T, (\mathbf{r}_1^T, \dots, \mathbf{r}_K^T)^T\}} \right] \quad (7.8)$$

The solution is then obtained by updating $\boldsymbol{\theta}$ at each iteration as $\boldsymbol{\theta}^{n+1} = \boldsymbol{\theta}^n + \mathbf{h}$ where \mathbf{h} is the solution to a linear system analogous to (5.19).

To summarize, in our method we model the shape structure of the anomaly using a set of 2D shape primitives representing the cross-section of the object in arbitrarily oriented (but parallel) planes. As shown in Fig. 7.1, where the planes are perpendicular to the y -axis, each primitive is itself a 2D shape, specifically a collection of radial basis functions for this chapter, whose structure is defined by its center locations, dilation and weighting factors. In this section we detail the object description when the primitives are stacked along the y -axis. Under our model, the i^{th} primitive is fixed to exist on the plane $y = y_i$. The following parameters are used to represent the primitive.

- A $2 \cdot L \times 1$ vector $\mathbf{r}_i = [\mathbf{x}_{0,i}, \mathbf{z}_{0,i}]^T$, denoting the (x, z) -coordinates of the center location of the basis functions forming the primitive on the plane $y = y_i$
- The dilation factors $\beta_{l,i}$ of the underlying basis functions.
- The weighting factor of $\kappa_{l,i}$ of each basis function. A weighting factor of $\kappa_{l,i} = 0$ deactivates a basis function from the reconstruction.

7.3 Simulation Analysis

Simulations are done to demonstrate the benefit of combining simple 2D reconstructions of more than one slice to approximate 3D structure. In this chapter, simulated data are generated using a standard finite difference forward solution provided by Prof. Misha Kilmer in the Tufts University Math Department. Simulated data are

generated for a rectangular box with dimensions $7 \text{ cm} \times 7 \text{ cm} \times 6.3 \text{ cm}$ discretized into a $71 \times 71 \times 64$ grid, with three cylinders placed close to the center. Boundary conditions on the source and detector planes are Robin type conditions and Dirichlet conditions are applied the sides of the box in the $z - x$ and $z - y$ planes. The true geometry of the phantom is shown in Fig. 7.2. Each cylinder in the medium has $\Delta\mu_a = 0.04 \text{ cm}^{-1}$ where the background has $\mu_a = 0.02 \text{ cm}^{-1}$, giving absorption contrast of 2:1, comparable to what is found in a clinical setting [84]. Diffusion coefficient is assumed to follow Mie Scattering theory and to be uniform throughout the medium and inclusion at $\mu'_s = 10.1 \text{ cm}^{-1}$ at 690 nm [68].

The alignment of sources and detectors is the same as for the experimental setup is shown in Fig. 4.6. Two different cases are considered, to demonstrate the effect of limited data for our method. In Case 1 we use two detectors per source position and 26 source locations along each slice for a total of only 52 measurements per slice. In Case 2 we implement ten detectors for each source position, giving 260 source detector pairs for each slice. These two cases demonstrate the effectiveness of our method even when working with severely limited data such as in Case 1.

In order to obtain a quantitative measure of comparison between the actual and estimated shapes and absorption values, we employ the Dice coefficient as in (5.30), MSE given by (5.29) and add the Symmetric difference which is the fraction of entries in the estimated image, S , where the corresponding entries in the ground truth image,

G , are not equal. Mathematically, this is expressed as

$$d_{sd}(S, G) = \frac{1}{N_v} \sum_i 1_{\{G_i \neq S_i\}} \quad (7.9)$$

where $1_{\{\cdot\}}$ is the indicator function and S is the 0 – 1 characteristic matrix corresponding to the estimated shape, and G the 0 – 1 characteristic matrix corresponding to the actual object.

The symmetric distance is an important measure of the quality of reconstruction because it measures the overall quality of shape reconstruction, by penalizing errors in detecting object voxels as background and similarly background voxels as object voxels. Symmetric difference assigns an equal penalty to an erroneous voxel, irrespective of whether it is detected as background or object. An important limitation of the symmetric difference measure is that it does not reflect well on how close the estimated absorption concentration value in the reconstructed image is to the true value. The mean square error fills this gap by providing a measure on the quantitative accuracy for each slices that measures both how well the shape and value of the $\Delta\mu_a$ is recovered.

As discussed in Section 6.1 our method constrains the image formation problem and reduces the number of unknowns when compared to a traditional pixel-based approach. To demonstrate the effectiveness of our approach we perform pixel-based reconstructions for the simulation cases presented in Section 7.4. We employ a pixel-based optimization method using Levenberg-Marquardt algorithm where we modify

(7.2) so that the regularization term takes the form of traditional Tikhonov regularization, where $\mathbf{L} = \mathbf{I}$. Tikhonov regularization is widely used for image reconstruction for multiple imaging modalities and provides a suitable comparison for our method [85, 110, 56].

7.4 Results

7.4.1 Simulations

Reconstruction results from simulated data are presented in Figs. 7.5 and 7.6 using 2 detectors and 10 detectors for each source location, respectively. Examining the reconstructions visually and with the error metrics presented in Table 7.1 it is evident that the impact of correlation regularization is very important. Especially notable is where unregularized reconstruction, shown in Figs. 7.5(a) and 7.6(a) recovers a structure with gaps, due to the fact that the connected nature of the tubular structure is not being emphasized. Additionally, evident by the shape metrics $D(S, G)$ and d_{sd} the middle rod is recovered as a separate structure when the regularization is present.

The pixel-based reconstruction using traditional Tikhonov regularization is shown in Fig. 7.4 for both the 2 detector and 10 detector setup. It is evident both by visual inspection and error metrics shown in Table 7.1 that the constrained model in PaLS and regularizing between slices results in a far more accurate estimation of the structure. It should be noted that pixel based reconstructions for DOT can be

very accurate, however as mentioned above the work in this chapter presents results using a severely limited dataset. Pixel-based methods traditionally require significant number of data points, resulting in the errors in the reconstruction shown here.

As mentioned in Section 7.2, to optimally select the regularization parameter α we implement the L-curve method. In this method, we generate a plot of $\log(\|\mathbf{L}\boldsymbol{\theta}\|^2)$ against $\log(\|\mathbf{W}(\mathbf{K}(\boldsymbol{\theta}) - \boldsymbol{\Phi}^s)\|^2)$ as α is varied. Figure 7.5(a) depicts the reconstructed object when $\alpha = 0$, where no regularization is being applied. From visual observation as well as examining error metrics defined in Section 7.3, it is clear that some degree of regularization is beneficial. The L-curve plot for the reconstruction of the simulated phantom is shown in Figs. 7.3(a) and 7.3(b) for the 2 detector and 10 detector setups, respectively. Note the encircled point on the curve denotes the “best” reconstruction given the data. The parameter α was obtained in a similar fashion in all our experiments. However, here in order to save space, we have only demonstrated our results for a single case.

Representative slice image from the 10 detector reconstruction is shown in Fig. 7.7. Along with the MSE it allows for visually judging the methods ability to recover the values of $\Delta\mu_a$. As expected using the Born Approximation, the absorption values are underestimated, but these results are encouraging, considering the limited data sets being employed, and how each slice reconstruction is not modeled to incorporate effects from the total 3D structure.

These results are especially encouraging considering the method is able to estimate

the structure even with a severely limited data set, shown in Fig. 7.5, where only 2 detectors are used for each 26 source locations, and only a single wavelength is used. This demonstrates the ability of the slice based PaLS method to accurately recover 3D tubular structures even with linear approximations and limited data sets.

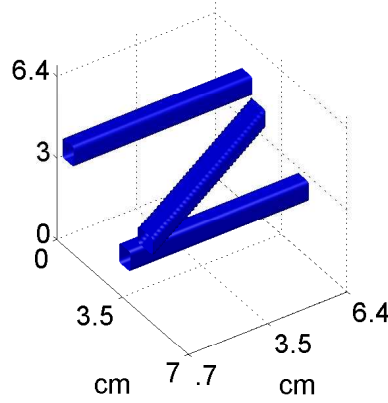


Figure 7.2: *Ground truth image used to generate simulated data.*

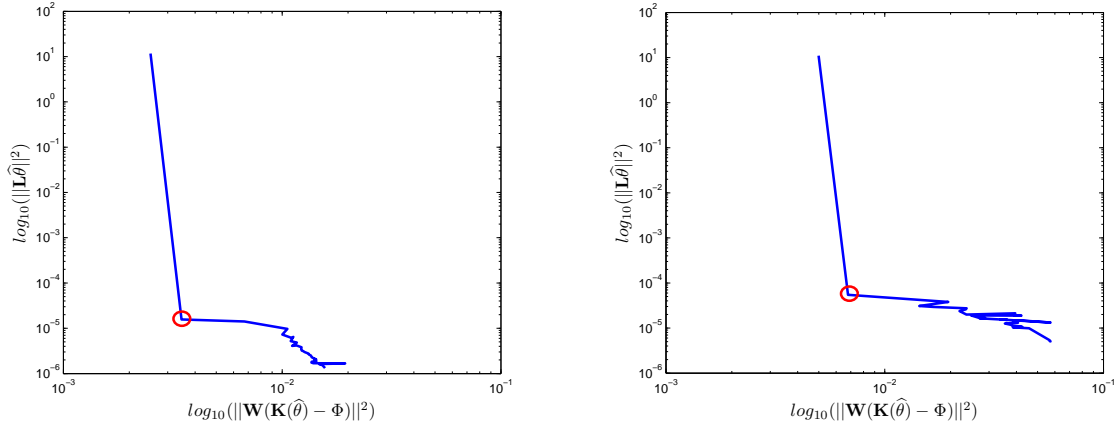
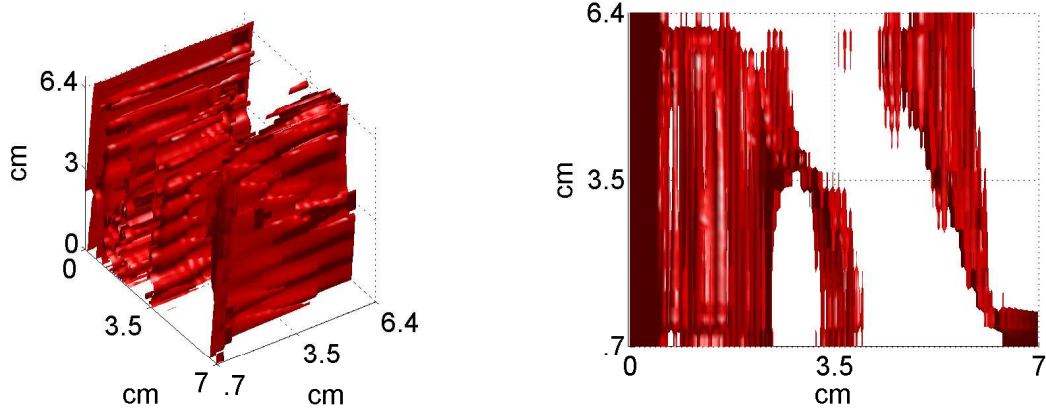
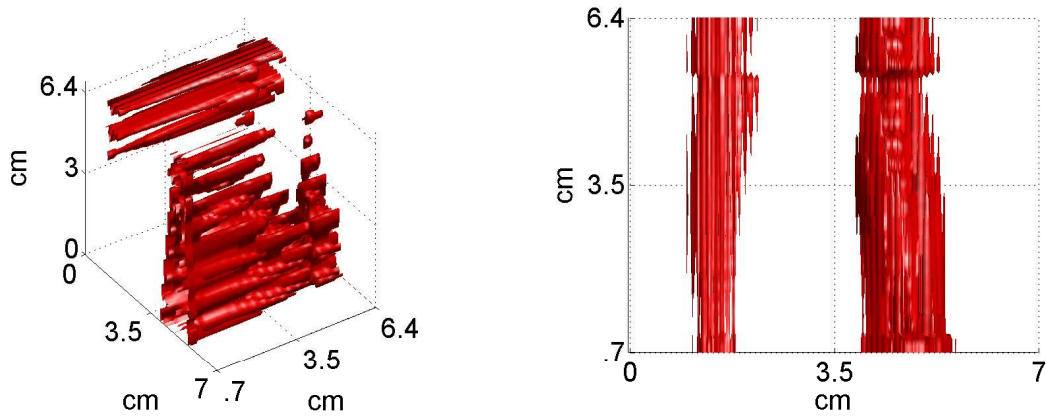


Figure 7.3: (a) *Example L-curve used to select optimal α for the reconstruction using 2 detectors at 30 dB SNR for simulated data.* (b) *Example L-curve used to select optimal α for the reconstruction using 10 detectors at 30 dB SNR for simulated data.*



(a) Pixel-based reconstruction using 2 detectors, $\alpha = 820$

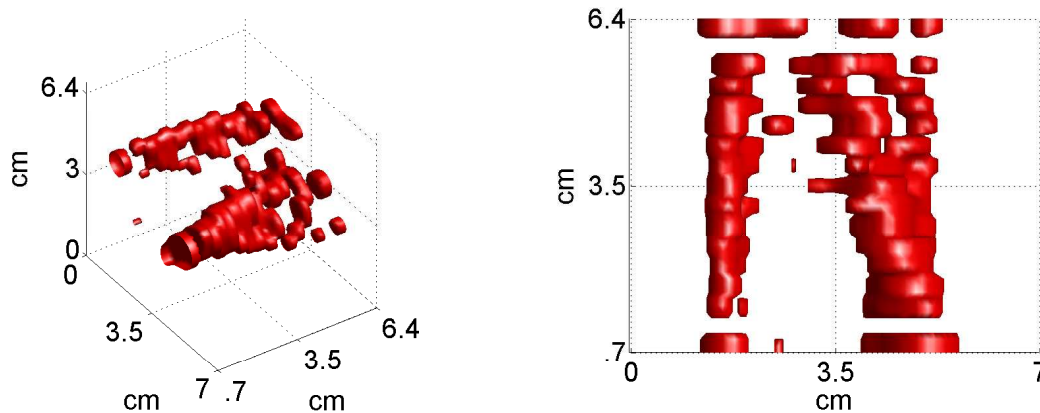


(b) Pixel-based reconstruction using 10 detectors, $\alpha = 300$

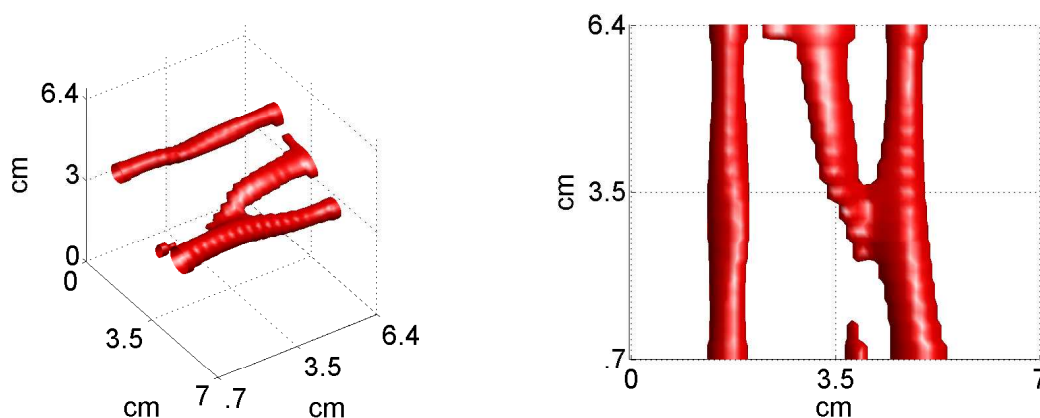
Figure 7.4: *Reconstruction results for a simulated geometry structure with realistic optical contrast.*

7.4.2 Experimental Validation

Reconstruction results for relative absorption reconstructions are shown in Figs. 7.8 and 7.9 for inclusions angled at 90° and 30° , respectively. As demonstrated in simulations, including correlation between adjacent slices greatly improves accuracy and allows for recovery of the underlying structure. Examining the images along with the error metrics, $D(S, G)$, d_{sd} and MSE shown in Table 7.2 it is clear that this method



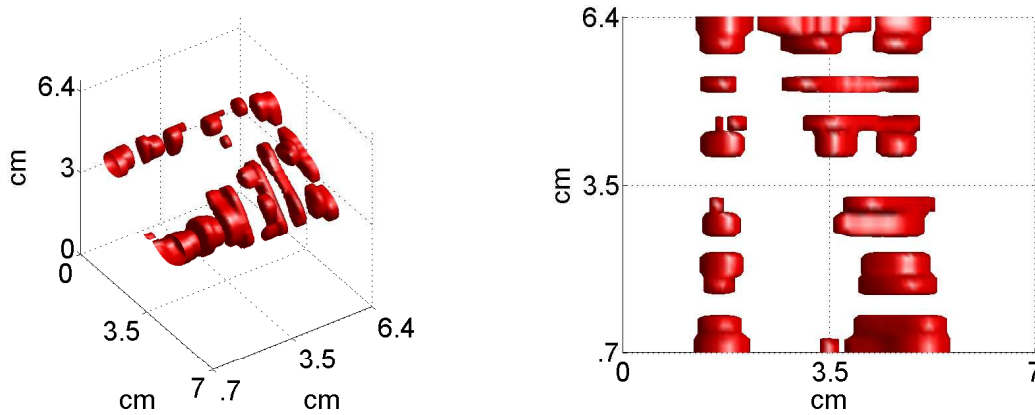
(a) PaLS image reconstruction using 2 detectors, $\alpha = 0$



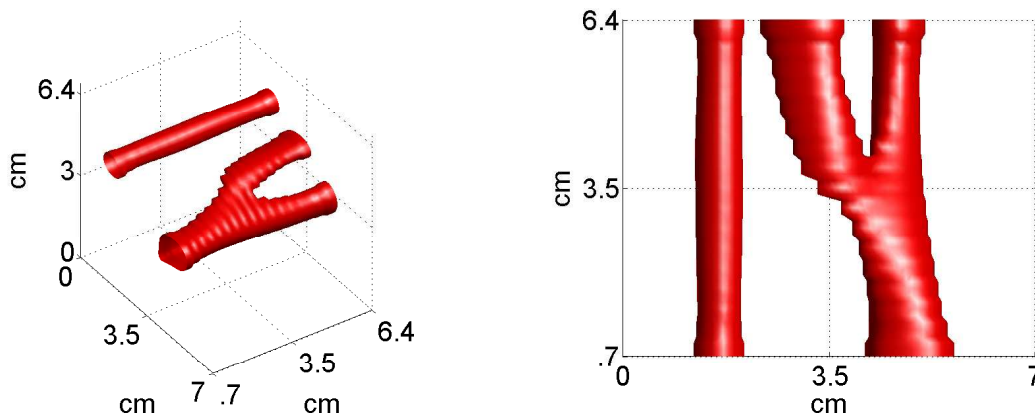
(b) PaLS image reconstruction using 2 detectors, $\alpha = 1.5$

Figure 7.5: *Reconstruction results from simulated data with realistic optical contrast, using 2 detectors for each source location*

allows for recovery of tubular structures in a realistic breast phantom. It is notable that the $10\times$ absorbing inclusion is recovered as a larger structure, whereas the $3\times$ cuboid is recovered close to its true shape with more accurate absorption value. This is demonstrated in an example slice image for the $\varphi = 90^\circ$ case in Fig. 7.10. This is expected due to the aforementioned limitations of the Born Approximation [11] but it is interesting to see, that the higher absorbing structure does not dominate the



(a) PaLS image reconstruction using 10 detectors, $\alpha = 0$



(b) PaLS image reconstruction using 10 detectors, $\alpha = 0.5$

Figure 7.6: *Reconstruction results from simulated data with realistic optical contrast, using 10 detectors for each source location*

optimization and our method correctly locates and recovers the $3 \times$ cuboid. Although the recovered absorption contrast does not improve greatly for the $\varphi = 30^\circ$ case, the shape is recovered much better when regularization is introduced. For the 30° case improvements in both absorption values and shape are evident and examining Fig. 7.9 shows clearly that we are able to recover structures even though they are angled close to the scanning direction.

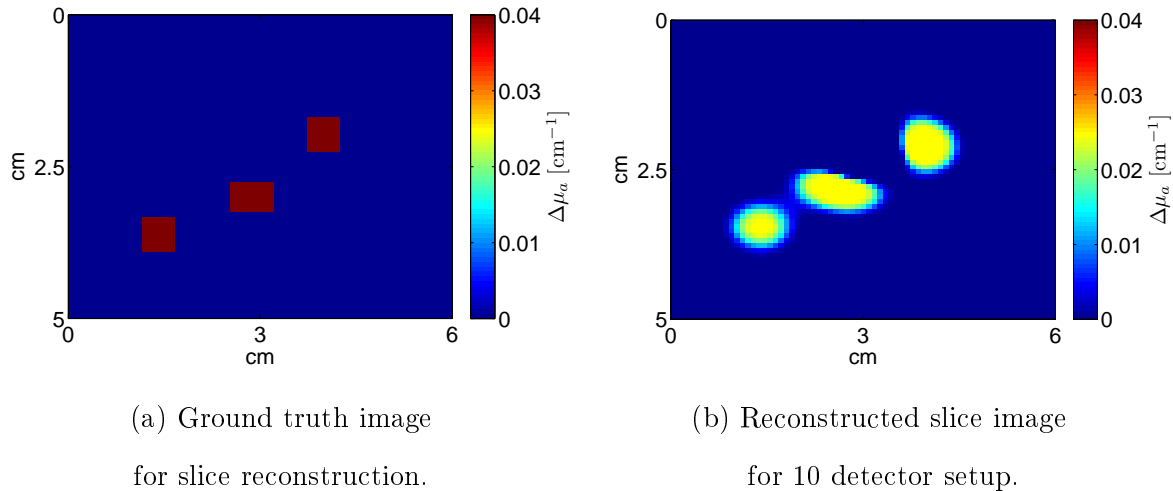


Figure 7.7: *Slice reconstruction from $y = 5$ cm, demonstrating absorption contrast. 3D reconstructed using 10 detectors shown in Fig. 7.6.*

Table 7.1: *Error metrics used to judge image reconstructions for simulated reconstructions.*

Fig.	# detectors	α	$D(S, G)$	d_{sd} [%]	MSE
7.4(a)	2(pixel-based)	820	0.07	76	9.5
7.4(b)	10(pixel-based)	300	0.08	74	8.3
7.5(a)	2	0	0.43	11	1.2
7.5(b)	2	1.5	0.83	10	0.9
7.6(a)	10	0	0.57	12	1.1
7.6(b)	10	19	0.82	9	0.89

The correlation term in (7.2) is shown to be as important for experimental reconstructions as in simulations, both in error metrics in Table 7.2 and visually, in Fig. 7.9(a). For both experimental sets, the primitive 3D PaLS method resolves the location and the shape of the inclusion more accurately, which is verified by all metrics. It should be noted in Table 7.2 that $D(S, G)$ is computed strictly for regions where the inclusions are present. This is due to the Dice coefficient not being a useful metric

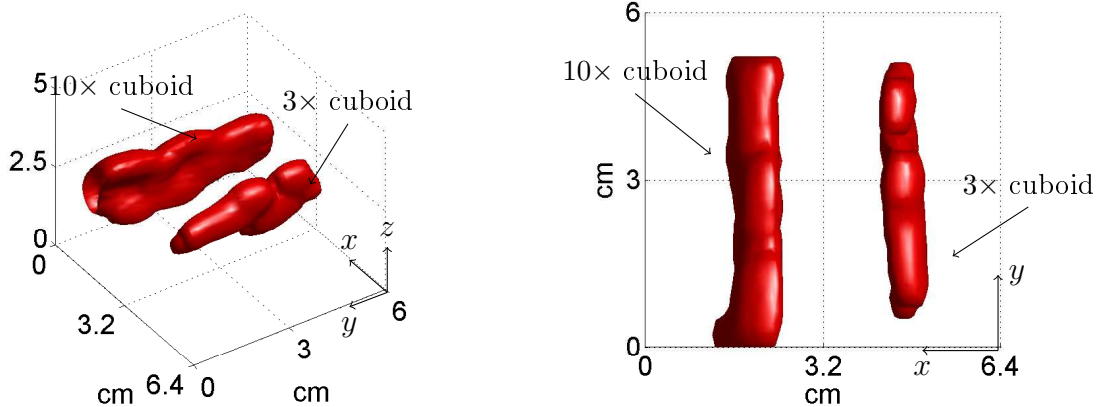


Figure 7.8: *Reconstruction results using experimental data and 3 detectors. Inclusions are angled 90° relative to scanning direction, $\alpha = 12$.*

to judge reconstructions when the ground truth is an empty set image.

Table 7.2: *Error metrics used to judge image reconstructions for experimental reconstructions.*

Fig.	φ	α	$D(S, G)$	d_{sd} [%]	MSE
7.8(a)	90°	0	0.23	8.6	0.99
7.8(b)	90°	0.5	0.55	6	0.97
7.9(a)	30°	0	0.31	13.6	1.10
7.9(b)	30°	0.1	0.65	10	0.98

7.5 Discussion

Using both simulations and experimental measurements we have shown that 3D tubular structures can be recovered by implementing a parametric primitive PaLS method by taking advantage of correlation of adjacent slices. Using an augmented cost function and optimizing regularization results in better performance compared to pixel

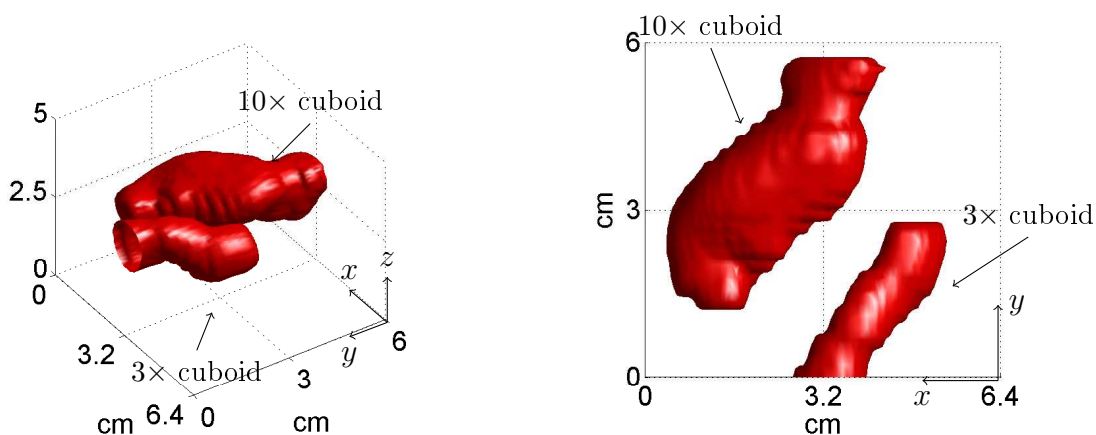
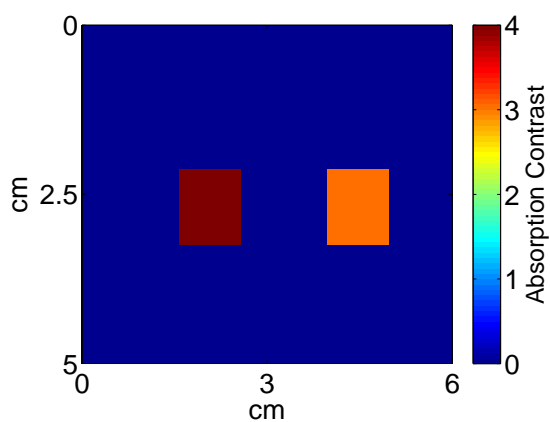


Figure 7.9: *Reconstruction results using experimental data and 3 detectors. Inclusions are angled 30° relative to scanning direction, $\alpha = 80$.*

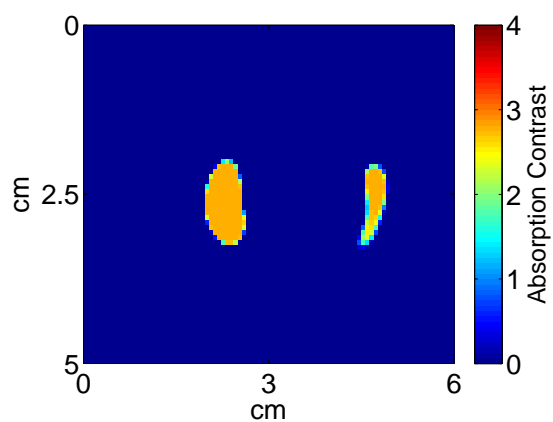
based and unregularized shape based approach measured in terms of MSE and spatial localization as measured using the Dice coefficient and Symmetric difference. This shows that even with implementing linear approximation and using severely limited data sets, the underlying structures can be recovered with accuracy.

These results demonstrated that this approach has significant promise to recover depth and shape estimation along with optical properties in realistic phantoms. With some improvements it would be especially interesting to advance this method by combining it with an optical mammography device, and expanding on the current approach. This consideration is discussed further in Chapter 8



(a) Ground truth image

for $\varphi = 0^\circ$ detector setup.



(b) Reconstructed slice image

for $\varphi = 0^\circ$ detector setup.

Figure 7.10: *Slice reconstruction located at $y = 3$ cm in Fig. 7.8, compared to ground truth demonstrating absorption contrast.*

Chapter 8

Conclusion

In this thesis, we have presented approaches which implement parametric shape-based methods to improve reconstruction algorithms for diffuse optical tomography (DOT). In Chapter 1, we discussed the motivation and basic challenges when working with optical imaging modalities, DOT specifically, for the breast imaging application. Although significant advancements have been made, current research is continuing to improve the quality of the DOT method. Chapter 2 established the basic concepts of the tomography problem and presented an introduction to existing work on solving the inverse problem for optical tomographic techniques.

Chapter 3 detailed how the forward model was constructed for the different geometries considered in this thesis. In Chapter 4 we discussed the physical experiments performed for the purpose of this thesis, which were used for the methods presented in Chapters 5-7, which introduced the parametric level set method, and described

how we apply it to the recovery problem of absorption, scattering and chromophore concentration images for DOT. We presented simulated and physical experiments to demonstrate the advantage of implementing a low-order model over a pixel-based formulation for image reconstruction. The PaLS method not only proved to be more accurate in terms of error metrics, but was demonstrated to be faster, due to the low-order model and the fact that no implicit regularization was required for the image reconstruction.

In Chapter 6 we expanded our method to consider differently shaped basis functions, placed at each grid point, for a fixed based PaLS approach. This was in order to verify that our method could take advantage of a large dictionary matrix without over complicating the estimation by inducing a sparsity constraint on the parametric vector. This method demonstrated some promising qualities for image recovery, but for the case of an ill-posed problem like DOT, optimizing the sparseness of the parametric vector, as well as restricting the movement of the basis functions affects the accuracy of the solution. Estimating the centers of the basis functions and their dilation factors proves to be more adaptable and straightforward rather than using a large dictionary matrix. Because of this we moved to a more adaptable method in Chapter 7.

The 3D estimation using primitives presented in Chapter 7 demonstrated that our method, is able to estimate the shape, depth and optical properties of complicated 3D structures with realistic optical contrast. The recovered structured proved to be

accurate, even when using extremely limited data sets, only 2-3 detectors for each source, and reconstruction performed at a single wavelength. Although absorption values were not recovered exactly at ground truth, this method is adaptable and should be considered for further development.

Based on the results reported on in Chapter 7 we want to improve on this method by testing it with more cases of silicon phantoms, exploring how the effect of low absorption contrasts changes the recovery of structures. Additionally our method is readily expandable to a model where interpolation functions can be applied to the primitives between slices, where n^{th} order hold functions, sinc functions, or spines could be used to interpolate the primitives to represent the 3D structures. These kind of interpolating functions could help recover structures that are recovered with gaps, or other artifacts. Incorporating hyperspectral data to improve recovery of absorption values and allow for direct estimation of chromophore concentrations should also be considered where our approach in Chapter 5 showed significant improvement for the PaLS method. Recovering chromophore information for a vascular structure as is considered in Chapter 5 could be helpful for tumor detection.

As discussed in Section 7.1 our model assumes that for each slice the primitive is invariant along the y -axis. This of course significantly affects the mismatch between the model and the true scenario, but our method demonstrated that correlating the slice images and parameterizing the reconstruction allows for accurate recovery of the vessel like structures. Future efforts will examine the effect of computing the

off diagonal elements of (7.1) where it would be seen how results would change if a certain segment along the y -axis would be modeled in 3D. This would physically represent stacking 3D slices with a certain thickness to recover a larger 3D structure and examining reconstruction accuracy versus computational intensity is a natural progression of our research.

Furthermore the plan is to advance the method to combine with an optical mammography system that obtains depth information of vascular structures. In the end the method presented here, along with optical mammograms, could serve as initial guesses for a full 3D non-linear reconstruction. Providing an accurate initial guess for a non-linear method would not only improve accuracy but significantly speed up computation time commonly found in those types of reconstructions.

In more detail, Prof. Sergio Fantin's group in the Tufts University Biomedical Department, is currently developing and testing an optical mammography device at the Tufts Medical Center. In this system broadband optical mammograms are used for breast tumor detection on the basis of measured oxygen saturation of hemoglobin. The data is collected in a collinear illumination-collection scan of the breast, which is exactly the setup that was considered for the source detector setup in Chapter 7. In addition to measured oxygen saturation, this system allows for depth discrimination in optical mammograms by exploiting directional information of spatial second derivatives. With this in mind, the measurement obtained by the optical mammography device, depth and saturation, could be implemented as an initial guess for our 3D

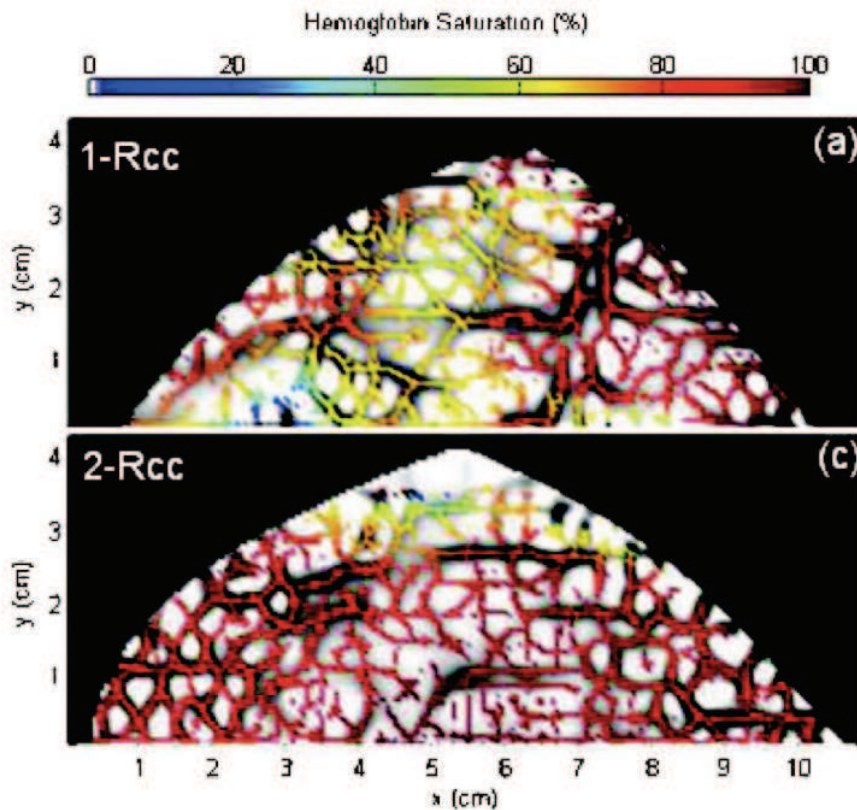


Figure 8.1: *Hemoglobin saturation maps measured, where false-color representation of oxygenation values are superimposed on a gray level image. Image and data was reported in Yu et al. [111].*

primitive reconstruction presented in Chapter 7. This could prove to be extremely useful, where a future clinical system could be considered a stand-alone optical imaging device. Utilizing our method in conjunction with mammograms, the possible workflow for the imaging system could be:

1. Data collection is performed in the clinic, where measurements are collected by scanning sources and detectors in tandem, over the breast. Limited number of detector are placed on- and off-axis, relative to the source.

2. Optical mammogram device measures oxygen saturation, and estimates depth information of detected tissue inhomogeneities. Typical optical mammogram image with measured oxygen saturation is shown in Fig. 8.1.
3. 3D primitive PaLS reconstruction performed using depth and absorption information obtained in Step 2 as initial guess.
4. Full 3D non-linear reconstruction using a finite difference model using structural information from Step 3, saturation and absorption information from Step 2 as a initial guess.

Considering a work-flow like this is encouraging, especially considering the advantage of the PaLS method over pixel-based method presented in Chapter 5 and accuracy in recovering 3D structures in Chapter 7. Steps 2-3 of this flow are methods and algorithms that have already been tested and implemented, where step 3, the 3D primitive method, can be improved by the items discussed earlier in this section. The development of step 4, where implementation of the finite difference model used in Chapter 8 will be developed to take the prior information as an initial guess and render a estimation of the underlying vascular structures and optical properties.

It is also important to integrate the PaLS method with a clinical device such as the optical mammogram, to analyze and provide a rigid framework regarding the basis and stopping criteria for the Levenberg Marquardt algorithm. The rigid framework should take into account how many basis functions are “deactivated” in the estimation, i.e. when the corresponding weight element κ is estimated as zero, the basis function

is considered as deactivated. Running the algorithm repeatedly with analysis could result in an optimal choice of basis functions for each data set. Furthermore, relating to the development of a framework for different basis functions, we will develop the Levenberg Marquardt algorithm to have optimally chosen stopping criteria and step size changes. This should increase robustness of our method and ensure accuracy of estimation for different situations and settings in diffuse optical tomography.

Additionally, incorporating texture functions to estimate variable concentrations and inhomogeneous backgrounds needs to be considered. In that setting, estimating multiple level sets for different geometries could prove useful, especially to estimate different regions of the heterogeneous background such as adipose and fibroglandular tissue. However, a simple approach is to simply multiply the characteristic function χ with a 2D polynomial that results in a recovery varied concentration of chromophores and absorption. This would allow the method to deal with areas that are not strictly piecewise constant.

Appendix A

Jacobian for Levenberg Marquardt optimization

As discussed in Chapters 5 and 7 in order to employ the Levenberg Marquardt algorithm, we need to calculate the Jacobians. The size \mathbf{J} depends on if we are considering a fixed basis grid as in Chapter 5 or movable basis functions as in Chapter 7. As the fixed grid is a simplified version of the movable basis, for this appendix we derive a general case for the error function, ϵ , as it is defined in Chapter 7 as ϵ in Chapter 5 can be considered a simplified case of Chapter 7.

As before we define the cost function in terms of ϵ as

$$M(\boldsymbol{\theta}) = \boldsymbol{\epsilon}^T \boldsymbol{\epsilon} \tag{A.1}$$

where $\boldsymbol{\epsilon}$ is defined as

$$\boldsymbol{\epsilon} = \begin{bmatrix} \boldsymbol{\epsilon}_1 \\ \boldsymbol{\epsilon}_2 \end{bmatrix} = \begin{bmatrix} \mathbf{W}(\mathbf{K}(\boldsymbol{\theta}) - \Phi^s) \\ \sqrt{\alpha}\mathbf{L}\boldsymbol{\theta} \end{bmatrix} \quad (\text{A.2})$$

We begin by considering the derivative term contributed by $\boldsymbol{\epsilon}_2$. Clearly taking the derivative with respect to $\boldsymbol{\theta}$ leaves us with

$$\frac{\delta \boldsymbol{\epsilon}_2(\boldsymbol{\theta})}{\delta \boldsymbol{\theta}} = \sqrt{\alpha}\mathbf{L}. \quad (\text{A.3})$$

This provides the complete characterization of the elements of the Jacobian matrix corresponding to the regularization term. Now considering the derivative term contributed by $\boldsymbol{\epsilon}_1$

$$\begin{aligned} \frac{\delta \boldsymbol{\epsilon}_1}{\delta \boldsymbol{\theta}_k} &= \frac{\delta(\mathbf{W}_k(\mathbf{K}_{k,i}\mathbf{c}_{k,i}(\mathbf{r}) - \Phi_k^s))}{\delta \boldsymbol{\theta}} \\ &= \mathbf{W}_k \mathbf{K}_{k,i} \frac{\delta \mathbf{c}_{k,i}(\mathbf{r})}{\delta \boldsymbol{\theta}} \end{aligned} \quad (\text{A.4})$$

where we generalize for simplicity sake to consider the i^{th} chromophore and the k^{th} slice.

Considering the parameters contained in $\boldsymbol{\theta}$ we start with by computing the derivative with respect to the concentration values of the region of interest and background, $c_{k,i}^a$ and $c_{k,i}^b$, respectively, defined as

$$\begin{aligned} \frac{\delta \boldsymbol{\epsilon}_1}{\delta c_{k,i}^a} &= \mathbf{W}\mathbf{K}\boldsymbol{\chi}_{k,i}(\mathbf{r}) \\ \frac{\delta \boldsymbol{\epsilon}_1}{\delta c_{k,i}^b} &= \mathbf{W}\mathbf{K}(1 - \boldsymbol{\chi}_{k,i}(\mathbf{r})) \end{aligned} \quad (\text{A.5})$$

Now we consider the derivative with regards of the weighting values of each of the CSRBFS, $\boldsymbol{\kappa}$, where for simplification we consider the l^{th} basis function and redefine

the image formulation in (5.2) as

$$\begin{aligned}\mathbf{c}_{k,i}(\mathbf{r}) &= (c_{k,i}^a - c_{k,i}^b)\boldsymbol{\chi}_{k,i}(\mathbf{r}) + c_{k,i}^b \\ &= (c_{k,i}^a - c_{k,i}^b)H(\kappa_{k,l}\boldsymbol{\psi}(\beta_{k,l}\|\mathbf{r} - \mathbf{r}_{k,l}\|)) + c_{k,i}^b\end{aligned}\quad (\text{A.6})$$

To simplify the notation further, we consider the derivatives with respect to the remaining parameters in $\boldsymbol{\theta}$ by writing

$$\begin{aligned}\frac{\delta \epsilon_1}{\delta \{\kappa_{k,l}, \beta_{k,l}, \mathbf{r}_{k,l}\}} &= \frac{\mathbf{W}\mathbf{K}\mathbf{c}(\mathbf{r})}{\delta \{\kappa_{k,l}, \beta_{k,l}, \mathbf{r}_{k,l}\}} \\ &= (c_{k,i}^a - c_{k,i}^b)\mathbf{W}\mathbf{K}\frac{\mathbf{c}_k(\mathbf{r})}{\delta \{\kappa, \beta, \mathbf{r}_{k,l}\}}.\end{aligned}\quad (\text{A.7})$$

Using this we express the derivative with respect to the weighting element $\kappa_{k,l}$ as

$$\frac{\delta \mathbf{c}_k(\mathbf{r})}{\delta \kappa_{k,l}} = \boldsymbol{\psi}(\beta_{k,l}\|\mathbf{r} - \mathbf{r}_{k,l}\|). \quad (\text{A.8})$$

Next we consider the derivative with respect to $\beta_{k,l}$ where we write

$$\begin{aligned}\frac{\delta \mathbf{c}_k(\mathbf{r})}{\delta \beta_{k,l}} &= \frac{\delta H_{2,\epsilon}(\kappa_{k,l}\boldsymbol{\psi}(\beta_{k,l}\|\mathbf{r} - \mathbf{r}_{k,l}\|))}{\delta \beta_{k,l}} \\ &= \kappa_{k,l}\beta_{k,l}\frac{\|\mathbf{r} - \mathbf{r}_{k,l}\|^2}{\|\beta_{k,l}^2(\mathbf{r} - \mathbf{r}_{k,l})\|^\star}\delta_{2,\epsilon}(\kappa_{k,l}\boldsymbol{\psi}(\beta_{k,l}\|\mathbf{r} - \mathbf{r}_{k,l}\|))\boldsymbol{\psi}'(\beta_{k,l}\|\mathbf{r} - \mathbf{r}_{k,l}\|)\end{aligned}\quad (\text{A.9})$$

Now considering derivatives with respect to the center locations of the CSRBFs, $\mathbf{r}_{k,l}$ which we split up into the x and z location by $\mathbf{r}_{k,l} = (X_{k,l}, Z_{k,l})$, and considering their h^{th} component so that $\{x, z\} \in \mathbb{R}^n$ we write

$$\frac{\delta \mathbf{c}_k(\mathbf{r})}{\delta X_{k,l}^{(h)}} = \kappa_{k,l}\beta_{k,l}^2\frac{X_{k,l}^{(h)} - x^{(h)}}{\|\beta_{k,l}(x - X_{k,l})\|^\star}\delta_{2,\epsilon}(\kappa_{k,l}\boldsymbol{\psi}(\beta_{k,l}\|\mathbf{r} - \mathbf{r}_{k,l}\|))\boldsymbol{\psi}'(\beta_{k,l}\|\mathbf{r} - \mathbf{r}_{k,l}\|) \quad (\text{A.10})$$

and

$$\frac{\delta \mathbf{c}_k(\mathbf{r})}{\delta Z_{k,l}^{(h)}} = \kappa_{k,l}\beta_{k,l}^2\frac{Z_{k,l}^{(h)} - z^{(h)}}{\|\beta_{k,l}(z - Z_{k,l})\|^\star}\delta_{2,\epsilon}(\kappa_{k,l}\boldsymbol{\psi}(\beta_{k,l}\|\mathbf{r} - \mathbf{r}_{k,l}\|))\boldsymbol{\psi}'(\beta_{k,l}\|\mathbf{r} - \mathbf{r}_{k,l}\|) \quad (\text{A.11})$$

In (A.9)-(A.11) the term $\psi'(\cdot)$ represents the derivative of the CSRBF.

For the simple case of the fixed grid, the Jacobian matrix contains simply the terms relating to (A.5) and (A.8), as noted in (5.18), where the more complicated situation with movable basis the Jacobian contains the terms (A.8)-(A.11) along with (A.3) for the regularization term, as shown in (7.7) and (7.8).

Bibliography

- [1] Alireza Aghasi, Misha Kilmer, and Eric L. Miller. Parametric level set methods for inveres problems. *SIAM J. Imaging Sci.*, 4:618–650, 2011.
- [2] B.O. Anderson, C.H. Yip, R.A. Smith, R. Shyyan, S.F. Sener, A. Eniu, R.W. Carlson, E. Azavedo, and J. Harford. Guideline implementation for breast healthcare in low-income and middle-income countries: overview of the breast health global initiative global summit 2007. *Cancer*, 15:2221–2243, 2008.
- [3] S. R. Arridge. Optical tomography in medical imaging. *Inverse Probl.*, 15(2):R41–R93, 1999.
- [4] S. R. Arridge and J. C. Hebden. Optical imaging in medicine: Ii. modelling and reconstruction. *Phys. Med. Biol.*, 42(5):841–853, 1997.
- [5] S. R. Arridge and W. R. B. Lionheart. Nonuniqueness in diffusion-based optical tomography. *Opt. Lett.*, 23(11):882–884, 1998.
- [6] S. R. Arridge and M. Schweiger. A gradient-based optimisation scheme for optical tomography. *Optics express*, 2(6):213–226, 1998.

- [7] Simon R. Arridge, Oliver Dorn, Ville Kolehmainen, Martin Schweiger, and Athanasios D. Zacharaopoulos. Parameter and structure reconstruction in optical tomography. *J. Phys.: Conf. Ser.*, 135:012001, 2008.
- [8] S.R. Arridge. The forward and inverse problems in time-resolved infrared imaging. *SPIE Proc., Medical Optical Tomograph: Functional Imaging and Monitoring*, IS11:35–64, 1993.
- [9] R.L. Barbour, H.L. Graber, Y. Wang, J. Chang, and R. Aronson. Perturbation approach for optical diffusion tomography using continuous-wave and time-resolved data. *Med. Opt. Tomography: Functional Imaging and Monitoring*, IS11:87–120, 1993.
- [10] M. Belge, M. E. Kilmer, and E. L. Miller. Efficient determination of multiple regularization parameters in a generalized l-curve framework. *Inverse Probl.*, 18(4):1161–1183, 2002.
- [11] D. A. Boas. A fundamental limitation of linearized algorithms for diffuse optical tomography. *Opt. Express*, 1(13):404–413, 1997.
- [12] D. A. Boas, A. M. Dale, and M. A. Franceschini. A bayesian approach to reconstruction from incomplete projections of a multiple object 3d domain. *Neuroimage*, 23:275–288, 2004.

- [13] D.A. Boas, D.H. Brooks, E.L. Miller, C.A. DiMarzio, M. Kilmer, R.J. Gaudette, and Quan Zhang. Imaging the body with diffuse optical tomography. *IEEE Sig. Process.*, 18(6):57–75, nov. 2001.
- [14] D.A. Boas, M. A. O’Leary, B. Chance, and A.G. Yodh. Scattering of diffuse photon density waves by spherical inhomogeneities within turbid media: analytic solution and applications. *Proc. Natl. Acad. Sci.*, 91(11):4887–4891, 1994.
- [15] G. Boverman, Q. Fang, S. A. Carp, E. L. Miller, D. H. Brooks, J. Selb, R. H. Moore, D. B. Kopans, and D. A. Boas. Spatio-temporal imaging of the hemoglobin in the compressed breast with diffuse optical tomography. *Phys. Med. Biol.*, 52(12):3619–3641, 2007.
- [16] Gregory Boverman and Eric L. Miller. Estimation-theoretic algorithms and bounds for three-dimensional polar shape-based imaging in diffuse optical tomography. *Inverse Problem*, pages 1132–1135, 2006.
- [17] B. Brendel and T. Nielsen. Selection of optimal wavelengths for spectral reconstruction in diffuse optical tomography. *Journal of Biomedical Optics*, 14(3):1–10, 2009.
- [18] Yoram Bresler, Jeffrey A. Fessler, and Albert Macovski. A bayesian approach to reconstruction from incomplete projections of a multiple object 3d domain. *IEEE Transactions on Pattern Analysis and Machine Intelligence*, 11:840–858, 1989.

- [19] S. A. Carp, T. Kauffman, Q. Fang, E. Rafferty, R. Moore, D. Kopans, and D. Boas. Compression-induced changes in the physiological state of the breast as observed through frequency domain photon migration measurements. *J. Biomed Opt.*, 11:064016, 2006.
- [20] A. Cerussi, D. Hsiang, N. Shah, R. Mehta, A. Durkin, J. Butler, and B. J. Tromberg. Predicting response to breast cancer neoadjuvant chemotherapy using diffuse optical spectroscopy. *Proc. Nat. Acad. Sci.*, 104:4014–4019, 2007.
- [21] T. Chan and L. Vese. Active contours without edges. *IEEE Transactions on image processing*, 10:266–277, 2001.
- [22] Abhijit J Chaudhari, Felix Darvas, James R Bading, Rex A Moats, Peter S Conti, Desmond J Smith, Simon R Cherry, and Richard M Leahy. Hyperspectral and multispectral bioluminescence optical tomography for small animal imaging. *Phys. Med. Biol.*, 50(23):5421–5441, 2005.
- [23] R. Choe, A. Corlu, T. Durduran, S.D. Konecky, M. Grosicka-Koptyra, S.R. Arridge, B.J. Czerniecki, D.L. Fraker, A. DeMichele, B. Chance, M.A. Rosen, and A.G. Yodh. Diffuse optical tomography of breast cancer during neoadjuvant chemotherapy: a case study with comparison to mri. *Medical Physics*, 32:1128–1139, 2005.
- [24] S. B. Colak, M. B. van der Mark, G. W. Hooft, J. H. Hoogenraad, E. S. van der Linden, and F. A. Kuijpers. Clinical optical tomography and nir spectroscopy

- for breast cancer detection. *IEEE J. Quantum Electron.*, 5(4):1143–1158, 1999.
- [25] M. P. Coleman, M. Quaresma, F. Berrino, J. M. Lutz and R. De Angelis, R. Capocaccia, P. Baili, B. Rachet and G. Gatta, T. Hakulinen, A. Micheli, M. Sant, H. K. Weir, J. M. Elwood, H. Tsukuma, S. Koifman, G. A. e Silva, S. Francisci, M. Santaquilani, A. Verdecchia, H. H. Storm, and John. L. Young. Cancer survival in Pve continents: a worldwide population-based study (concord). *The Lancet Oncology*, 9:730–756, 2008.
- [26] T.F. Coleman and Y. Li. On the convergence of reflective newton methods for large-scale nonlinear minimization subject to bounds. *Math. Prog.*, 61:189–224, 1994.
- [27] M. Cope. *The development of a near-infrared spectroscopy system and its application for noninvasive monitoring of cerebral blood and tissue oxygenation in the newborn infant*. PhD thesis, Dept. Med. Phys. Biol., University College London, U.K., 1991.
- [28] M. Cope and D.T. Delpy. System for long-term measurements of cerebral blood flow and tissue oxygenation on newborn infants by infra-red. *Med. Biol. Eng. Comput.*, 26(3):289–294, 1988.
- [29] A. Corlu, T. Durduran, R. Choe, M. Schweiger, E. M. C. Hillman, S. R. Arridge, and A. G. Yodh. Uniqueness and wavelength optimization in continuous-wave multispectral diffuse optical tomography. *Opt. Lett.*, 28(23):2339–2341, 2003.

- [30] Alper Corlu, Regine Choe, Turgut Durduran, Kijoon Lee, Martin Schweiger, Simon R. Arridge, Elizabeth M.C. Hillman, and Arjun G. Yodh. Diffuse optical tomography with spectral constraints and wavelength optimization. *Appl. Opt.*, 44(11):2082–2093, 2005.
- [31] J. P. Culver, R. Choe, M. J. Holboke, L. Zubkov, T. Durduran, A. Slemph, and A. G. Yodh. Three-dimensional diffuse optical tomography in the parallel plane transmission geometry: Evaluation of a hybrid frequency domain/continuous wave clinical system for breast imaging. *Med. Phys.*, 30(2):235–247, 2003.
- [32] M. Cutler. Transillumination of breasts. *Surg. Gynecol. Obstet.*, 48:721–727, 1929.
- [33] Hamid Dehghani, Subhadra Srinivasan, Brian W. Pogue, and Adam Gibson. Numerical modelling and image reconstruction in diffuse optical tomography. *Philosophical transactions of the Royal society A*, 367:3073–3093, 2009.
- [34] O. Dorn. A shape reconstruction method for diffuse optical tomography using a transport model and level sets. *Proc IEEE Intl. Symp. Biomedical Imaging*, 135:1015–1018, 2002.
- [35] O. Dorn and D. Lesselier. Level set methods for inverse scattering. *Inverse Problems*, 22:R67–R131, 2006.

- [36] T. Durduran, R. Choe, J. P. culver, L. Zubkov, M. J. Holboke, J. Giammarco, B. Chance, and A. G. Yodh. Bulk optical properties of healthy female breast tissue. *Phys. Med. Biol.*, 47(16):2847–2861, 2004.
- [37] M. E. Eames, B. W. Pogue, and H. Dehghani. Wavelength band optimization in spectral near-infrared optical tomography improves accuracy while reducing data acquisition and computational burden. *J. Biomed. Opt.*, 13(5):1–9, 2008.
- [38] Q. Fang, R. H. Moore, D. B. Kopans, and D. A. Boas. Commpositional-prior-guided image reconstruction algorithm for multi modality imaging. *Biomedical Optics Express*, 1:223–235, 2010.
- [39] S. Fantini, M. A. Franceschini, J. B. Fishkin, B. Barbieri, and E. Gratton. Quantitative detrmination of the absorption spectra of chromophores in strongly scattering media: a light-emitting-diode based technique. *Applied Optics*, 33:5204–5213, 1994.
- [40] S. Fantini, M. A. Franceschini, J. B. Fishkin, and E. Gratton. Absolute measurement of absorption and scattering coefficients spectra of a multiply scattering medium. *Proc. SPIE*, 2131:356–364, 1994.
- [41] S. Fantini, M. A. Franceschini, J. S. Maier, S. A. Walker, B. Barbieri, and E. Gratton. Frequency-domain multichannel optical detector for noninvasive tissue spectroscopy and oximetry. *Opt. Eng.*, 34(1):32–42, 1995.

- [42] S. Fantini, E. L. Heffer, V. E. Pera, A. Sassaroli, and N. Liu. Spatial and spectral information in optical mammography. *Technol. Cancer Res. Treat.*, 4(5):471–482, 2005.
- [43] S. Fantini and A. Sassaroli. Near-infrared optical mammography for breast cancer detection with intrinsic contrast. *Annals of Biomedical Engineering*, 40:398–407, 2011.
- [44] S. Fantini and A. Sassaroli. Near-infrared optical mammography for breast cancer detection with intrinsic contrast. *Annals of Biomedical Engineering*, 40:398–407, 2012.
- [45] M. A. T. Figueiredo, R. D. Nowak, and S. J. Wright. Gradient projection for sparse reconstruction: application to compressed sensing and other inverse problems. *IEEE journal of selected topics in signal processing*, 1:586–597, 2007.
- [46] Harley Flanders. *Differential Forms with Applications to the Physical Sciences*. Dover, New York, 1 edition, 1989.
- [47] M. A. Franceschini, V. Toronov, M. E. Filiaci, E. Gratton, and S. Fantini. On-line optical imaging of the human brain with 160-ms temporal resolution. *Opt. Express*, 6:49–57, 2000.
- [48] Richard J. Gaudette, Dana H. Brooks, Charles A. DiMarzio, Misha E. Kilmer, Eric L. Miller, Thomas Gaudette, and David A. Boas. A comparison study

- of linear reconstruction techniques for diffuse optical tomographic imaging of absorption coefficient. *Phys. Med. Biol.*, 45:1051–1069, 2000.
- [49] A. P. Gibson, J. C. Hebden, and S.R. Arridge. Recent advances in diffuse optical imaging. *Phys. Med. Biol.*, 50:R1–R43, 2004.
- [50] R. C. Gonzalez and R. E. Woods. *Digital Image Processing*. Prentice-Hall, New Jersey, 2 edition, 2002.
- [51] E. Gratton, S. Fantini, M. A. Franceschini, C. Gratton, and M. Fabiani. Measurements of scattering and absorption changes in muscle and brain. *Philos. Trans. R. Soc. Lond. B. Biol. Sci.*, 352:727–735, 1997.
- [52] C. M. Gros, Y. Quenneville, and Y. Hummel. Diaphanologie mammaire. *J. Radiol. Electrol. Med. Nucl.*, 53:297–302, 1972.
- [53] U.S. Cancer Statistics Working Group. United States Cancer Statistics: 1999–2008 Incidence and Mortality Web-based Report. Technical report, Department of Health and Human Services and Center for Disease Control and Prevention and National Cancer Institute, 2012.
- [54] M. Guven. *Identifying and addressing the error sources in diffuse optical tomography*. PhD thesis, Rensselaer Polytechnic Institute, 2007.
- [55] M. Guven, B. Yazici, X. Intes, and B. Chance. Diffuse optical tomography with a priori anatomical information. *Phys. Med. Biol.*, 50(12):2837–2858, 2005.

- [56] P. C. Hansen. *Rank-Deficient and Discrete Ill-Posed Problems: Numerical Aspects of Linear Inversion*. Society for Industrial and Applied Math, 1 edition, 1987.
- [57] P. C. Hansen. *Rank-Deficient and Discrete Ill-Posed Problems*. SIAM, Philadelphia, 1 edition, 1997.
- [58] R. C. Haskell, L. O. Svaasand, T. T. Tsay, T. C. Feng, M. S. McAdams, and B. J. Tromberg. Boundary conditions for the diffusion equation in radiative transfer. *JOSA A*, 11:2727–2741, 1994.
- [59] A. H. Hielscher and S. Bartel. Use of penalty terms in gradient-based iterative reconstruction schemes for optical tomography. *J. Biomed. Opt.*, 6(2):183–192, 2001.
- [60] Andreas H. Hielscher, Alexander D. Klose, and Kenneth M. Hanson. Gradient-based iterative image reconstruction scheme for time-resolved optical tomography. *IEEE Transactions on Medical Imaging*, 18:262–271, 1999.
- [61] D. Hyde. *Improving Forward Matrix Generation and Utilization for Time Domain Diffuse Optical Tomography*. PhD thesis, Worcester Polytechnic Institute, 2002.
- [62] R. A. Jesinger, G. E. Lattin, E. A. Ballard, S. M. Zelasko, and L. M. Glassman. Vascular abnormalities of the breast: Arterial and venous disorders, vascular

- masses, and mimic lesions with radiologic-pathologic correlation. *Radiographics*, 31:E117–E136, 2011.
- [63] H. Jiang, N.V. Iftimia, Y. Xu, J.A. Eggert, L.L. Fajardo, and K.L. Klove. Near-infrared optical imaging of the breast with model-based reconstruction. *Academic Radiology*, 9:186–194, 2002.
- [64] F.F. Jobsis. Noninvasive infrared monitoring of cerebral and myocardial sufficiency and circulatory parameters. *Science*, 198:1264–1267, 1977.
- [65] A. A. Joshi, A. J. Chaudhari, D. W. Shattuck, J. Dutta, R. M. Leahy, and A. W. Toga. Posture matching and elastic registration of a mouse atlas to surface topography range data. *Proc IEEE Intl. Symp. Biomedical Imaging.*, pages 366–369, 2009.
- [66] C. Kanzow, M. Yamashita, and M. Fukushima. Levenberg marquardt methods for constrained nonlinear equations with strong local convergence properties. *J. Comput. Appl. Math.*, 172:375–397, 2004.
- [67] Misha E. Kilmer, Eric L. Miller, Alethea Barbaro, and David Boas. Three-dimensional shape-based imaging of absorption perturbation for diffuse optical tomography. *Applied Optics*, 42:3129–3144, 2003.
- [68] S. D. Konecky, R. Choe, A. Corlu, K. Lee, R. Wiener, S. M. Srinivas, J. R. Saffer, R. Freifelder, J. S. Karp, N. Hajjioui, F. A., and A. G. Yodh. Comparison of

- diffuse optical tomography of human breast with whole-body and breast-only positron emission tomography. *Med. Phys.*, 35(2):446–455, 2008.
- [69] D. Landgrebe. Hyperspectral image data analysis as a high dimensional signal processing problem. *IEEE Sig. Process.*, 19(1):17–28, 2002.
- [70] Alan J. Laub. *Matrix Analysis for Scientists and Engineers*. SIAM: Society for industrial and applied mathematics, New York, 1 edition, 2004.
- [71] A. Li, E. L. Miller, M. E. Kilmer, T. J. Brukilacchio, T. Chaves, J. Stott, Q. Zhang, T. Wu, M. Chorlton, R. H. Moore, D. B. Kopans, , and D. A. Boas. Tomographic optical breast imaging guided by three-dimensional mammography. *Appl. Opt.*, 45(25):5181–5190, 2003.
- [72] Ang Li, Greg Boverman, Yiheng Zhang, Dana Brooks, Eric L. Miller, Misha E. Kilmer, Quan Zhang, Elizabeth M. C. Hillman, and David A. Boas. Optimal linear inverse solution with multiple priors in diffuse optical tomography. *Appl. Opt.*, 44(10):1948–1956, 2005.
- [73] Ang Li, Quang Zhang, Joseph P. Culver, Eric L. Miller, and David A. Boas. Reconstructing chromosphere concentration images directly by continuous diffuse optical tomography. *Opt. Lett.*, 29(3):256–258, 2004.
- [74] J. Liu and J. Ye. Visual efficient euclidean projections in linear time. *Proceedings of the Twenty Sixth International Conference on Machine Learning (ICML)*, 2009.

- [75] N. Liu, A. Sassaroli, and S. Fantini. Paired-wavelength spectral approach to measuring the relative concentrations of two localized chromophores in turbid media: an experimental study. *Journal of Biomedical Optics*, 12:01560, 2007.
- [76] K. Madsen, H. Bruun, and O. Tingleff. *Methods for non-linear least squares problems*. DTT, Copenhagen, 2 edition, 2004.
- [77] F. Martelli, S. Del Bianco, A. Ismaelli, and G. Zaccanti. *Light Propagation Through Biological Tissue and Other Diffusive Media: Theory, Solutions, and Software*. SPIE, Bellingham, 1 edition, 2009.
- [78] M. I. Mischenko. Radiative transfer theory: From maxwell’s equations to practical applications. In B.A. van Tiggelen and S.E. Skipetrov, editors, *Wave scattering in complex media: From theory to Applications*, pages 367–414. Kluwer Academic, 2003.
- [79] Tim Nielsen, Bernhard Brendel, Ronny Ziegler, Michiel van Beek, Falk Uhlemann, Claas Bontus, and Thomas Koehler. Linear image reconstruction for a diffuse optical mammography system in a noncompressed geometry using a scattering fluid. *Applied Optics*, 48:D1–D13, 2010.
- [80] S. Osher and R. Fedkiw. *Level set methods and dynamic implicit surfaces*. Springer, New York, 1 edition, 2002.

- [81] M. A. O'SLeary, D. A. Boas, B. Chance, and A. G. Yodh. Experimental images of heterogeneous turbid media by frequency-domain diffusing-photon tomography. *Opt. Lett.*, 20(5):426–428, 1995.
- [82] C. C. Paige and M. A. Saunders. Lsqr: An algorithm for sparse linear equations and sparse least squares. *ACM Trans. Math. Software*, 8:43–71, 1982.
- [83] K.D. Paulsen, P. M. Meany, and L. Gilman. *Alternative Breast Imaging: for model-based approaches*. Springer, New York, 1 edition, 2004.
- [84] B. W. Pogue, S. Jiang, H. Dehghani, C. Kogel, S. Soho, S. Srinivasan, X. Song, T. D. Tosteson, S. P. Poplack, and K. D. Paulsen. Characterization of hemoglobin, water, and nir scattering in breast tissue: analysis of intersubject variability and menstrual cycles changes. *J. Biomed. Opt.*, 9(3):541–552, 2004.
- [85] B. W. Pogue, T. O. McBride, J. Prewitt, U. L. Osterberg, and K. D. Paulsen. Spatially variant regularization improves diffuse optical tomography. *Appl. Opt.*, 38(13):2950–2961, 1999.
- [86] B. W. Pogue, S. P. Poplack, T. O. McBride, W. A. Wells, K. S. Osterman, U. L. Osterberg, and K. D. Paulsen. Quantitative hemoglobin tomography with diffuse near-infrared spectroscopy pilot results in the breast. *Radiology*, 218:261–266, 2001.

- [87] P. Porter. Westernizing womens risks? breast cancer in lower-income countries. *New England Journal of Medicine*, 358:213–216, 2008.
- [88] S. Prahl. Tabulated molar extinction coefficient for hemoglobin in water. <http://omlc.orgi.edu/spectra/hemoglobin/summary.html>.
- [89] H. Rauhut, K. Schnass, and P. Vandergheynst. Compressed sensing and redundant dictionaries. *IEEE transactions on Information Theory*, 54:2210–2219, 2008.
- [90] J. Ripoll and V. Ntziachristos. Iterative boundary method for diffuse optical tomography. *Journal of the Optical Society of America A*, 20:1103–1110, 2003.
- [91] Angelo Sassaroli, Fabrizio Martelli, and Sergio Fantini. Perturbation theory for the diffusion equation by use of the moments of the generalized temporal point-spread function. iii. frequency-domain and time-domain results. *Journal of the Optical Society of America Part A*, 27:1723–1742, 2010.
- [92] M. Schweiger and S. R. Arridge. Optical tomographic reconstruction in a complex head model using a priori region boundary information. *Phys. Med. Biol.*, 44(11):2703–2721, 1999.
- [93] M. Schweiger, S.R. Arridge, and D.T. Delpy. Application of the finite-element method for the forward and inverse models in optical tomography. *Journal of Math. Imaging vision*, 3:263–283, 1993.

- [94] M. Schweiger, O. Dorn, and S. R. Arridge. 3-d shape and contrast reconstruction in optical tomography with level sets. *J. Phys.: Conf. Ser.*, 135:135:012001, 2008.
- [95] M. Schweiger, A. Gibson, and S. R. Arridge. Computational aspects of diffuse optical tomography. *IEEE Comput. Sci. Eng.*, 5(6):33–41, 2003.
- [96] G. Shaw and D. Manolakis. Signal processing for hyperspectral image exploitation. *IEEE Sig. Process.*, 19(1):12–16, 2002.
- [97] H. Soliman, A. Gunasekara, M. Rycroft, J. Zubovits, R. Dent, J. Spayne, M. J. Yaffe, and G. Czarnota. Functional imaging using diffuse optical spectroscopy of neoadjuvant chemotherapy response in women with locally advanced breast cancer. *Clinical Cancer Research*, 16:2605–2614, 2010.
- [98] L. Spinelli, A. Torricelli, A. Pifferi, P. Taroni, G. Maria Danesini, and R. Cubeddu. Bulk optical properties and tissue components in the female breast from multiwavelength time-resolved mammography. *J. Biomed. Opt.*, 9(6):1137–1142, 2004.
- [99] S Srinivasan, B W Pogue, H Dehghani, S Jian, X Song, and K D Paulsen. Improved quantification of small objects in near-infrared diffuse optical tomography. *Journal of Biomedical Optics*, 9:1161–1171, 2004.
- [100] S. Srinivasan, B. W. Pogue, S. Jiang, H. Dehghani, C. Kogel, S. Soho, J. J. Gibson, T. D. Tosteson, S. P. Poplack, and K. D. Paulsen. Interpreting hemoglobin

- and water concentration, oxygen saturation, and scattering measured in vivo by near-infrared breast tomography. *Proc. Natl. Acad. Sci.*, 100(21):12349–12354, 2003.
- [101] T. Tanaka, C. Riva, and I. Ben-Sira. Blood velocity measurements in human retinal vessels. *Science*, 186:830, 1974.
- [102] P. Taroni, A. Pifferi, A. Torricelli, D. Comelli, and R. Cubeddu. In vivo absorption and scattering spectroscopy of biological tissues. *Photochem. Photobiol. Sci.*, 2(2):124–129, 2003.
- [103] Tanja Tarvainen, Ville Kolehmainen, Jari P. Kaipio, and Simon r. Arridge. Corrections to linear methods for diffuse optical tomography using approximation error modelling. *Biomedical Optics Express*, 1:209–222, 2010.
- [104] S. v. d. Ven, S. Elias, A. Wiethoff, M. v. d. Voort, A. Leproux, T. Nielsen, B. Brendel, L. Bakker, M. v. d. Mark, W. Mali, , and P. Luijten. Diffuse optical tomography of the breast: Initial validation in benign cysts. *Mol. Imaging Biol.*, 11(2):64–70, 2009.
- [105] S. M. W. Y. van de Ven, W. O. Th. M. Mali, S. G. Eli, A. J. Weithoff, M. van der Voort, M. B. van der Mark, and P. Luijten. Optical imaging of the breast: clinical research using an experimental diffuse optical tomography system. *Medicamundi*, 54:69–77, 2010.

- [106] C.R. Vogel. *Computational Methods for Inverse Problems*. Society for Industrial and Applied Math, 1 edition, 2002.
- [107] J. D. Vylder and W. Philips. A computational efficient external energy for active contour segmentation using edge propagation. *Intl. con. on Im. Processing.*, pages 661–664, 2010.
- [108] J. Wang, S. C. Davis, S. Srinivasan, S. Jiang, B. W. Pogue, and K. D. Paulsen. Spectral tomography with diffuse near-infrared light: inclusion of broadband frequency domain spectral data. *J. Biomed. Opt.*, 13(4):1–10, 2008.
- [109] T. T. Wu and K. Lange. Coordinate descent algorithms for lasso penalized regression. *Applied Statistics*, 2:224–244, 2008.
- [110] P. K. Yalavarthy, B. W. Pogue, H. Dehghani, C. M. Carpenter, S. Jiang, and K. D Paulsen. Structural information within regularization matrices improves near infrared diffuse optical tomography. *Opt. Express*, 15(13):8043–8058, 2007.
- [111] Y. Yu, N. Liu, A. Sassaroli, and S. Fantini. Near-infrared spectral imaging of the female breast for quantitative oximetry in opticali mammography. *Applied Optics*, 48:D225–D235, 2009.
- [112] Athanasios D. Zacharaopoulos, Simon R. Arridge, Oliver Dorn, Ville Kolehmainen, and Jan Sikora. Three-dimensional reconstruction of shape and

- piecewise constant region values for optical tomography using spherical harmonic parametrization and a boundary element method. *Inverse Problem*, 22:1509–1532, 2006.
- [113] Q. Zhang and H. Jiang. Three-dimensional diffuse optical tomography of simulated hand joints with a 64x 64 channel photodiodes-based optical system. *J. Opt. A Pure Appl. Opt.*, 7(5):224–231, 2005.
- [114] Hong-Kai Zhao, Stanley Osher, Barry Merriman, and Myungjoo Kang. Implicit and non-parametric shape reconstruction from unorganized data using a variational level set method. *UCLA CAM rep.*, pages 98–7, 1998.
- [115] Q. Zhu, P. U. Hegde, A. Ricci, M. Kane, E. B. Cronin, Y. Ardeshirpour, C. Xu, A. Aguirre, S. H. Kurtzman, P. J. Deckers, and S. H. Tannenbaum. Early-stage invasive breast cancers: potential role of optical tomography with us localization in assisting diagnosis. *Radiology*, 256:367–378, 2010.